Direct observation of ultrafast atomic motion using time-resolved X-ray diffraction

Vom Fachbereich Physik der Universität Duisburg-Essen zur Erlangung des akademischen Grades eines Doktors der Naturwissenschaften genehmigte

Dissertation

von

Uladzimir Shymanovich

aus

Minsk

Referent: Prof. Dr. Dietrich von der Linde

Korreferent: Prof. Dr. Michael Horn-von Hoegen

Tag der mündlichen Prüfung: 13.11.2007

Contents

List of figures

List of tables

1. Introduction

1.1. Introduction and motivation

Studying the structural properties of condensed matter systems started to widely develop after the discovery of X-rays by Röntgen in 1895 [1]. In 1912 Laue discovered X-ray diffraction [2, 3] and in 1913 Bragg demonstrated a possibility to determine the structure of crystals [4]. Since then X-ray structural analysis has been playing an important role not only in physics but also in medicine, chemistry and biology. X-ray structural analysis allows very complicated structures such as biological molecules to be investigated. The reason for this is that the short wavelength of X-rays matches the typical distance between atoms in molecules or solids, which makes it possible to get direct information about the atomic positions in materials.

However, the classical structural analysis provides only static information on atomic structure. A natural wish would be to observe not only a static picture but also to monitor the dynamics of atoms during such fundamental phenomena in nature as phase transitions, chemical reactions and vibrations in molecules or solids which typically take place on a femtosecond (fs) to picosecond (ps) time scale. It took about a century to extend structural analysis to the domain of ultrafast (few ps …fs) science. Until recently, this was not possible because X-ray pulses with a duration significantly less than a hundred picoseconds were not available. A breakthrough was achieved with the development of femtosecond laser technologies [5, 6]. In 1997 Rischel et al. demonstrated the first X-ray diffraction experiment with subpicosecond temporal resolution using a laser-plasma based X-ray source [7]. A laser-plasma based X-ray source can generate X-ray pulses with a duration comparable to that of the driving laser pulse (i. e. approximately 100 fs). A more detailed description of its principle of operation will be given in section 1.3.

Another way to perform time-resolved diffraction experiments is to use X-rays from accelerator–based sources [8-10]. Today, the development of both methods of ultrashort X-ray generation is actively taking place. But it should be noted that the

development of the latter method is carried out on large accelerator facilities (such as the Linac Coherent Light Source “LCLS” at SLAC in Standford, USA and the X-ray Free-Electron Laser “XFEL” at DESY in Hamburg, Germany), whereas the laser-plasma based X-ray source together with a terawatt laser system can be built in one laboratory on a couple of optical tables.

A reviews on recent experiments in the field of ultrafast X-ray science can be found in [11, 12]. Research has been done in the following main areas:

1) Ultrafast melting: The sample under study is excited by an ultrashort (sub-ps) intense laser pulse. It causes changes in the electron distribution function leading to changes in the atomic interaction potential so that the matter loses crystalline order and becomes molten on a sub-ps time scale. The melting can be seen by observing a large decrease of the integrated intensity of the Bragg-reflections. More details on the experiments of this type are presented in [9, 10, 13-17].
2) Coherent optical phonons: The sample under study is excited by a sub-ps laser pulse with an intensity under the melting threshold. Again, the electronic excitation leads to impulsive changes of the interatomic forces and to the coherent excitation of optical phonons. This changes the geometrical structure factor which influences the integral intensity of the diffraction signal. A description of the experiments on this topic can be found in [18, 19].
3) Coherent acoustic phonons: The sample under study is excited by an ultrashort (sub-ps … few ps) laser pulse with an intensity below the melting threshold. The impulsive stress caused by the optical excitation pulse relaxes by generating coherent acoustic waves, as was first described by Thomsen et al. in [20, 21]. The coherent acoustic strain waves are seen as changes of the angular X-ray diffraction profile over time. Some recent experiments on this topic can be found in [22-33]. More information about experiments of this type and the investigations of the coherent acoustic phonons made by the author are presented in section 4.3.

The experiments performed for this thesis were carried out using a laser-plasma based X-ray source at the “Institut für Experimentelle Physik” at the University of Duisburg-Essen.

1.2. Overview and structure of the thesis

The structure of this thesis is as follows:

Section 1.3 discusses the generation of ultrashort X-ray pulses by focusing intense femtosecond laser pulses onto the surface of a solid material.

Chapter 2 contains a description of the terawatt laser system, the laser-plasma based X-ray source and the experimental setup used for time-resolved X-ray diffraction.

Chapter 3 presents the characterization and comparison of different types of X-ray optics used for point-to-point imaging of femtosecond X-ray pulses emitted by a point-like X-ray source.

Chapter 4 describes the results of the time-resolved X-ray diffraction measurements upon irradiation with femtosecond optical pulses. It consists of three sections:

- The first section discusses initially unexpected large transient changes of the diffraction signal observed in a thin Germanium film. The observed changes were explained in terms of the thermo-acoustic response of the sample when inhomogeneously strained material is probed by divergent X-ray beams.

- The second section presents the direct observation of the build-up of non-coherent lattice vibrations in Germanium during intraband relaxation of the excited carriers. It was found that the energy of excited electrons in Germanium is transferred to the lattice in just over one picosecond.

- The third section describes time-resolved measurements of the acoustic phonons in a thin Germanium film. The measured data were interpreted and fitted with a theoretical model describing the acoustic response of the lattice upon ultrafast optical excitation. The theoretical model allowed interpretation

of the measured acoustic phonon dynamics and made it possible to estimate the relative strength of the thermal and electronic pressure contributions in Germanium after ultrafast optical excitation.

The summary contains an overview of the main results presented in this thesis.

1.3. Generation of ultashort X-ray pulses from laser produced plasmas

This section discusses the generation of ultrashort keV X-ray pulses by focusing an intense femtosecond laser onto the surface of a solid material.

The optical radiation is absorbed by a metal within a thin layer of about 10 nm which is called 'skin depth' [34]. If the intensity of the laser radiation that excites the material is large enough, then the target material within the skin depth will be practically fully ionized and transformed into plasma. It was found that for moderate intensities below 10^{18} W/cm^2 the radiation emitted by the plasma consists of the characteristic line emission (K_α, K_β, …) and Bremsstrahlung radiation that appears due to the interaction of hot (~10…100 keV) plasma electrons with the material [35-38]. The laser radiation intensity of 10^{15}-10^{18} W/cm^2 can be achieved by focusing a femtosecond laser pulse with an energy of ~0,1 J onto a spot of about 10 μm in size.

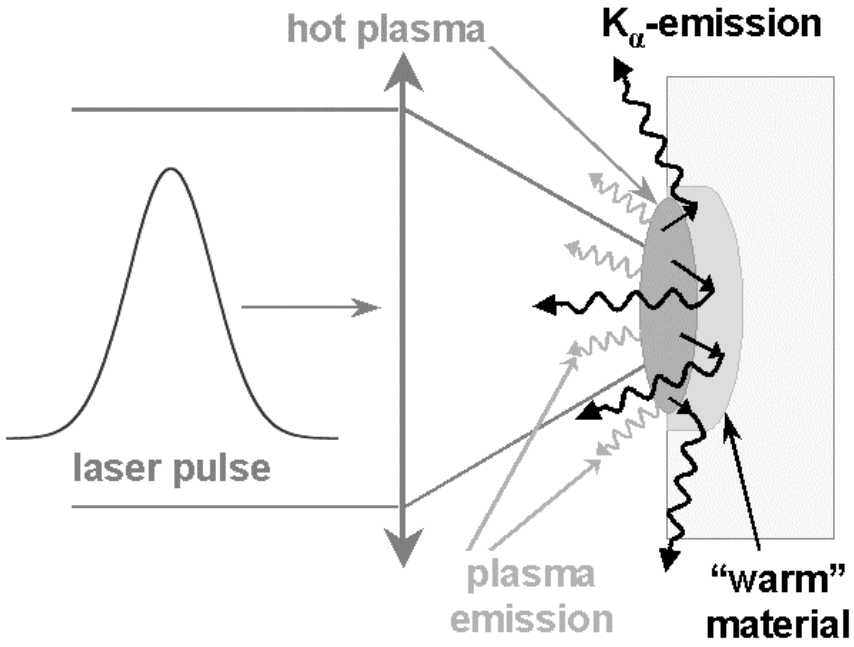

Figure 1.1. Scheme of K_α radiation generation by focusing an ultrashort laser pulse with high intensity onto a solid target.

The generation of characteristic line radiation during irradiation of a solid material with an intense femtosecond laser pulse is described in [37, 39-41]. A short description of this process is given below.

Figure 1.1 illustrated the process of K_α radiation generation when a solid is excited with a high intensity femtosecond laser pulse. The laser pulse front generates a plasma with a high electron concentration on the target surface. The plasma electrons, interacting with the strong electric field of the incident femtosecond optical pulse, can acquire an energy which is high enough to leave the skin layer and enter the deeper layers of the non-excited material. Electrons entering the non-excited material, are shown schematically in figure 1.1 by black arrows. These electrons collide with the non-excited atoms, kick out electrons from their inner electronic shells and thereby produce core holes. The recombination of the holes with outer shell electrons subsequently takes place, and the characteristic line radiation is emitted. This mechanism is very similar to that in an ordinary X-ray tube, but the significant difference is the duration of the characteristic line radiation. The emission of the characteristic line radiation depends on the presence of high energy electrons. These exist only during the femtosecond laser pulse irradiation and for a very short time afterwards which is determined by the flight-time of the hot electrons through the material of the sample. Thus, one can expect the duration of the X-ray pulses produced in this way to be comparable with the duration of the laser pulses, which means that in this way one can produce femtosecond X-ray pulses [42-45].

The size of the area emitting X-rays is comparable to the size of the laser beam focal spot which is typically about 10 μm. The characteristic X-ray radiation is emitted by atoms into the whole 4π solid angle.

Different working groups have investigated the generation of the K_α radiation from the laser-produced plasmas in different materials, such as Silicon, Calcium, Aluminum, Iron, Copper, and Titanium and used this radiation for time-resolved X-ray diffraction experiments [7, 13, 22, 24, 37, 41, 43-48].

A detailed description and characterization of the laser-plasma based X-ray source used for the time-resolved X-ray diffraction experiments described in this thesis is given in section 2.2.

2. Experimental setup

2.1. 10 Hz Titanium-Sapphire laser system

This section contains basic information concerning the principle of operation of the laser system used as a driver for a plasma based X-ray source, and some data on the laser stability.

The 10-Hz Titanium-Sapphire femtosecond terawatt laser system in the “Institut für Experimentelle Physik” at the University of Duisburg-Essen is based on chirped pulse amplification [49, 50]. This means that a femtosecond pulse produced by an oscillator first passes through a device called a “stretcher”, which adds a controlled dispersion to the laser pulse and thereby increases the pulse duration and decreases the peak intensity. The “chirped” pulse is then amplified by an amplifying system. Finally, it travels through another device, called a “compressor“, which compresses it nearly to its initial duration. The advantage of this scheme is that the intensity of the pulse during amplification is kept small. It allows the deterioration of the pulse parameters due to nonlinear effects in the amplifier to be minimized, and the damages to the optical components in the amplifying system to be avoided. The main parameters of the laser system are listed in table 2.1:

Average wavelength	800 nm
Spectral width	21 nm
min. pulse duration	45 fs
max. pulse energy	150 mJ
contrast ratio at 2 ps	10^{-7}
repetition rate	10 Hz

Table 2.1. Main parameters of the laser system.

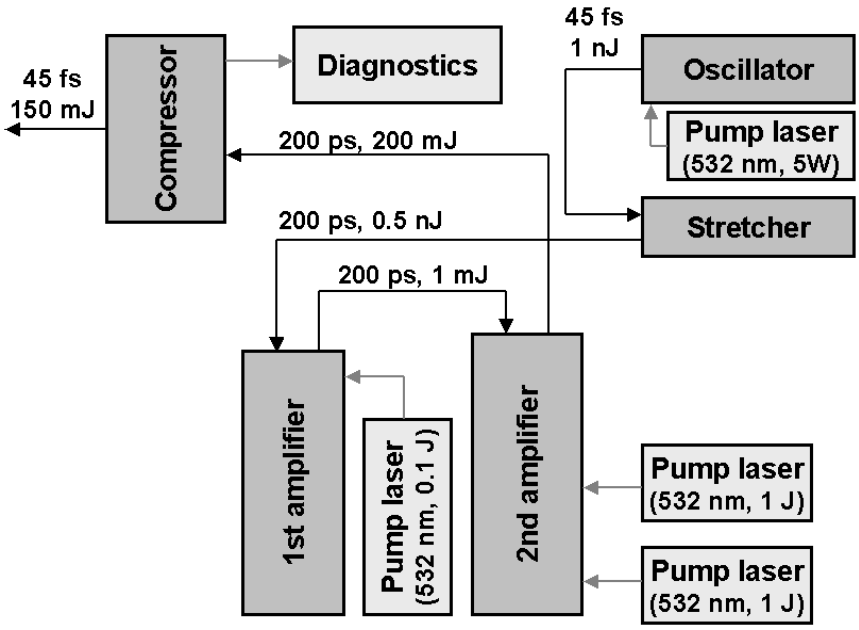

a)

b)

Figure 2.1. Laser system: a) the principle scheme of the laser system; b) a photograph of the laser system.

The main components and a photograph of the laser system are shown in figure 2.1.
The "heart" of the laser system is a mode locked Titan-Sapphire oscillator. It produces a train of 45 fs pulses with the repetition rate of 80 MHz and the energy ~1 nJ per pulse. The central wavelength of the pulses is 800 nm. The spectral width is 21 nm FWHM (full width at half maximum). The oscillator is "pumped" by the second harmonic Nd:YLF cw laser (λ=532 nm, P=5W).

Each pulse from the oscillator is directed to the stretcher. Due to its high dispersion the stretcher broadens the pulses up to 200 picoseconds. Commercial Jobin Yvon gratings with 1200 lines/mm are used in the stretcher as dispersive elements for broadening the pulses. For further amplification, single pulses with the repetition rate of 10 Hz are selected from the initial pulse train by an optical pulse selector consisting of Pockels cells.

The amplifying system consists of two multipass stages. The amplifying medium in each of the stages is a Titanium-Sapphire crystal pumped by the second harmonic of Nd:YAG lasers (λ=532 nm).
The first stage represents an 8-pass amplifier whose amplification is about 10^6-10^7. The energy of the "chirped" pulse after the amplification is about 1 mJ.
The second stage representing a four-path amplifier increases the energy of the pulse up to ~200 mJ (the amplification is $>10^2$).

Finally, the amplified pulses enter the compressor. The compressor contains dispersive elements (gratings) which compensate the dispersion of the pulses added by the stretcher and thereby compress the pulses nearly to their initial duration before stretching.

Stability of the laser pulses coming out of the compressor plays an important role in performing the experiments using the laser system. Two types of stability are especially interesting for the experiments described in this thesis: a) pointing stability and b) energy stability.

a) Pointing stability describes the angular shift of the laser beam during the course of time. It is significant when an experiment requires focusing of the pulses on some target. In this case the angular shift of the beam will lead to the shift of the focal spot, and consequently to the partial or total misalignment of the experimental setup.
To investigate the pointing stability the following experiment was performed. A laser beam was focused with a 1m focal length lens and the position of the focal spot ("centre of gravity") was recorded for each laser pulse with the help of a CCD-camera placed in the focal plane of the lens. The measured positions of the focal spots for a sequence of 500 laser pulses are shown in figure 2.2.

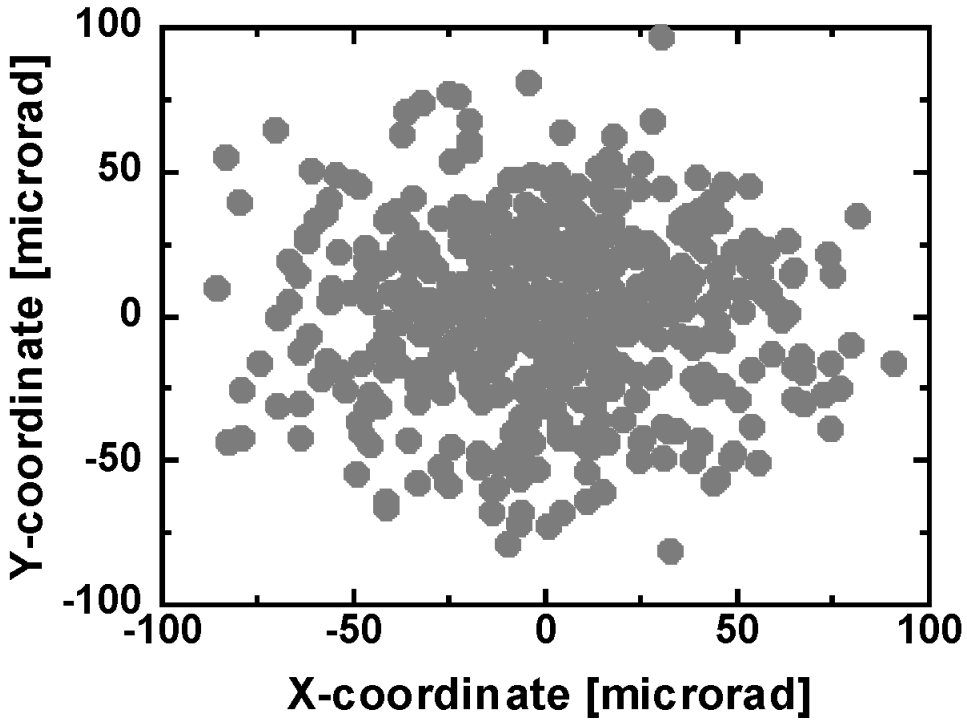

Figure 2.2. Pulse-to-pulse pointing stability of the laser system.

The measured pulse-to-pulse pointing instability of the laser pulses is about 35 microradian (RMS). This value is comparable with the divergence of the laser radiation. So, for λ = 800 nm and for the diameter of the beam d = 2.5 cm (FWHM) the divergence of the radiation is λ/d = (800 nm) / (2.5 cm) = 32 microradian.

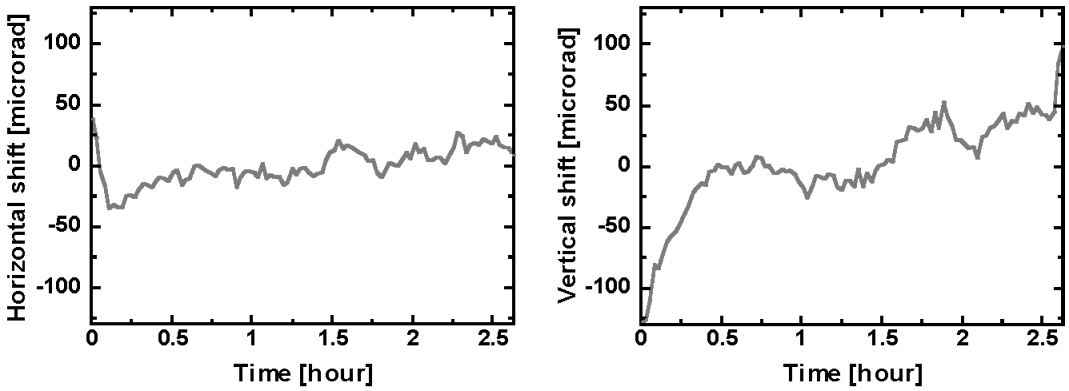

a) b)

Figure 2.3. Angular shift of the laser beam over time: a) vertical direction; b) horizontal direction.

Information on pulse-to-pulse pointing stability is especially important for single pulse experiments. For experiments which take hours, it is important to know if there is an angular drift of the laser beam on a long time scale. Figure 2.3 shows how the position of the focused laser beam averaged over 500 pulses changes during the course of couple of hours. From the measured data, it is seen that the laser system has an excellent long time scale pointing stability (less than 100 microrad).

b) Another important characteristic of the laser system mentioned above is the energy stability. The energies of the fundamental pulses and of the second harmonic (SH) pulses were recorded during the experiment. The information on the second harmonic stability is important for steady X-ray production and for experiments where the samples need to be excited with 400 nm wavelength instead of 800 nm. Temporal dependencies of the fundamental and the second harmonic signals averaged over 500 laser pulses are depicted in figure 2.4. One can see from figure 2.4 that the energies of the fundamental and the second harmonic are stable during hours of continuous operation of the laser system within ~3% and ~10%, respectively. Standard deviations of the fundamental (800 nm) and the second harmonic (400 nm) signals for a sequence of 500 laser pulses were ~2.5 and ~7 %, respectively.

The measured instability of the second harmonic is larger than that of the fundamental pulses. This is due to the fact that second harmonic generation is a non-

linear process in which the intensity of the SH is determined by the square of the fundamental beam intensity. Thus, small changes in the laser intensity should lead to twice larger changes in the SH intensity. As the intensity of a laser pulse is determined by its energy, its duration and its beam size, one can draw the conclusion that the measured changes of the second harmonic signal which are twice larger than the changes in the fundamental energy are due to variations (~2%) of the laser pulse duration and/or fluctuations of the beam profile.

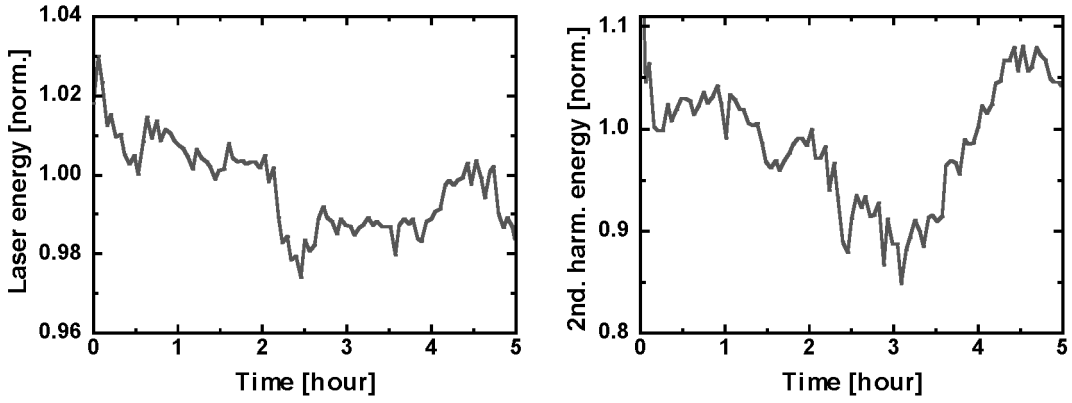

a) b)

Figure 2.4. Energy stability of the laser system over time: a) 800 nm fundamental beam; b) second harmonic.

The stability of the laser system is determined mostly by the stability of the pulses produced by the oscillator and by the pump-lasers in the amplifiers. It is mostly influenced by changes in the environment temperature. The measurements presented here were done for typical temperature drifts of about one degree.

The stability measurements described in this section revealed that the laser system can be used for experiments requiring high accuracy.

2.2. X-ray source

Section 1.3 gave a description of the ‘simple’ and ‘cheap’ (in comparison with synchrotrons [44-47]) method of generating subpicosecond X-ray pulses by focusing a short laser pulse on an appropriate target.
This section discusses the laser-plasma based X-ray source used in the experiments described in this thesis.

A photograph of the X-ray target is shown in figure 2.5. A thin wire (diameter 250 μm) of titanium or copper was used as a target.

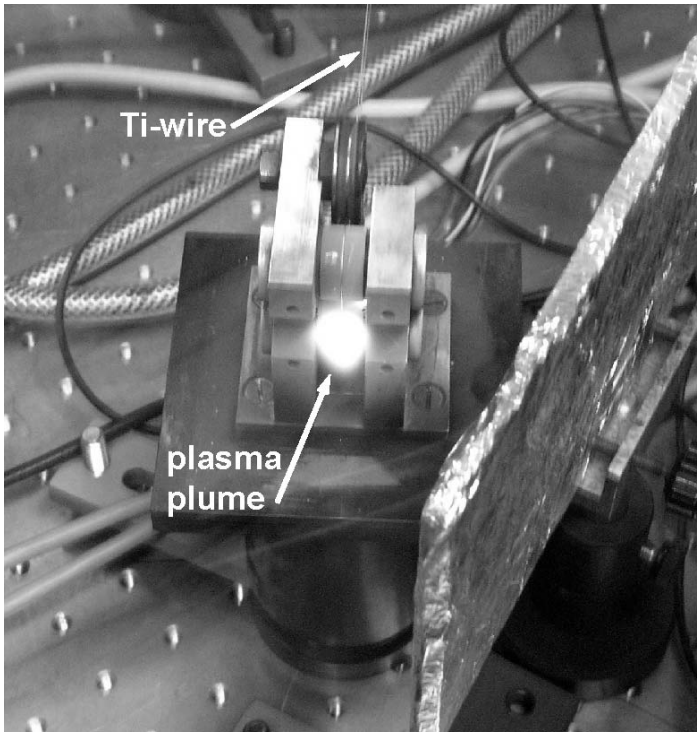

Figure 2.5. A photograph of the X-ray target. During the experiment a wire is continuously pulled through the cone shape grooves of the wheels.

The wire was constantly pulled through the focus of the lens focusing the laser pulses in order to ensure a fresh spot for each laser pulse. The pulling of the wire during the experiment is necessary because the intensity of the focused laser pulse is so high that the surface of the wire is irreversibly destroyed already after the first laser pulse.

Bobbins with 500 m wire length were used for the experiments. This length is enough for one week's continuous operation of the X-ray source. The possibility of performing an experiment uninterrupted for such a long period of time and the compactness of the construction are the main advantages of using the wire target as compared with other geometries of the target, such as a rotating disk or a flat plate placed in the focus of the laser beam and constantly shifted by means of large translation stages.

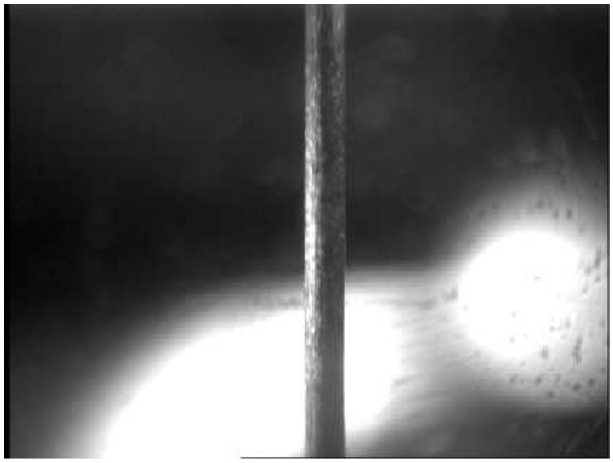

Figure 2.6. Image of the wire on the CCD-camera chip. The white and dark regions in the image background are due to non-homogeneous lighting.

The following experiment was performed to measure the stability of the wire position at the laser focus. With the help of an objective the wire was imaged onto the chip of a CCD-camera. The image is shown in figure 2.6. Having filmed the image of the moving wire, it was found that the deviations (vibrations) of the wire around its average position were less than 5 μm in all directions. The experiments described below will show that these wire vibrations are small enough to ensure the stable generation of X-ray radiation.

It should be noted that the X-ray generation needs to take place in vacuum as this avoids:

a) absorption of X-ray radiation in air (Ti-K_α radiation has an absorption depth in air of only ~15cm) and

b) undesirable nonlinear optical effects in air due to the high intensity of the focused laser radiation.

In the experiments the laser radiation was focused on the wire by a 300 mm focal length lens. The focused laser radiation produced a plasma. The light emitted by the plasma can be seen in figure 2.5. The X-ray radiation coming out from the target consists mainly of the characteristic Ti-K_α radiation with a quantum energy of 4.51 keV (λ = 0,275 nm).

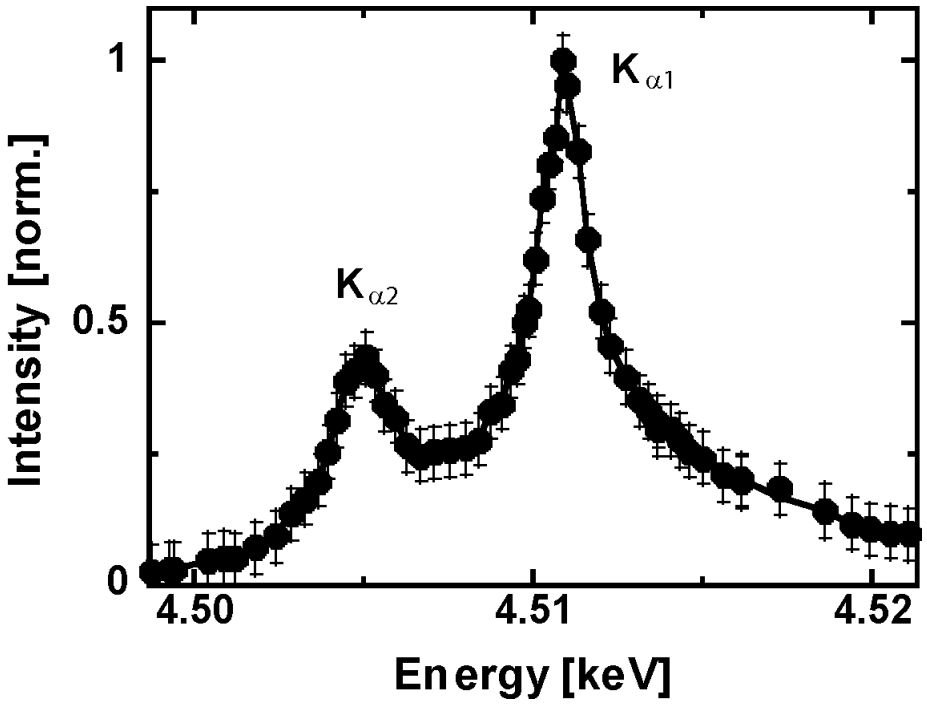

Figure 2.7. The X-ray source spectrum of radiation. The points represent the measured values. The line is a guide for the eye.

The measured spectrum of radiation of the X-ray source is depicted in figure 2.7. The spectrum was measured with the help of a toroidal crystal, used as a spectrometer. The detailed description of the toroidal mirror used for this measurement is given in section 3.1. The resolution of such a spectrometer is determined by the rocking curve width of the Bragg-reflection the mirror is designed for. In the case of the used optic it is the Ge (400) Bragg-reflection. Only the radiation in the energy interval

determined by the width of the rocking curve is diffracted by the toroidal mirror. The energy of the radiation diffracted from the crystal is determined, according to the Bragg condition, by the angle of incidence. Thus, by turning the crystal (and thereby changing the incidence angle of the X-ray radiation) and measuring the intensity of the diffracted radiation one can measure the radiation spectrum of the source. As one can see in figure 2.7, the high resolution of the measurement described above allows the splitting into the $K_{\alpha 1}$ and $K_{\alpha 2}$ lines of the Ti-K_α source spectrum to be distinctly resolved. It is important to notice that the measured width of the K_α lines is larger than the width of the K_α lines known from literature. For example, the measured FWHM of the $K_{\alpha 1}$ line is approximately 2.5 eV, whereas the literature value is only 1.45 eV [51]. This difference can be explained if one takes into account that for laser-driven plasmas the radiation is not only emitted by singly ionized atoms, but also by multiply ionized atoms. The energy of K_α radiation of multiply ionized atoms differs from the energy of the single-ionized atoms, which should lead to the broadening of the total radiation spectrum, as observed in the experiment.
In order to get radiation of another characteristic wavelength from such an X-ray source one just needs to use a wire made of a different material.

The next important characteristic of the X-ray source is the size of the area emitting X-ray radiation. The size of the X-ray source was measured by means of a 5 μm pinhole camera.

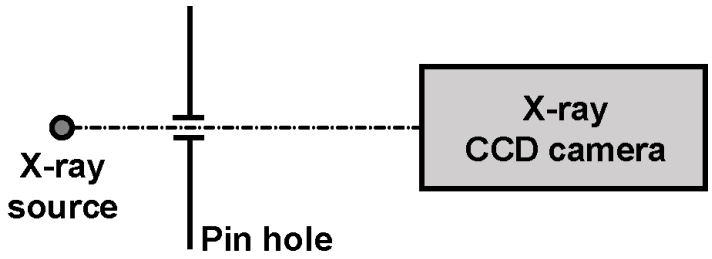

Figure 2.8. Principle scheme of the experimental setup for X-ray source size measurements.

During the experiment the CCD-camera, pinhole and X-ray source were placed on one line as is illustrated in figure 2.8, so that the magnified image of the source was formed on the chip of the CCD-camera. Figure 2.9 presents a magnified image of the X-ray source obtaind with the pinhole. Knowing the distance between the X-ray source and the pinhole ($L_{source\text{-}hole}$) and the distance between the pinhole and the chip of the CCD-camera ($L_{hole\text{-}CCD}$) one can calculate the real size of the X-ray source [52, 53]. For the $L_{source\text{-}hole}$= 43 mm and $L_{hole\text{-}CCD}$= 285 mm (experimental conditions) one can determine from the cross-sections shown in figure 2.9 that the size of the X-ray source is equal to 34 x 29 μm (horizontal x vertical).

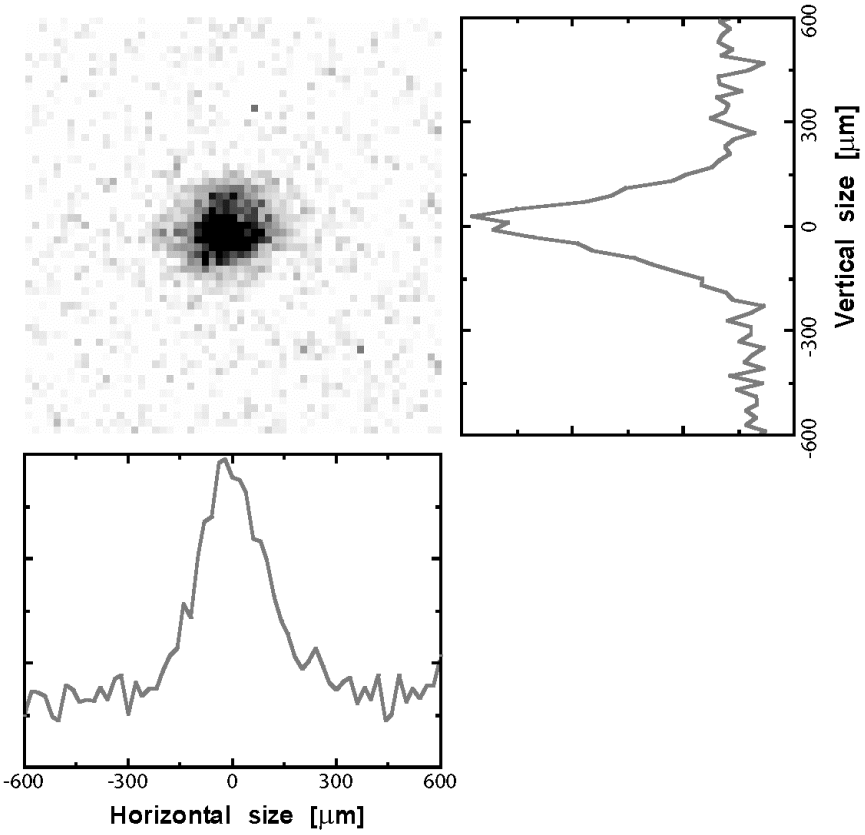

Figure 2.9. The image of the X-ray source, obtained with the pinhole camera.

This size corresponds approximately to the size of the laser focal spot on the wire. The measurement of the X-ray source size was performed using a copper wire as a target. It should be noted that the obtained image of the source is an integrated image over all the wavelengths presented in the spectrum of the source.

2.3. Pump-probe experiment

A usual way to perform time-resolved experiments in the picosecond to femtosecond time-domain is to use the so-called “pump-probe” technique. In a typical pump-probe experiment one initiates a process by applying a laser pulse to a sample and thus “pumping” it. By sending a weak probe pulse with fixed time delays from the pump pulse and then measuring the reflected (and/or transmitted) signal at each time delay one can observe the temporal evolution of the changes in the sample after the optical excitation.

The temporal resolution of a pump-probe experiments is not defined by the resolution of the used detectors, but by the duration of the pump and probe pulses, which are 100 fs or less with modern laser systems.

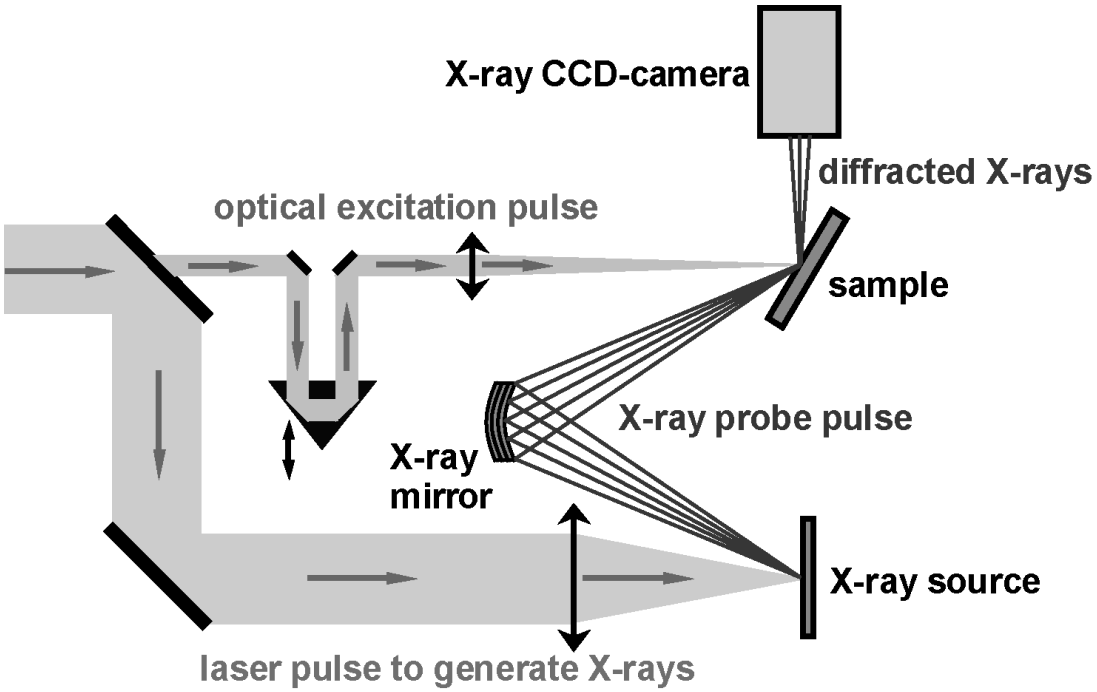

Figure 2.10. Principle scheme of the optical pump/X-ray probe experiment.

As illustrated in figure 2.10 the all-optical pump-probe scheme can be easily modified into an optical pump/X-ray probe experiment to perform for example time-resolved X-ray diffraction measurements. The experimental setup used for the

measurements described in this thesis is based on this scheme. The optical pulses of the laser system are divided into two parts by a splitting mirror. One part is used for the generation of X-rays by focusing it onto a suitable solid target (the source is described in section 2.2). The X-rays produced by this source are collected and focused onto the sample under investigation with the help of a special toroidal X-ray mirror described in section 3.1. The X-rays diffracted from the sample are detected by an X-ray sensitive CCD-camera (type PI·LCX1300, "Roper scientific"). The other part of the laser beam is used for the excitation of the sample. The time delay between the optical pump and the X-ray probe pulses reaching the sample can be easily adjusted by changing the length of the path of one of the pulses (in figure 2.10 it is the optical pump pulse).

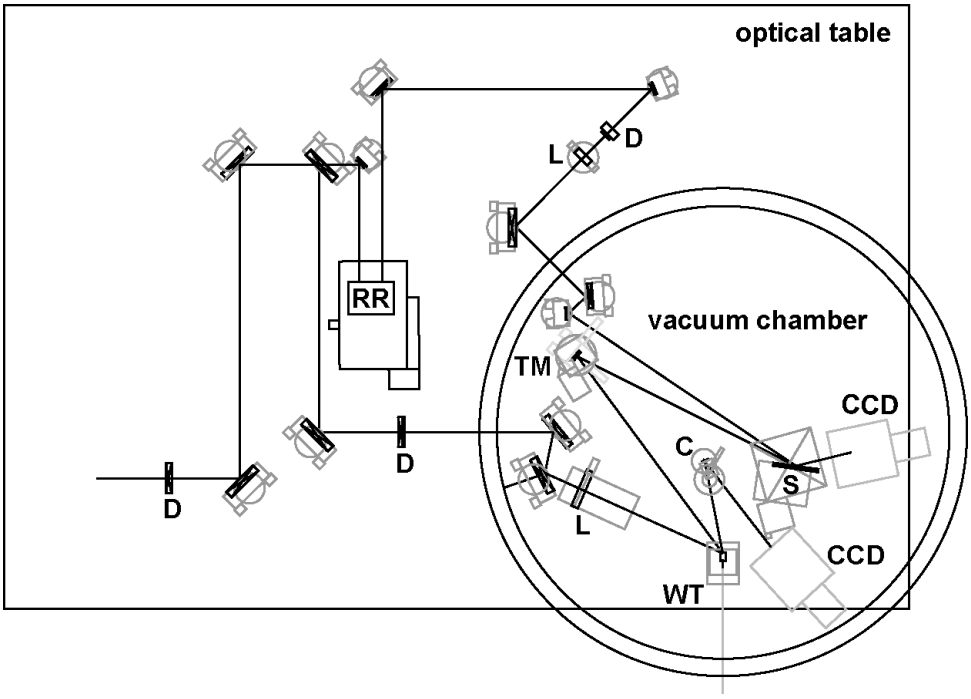

Figure 2.11. A drawing of the experimental setup. Letters D denote diaphragms, letters L denote lenses, TM is the X-ray toroidal mirror, WT is the wire target, C is the GaAs crystal, S is the sample, and RR is the retroreflector. The mirrors for the laser beam are not denoted with letters.

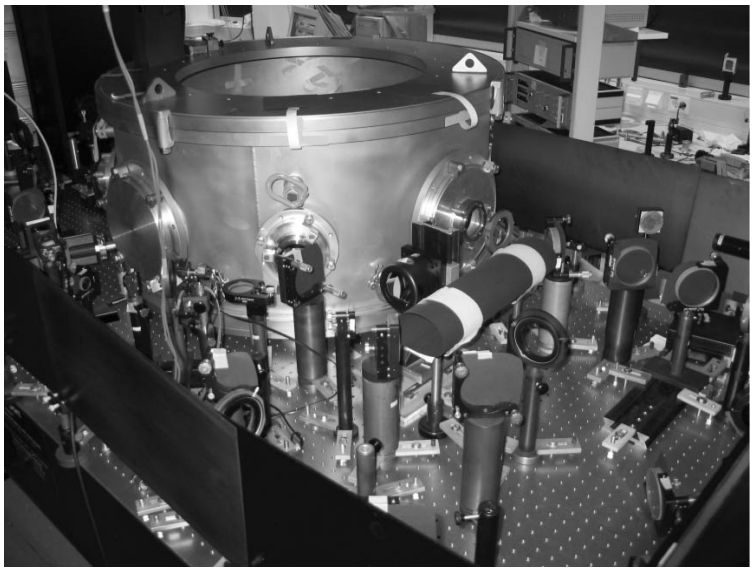

a)

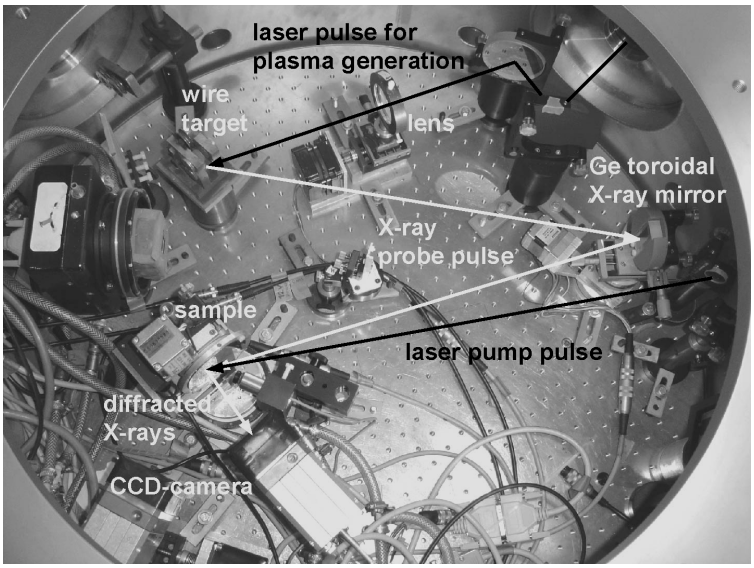

b)

Figure 2.12. Photographs of the experimental setup: a) panoramic view; b) vacuum chamber.

To find zero time-delay between the two pulses the sample was replaced by a non-linear crystal. A second harmonic cross-correlation signal of the pump pulse and the optical radiation scattered from the wire and reflected by the toroidal mirror was observed. The maximum of this signal obtained by varying the time delay between

the two pulses determines time zero. The time-zero can be found in this way with an accuracy of about 200 fs. Figure 2.11 contains a technical drawing of the experimental setup with all the significant elements.

The arrangement and distances between the elements on the drawing correspond to the arrangement and distances in the real experimental setup. In addition to the elements described in figure 2.10 the experimental setup contains a small GaAs crystal marked in figure 2.11 as “C”, whose diffraction signal serves as a reference of the X-ray production. Photographs of the experimental setup are shown in figure 2.12. Figure 2.12.a contains a general (panoramic) view of the experimental setup on the optical table. Figure 2.12.b shows the arrangement of components in the vacuum chamber. The dark and bright arrows represent the paths of the laser and X-ray beams, respectively.

2.4. Stability of X-ray production

The changes in the intensity of the diffracted signal which have to be detected in the experiments for this thesis are in the order of a couple of percent. That is why it is important to determine how accurately the intensity of the diffracted signal can be measured.

The stability of the source X-ray production was measured by observing the diffracted signal from a reference GaAs crystal as discussed in section 2.3. Grey triangles in figure 2.13 represent the measured flux of the X-ray source plotted versus time. Each point corresponds to the signal integrated over a two minute time interval. The standard deviation of the measured points is 5 %. This value is compatible with the value of the energy stability of the laser system.

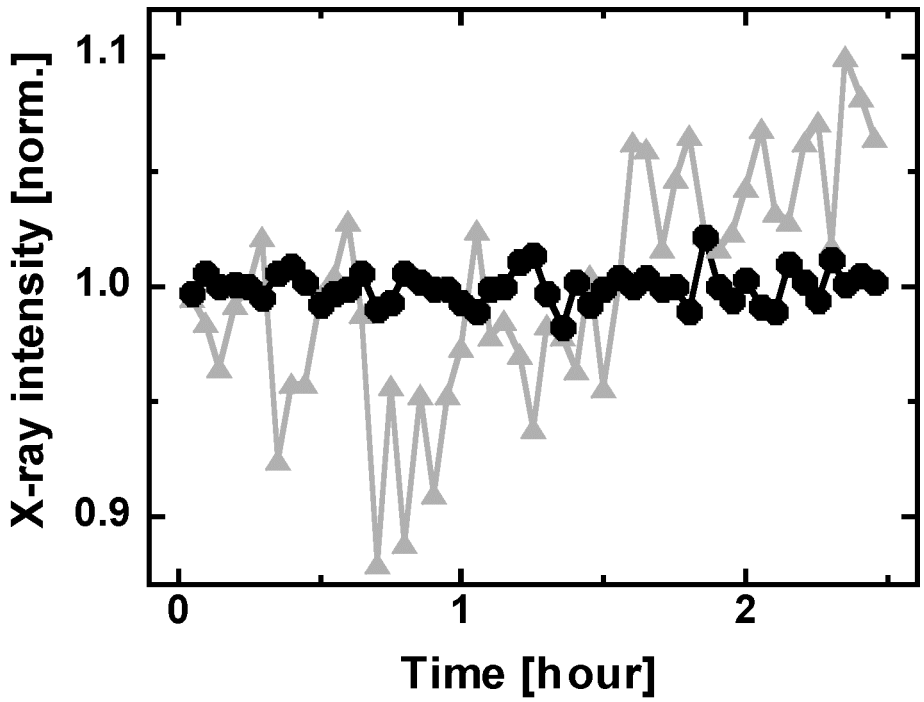

Figure 2.13. Stability of X-ray production. Grey triangles reveal the flux of the X-ray source measured with the GaAs crystal as discussed in section 2.3. Filled circles depict the Ge (111) signal normalized to that of the GaAs crystal.

The filled circles in figure 2.13 depict the measured signal diffracted by the sample normalized to that of the reference GaAs crystal. A 150 nm monocrystalline Germanium film was used as a sample and the Ge (111) reflection was observed. The standard deviation of the normalized points is 0.7 % which is approximately a factor of seven less than the fluctuations in X-ray production.

This demonstrates that by using proper normalization TRXD experiments can be performed at the required level of accuracy.

3. X-ray focusing optics

In order to perform a time-resolved X-ray diffraction experiment one needs to have as much radiation of the X-ray source as possible on the sample under investigation. The radiation of accelerator based X-ray sources usually represents a well collimated beam. In contrast, the radiation of laser-plasma based X-ray sources is emitted into the full solid angle. To directly use this radiation, the sample under investigation needs to be positioned as close as possible to the X-ray source in order to get the required necessary flux density of the X-ray radiation. This close proximity requirement between the sample and X-ray source imposes strong limitations on the experimental geometries and makes it effectively impossible to carry out certain experiments. These limitations can be overcome by using special optics which allow the X-rays emitted by the source to be collected and focused onto the sample under investigation. X-ray optics represent key-components in a setup for TRXD pump/probe experiments with laser-plasma based X-ray sources. This chapter discusses the results of the characterization and comparison of three different types of point-to-point imaging X-ray optics: a) toroidally bent crystals; b) capillary optics and c) two kinds of multilayer optics.

3.1. Toroidal mirrors

This section discusses the results of the characterization of toroidally bent crystals which allow monochromatic point-to-point imaging of the femtosecond X-ray pulses.

The principle of operation

The X-ray toroidal mirror consists of a thin crystal platelet attached to a thicker, toroidally shaped glass substrate.

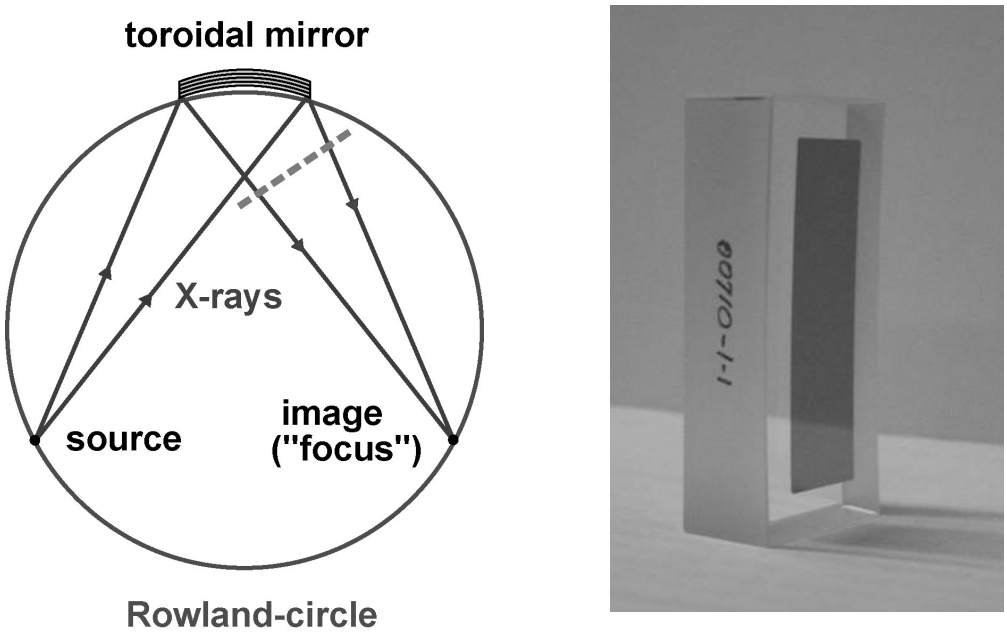

a) b)

Figure 3.1. a) imaging of the point-like source using a Rowland-circle geometry;
b) a photograph of the Germanium toroidal X-ray mirror.

Curving the crystal planes in two directions to form a toroidal surface allows one-to-one imaging of the point-like X-ray source onto the sample [54]. The radii of curvature of the mirror in horizontal R_h and vertical R_v directions should satisfy the condition $R_h / R_v = \sin^2(\Theta_B)$ in order to get the same focal distances of the mirror in the horizontal and vertical directions and thereby achieve 1:1 imaging. In order to

satisfy the Bragg condition over the entire area of the mirror the X-ray source and the sample should be located on the Rowland circle in a symmetrical configuration (see figure 3.1.a) [54].

The spectral width of the radiation reflected by the toroidal mirror is determined by the rocking curve of the mirror. Thus, if the spectrum of the X-ray source is broader than the spectral width of the rocking curve then the mirror also works as a monochromator reflecting only the wavelengths near the wavelength determined by the Bragg condition.

The main technical data of the tested toroidal mirrors are summarized in table 3.1.

	Mirror No. 1	Mirror No. 2
Size	12.5 x 40 mm^2	
Orientation	(111)	(100)
Orientation error	< 10 ’’	
Bragg-reflection	(444)	(400)
Wavelength	Cu K_α	Ti K_α
Bragg-angle	70.6°	76.4°
R_h	496.5 mm	498.6 mm
R_v	441.8 mm	473.7 mm
Thickness	90 μm	

Table 3.1. Technical data of the tested toroidal mirrors.

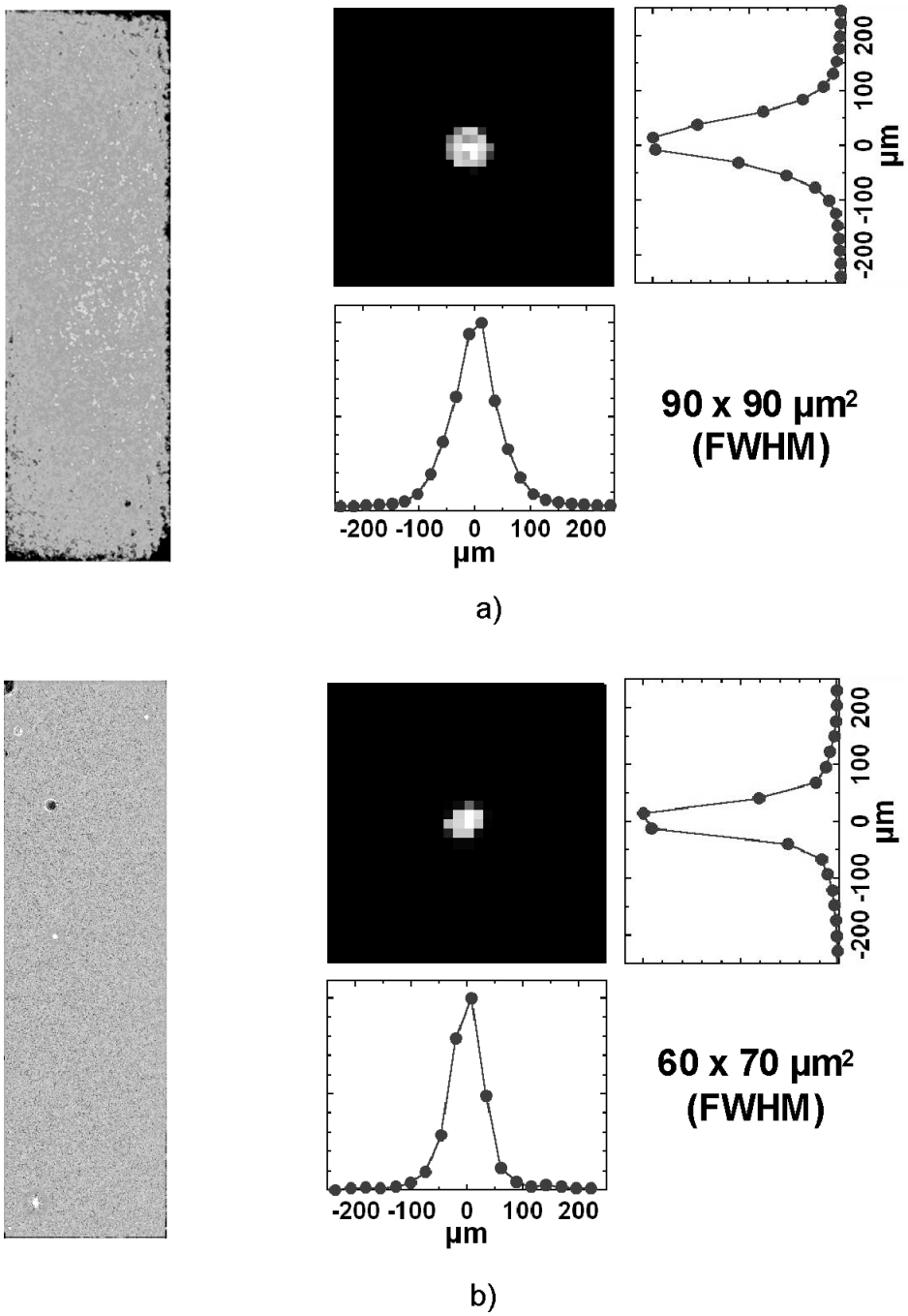

Figure 3.2. Spatial X-ray distribution in the topography (left side) and in the focal plane (right side). The graphs depict corresponding horizontal and vertical cross-sections of the X-ray distributions in the focal plane: a) mirror No. 1; b) mirror No. 2.

The total efficiency of the tested mirrors can be estimated as the ratio of the mirror bandwidth over the FWHM of the corresponding K_α radiation spectrum multiplied by the solid angle of the X-rays reflected by the mirror divided by 4π. The bandwidths of the Ge (444) and Ge (400) reflections of flat crystals are 0.1 eV and 0.26 eV, respectively. Taking into account the large radii of curvature of the toroidal mirror these values can be also taken as an approximation for the bandwidth of the toroidal mirror [55]. Using the geometrical parameters listed in table 3.1 one obtains the diffraction efficiency of $1.8 \cdot 10^{-6}$ and $1.1 \cdot 10^{-5}$ for the Cu-K_α and Ti-K_α mirrors, respectively.

These two mirrors were specially designed for the experimental setup described in this thesis. Previous experiments had demonstrated the successful use of similar toroidal mirrors for TRXD measurements [15, 18]. However, small radii of curvature and consequently small working distances of the previously used mirrors led to significant geometrical restrictions. In particular, it was not possible to observe some of the desired Bragg-reflections. The new mirrors described here have improved diffraction efficiency and larger working distances compared with the previously used toroidal mirrors. This enabled some of the geometrical restrictions imposed by the old mirrors to be removed. A photograph of the new toroidal mirror (No: 2) is shown in figure 3.1.b.

The spatial X-ray intensity distributions were measured in the focal plane and in the “topography” plane close to the mirror surface for both of the mirrors. The topography plane is shown in figure 3.1.b by the dashed line. The distribution of X-rays measured in this plane shows the uniformity of the reflected X-rays over the mirror surface.

Figures 3.2.a and 3.2.b illustrate the spatial X-ray distributions in the topography and focal plane for mirror No. 1 and mirror No. 2, respectively. The topography pictures reveal quite a uniform X-ray reflectivity over the entire mirror surface with only some point-like imperfections. The sizes of the focal spots for both mirrors are less then 100 μm (FWHM). It should be noted that the measured spot sizes represent convolutions of the imaging properties of the optics and the X-ray source size.

The X-ray phonon flux in the focal spot of the Ti-K_α toroidal mirror (No. 2) is ~$5 \cdot 10^4$ Ti-K_α photons per pulse. The X-ray phonon flux was measured for a laser energy of about 130 mJ and a laser pulse duration of about 120 fs. The flux in the focal spot of the Cu-K_α mirror (No. 1) was measured to be equal to ~$6 \cdot 10^3$ photons per pulse for a laser energy of about 90 mJ and a laser pulse duration of about 120 fs. Using the total efficiency of the mirrors one can estimate the number of X-ray photons emitted by the source into the full solid angle. For the data mentioned above one obtains that the Ti-K_α and Cu-K_α sources emit $4.5 \cdot 10^9$ ph/pulse and $3.3 \cdot 10^9$ ph/pulse into 4π solid angle, respectively.

3.2. Multilayer optics

This section presents the characterization and comparison of two different types of multilayer optics for focusing femtosecond X-ray pulses: a) toroidal single bounce mirror (SBM) and b) so called Montel optic, consisting of two elliptical multilayer mirrors.

The principle of operation

Multilayer optics are based on Bragg-reflection at multilayer systems. Multilayer optics, in comparison with toroidal mirrors, have a higher reflectivity of the single layer and thus a small X-ray extinction depth. This leads to the broadening of the reflected bandwidth compared with that of the toroidal mirrors. Typically multilayer optics are designed so that the whole K_α emission (including the $K_{\alpha 1}$ and $K_{\alpha 2}$ lines) can be reflected.

Single-bounce multilayer mirror

A single-bounce multilayer mirror is a two-dimensional focusing mirror, which has a toroidal surface consisting of laterally graded multilayers.

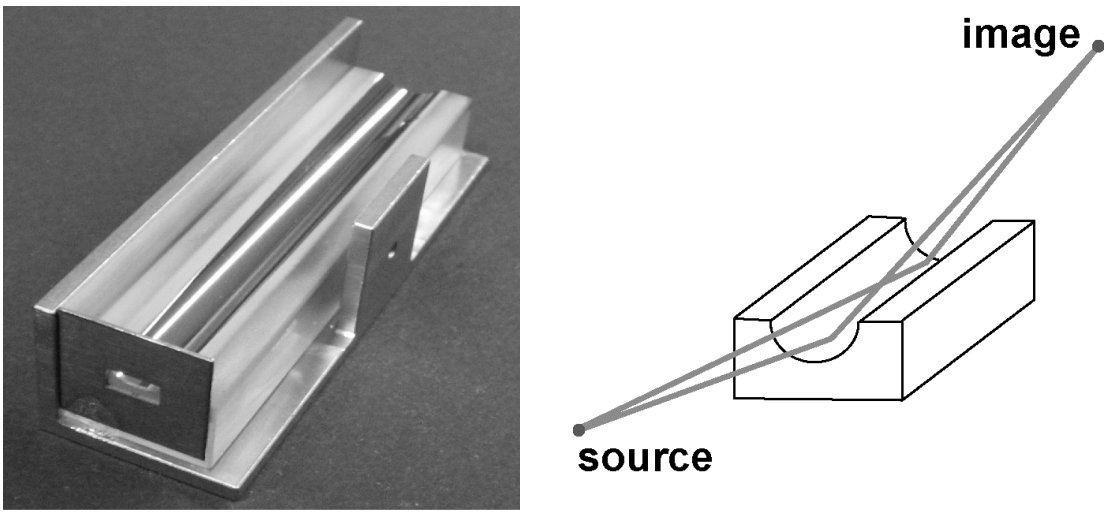

a) b)

Figure 3.3. SBM optic: a) photograph; b) the principle of operation.

A photograph and the principle of operation of the SBM are shown in figure 3.3. A SBM optic recollects and focuses X-rays emitted from a point source to another point which is the image of the X-ray source (see figure 3.3.b). The imaging principle is the same as in the case of the toroidal mirrors described in section 3.1. Lateral gradation of the multilayer thickness ensures that the Bragg condition is satisfied over the whole area of the mirror. The optic characterized here had a magnification of M=3.2.

Montel optics

The second type of optic tested here is a Montel optic [56]. The Montel type of optic is based on the so-called Kirkpatrick-Baez scheme (figure 3.4) [57]. In this scheme consisting of two perpendicular 1-D elliptical mirrors each mirror focuses the radiation from a point source in one dimension. Focusing in two dimensions is achieved by placing two mirrors close to one another in a geometry as illustrated in figure 3.4. In this case the X-rays passing through the optic are sequentially reflected by the two mirrors. The paths of the X-rays in this configuration are shown in figure 3.4 by dark and bright lines.

The Montel optic consists of two reflectors arranged in a multilayer-based Kirkpatrick-Baez geometry (figure 3.5).

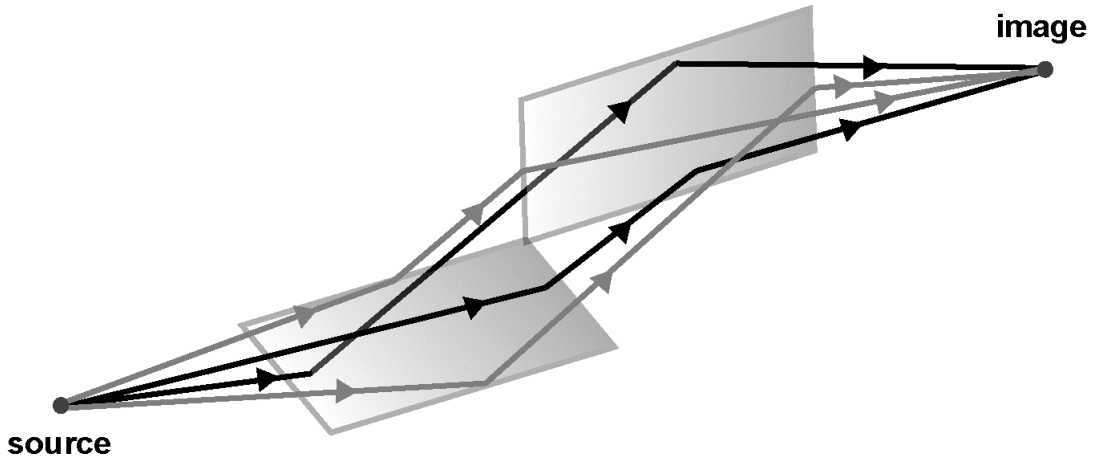

Figure 3.4. Kirkpatrick-Baez system.

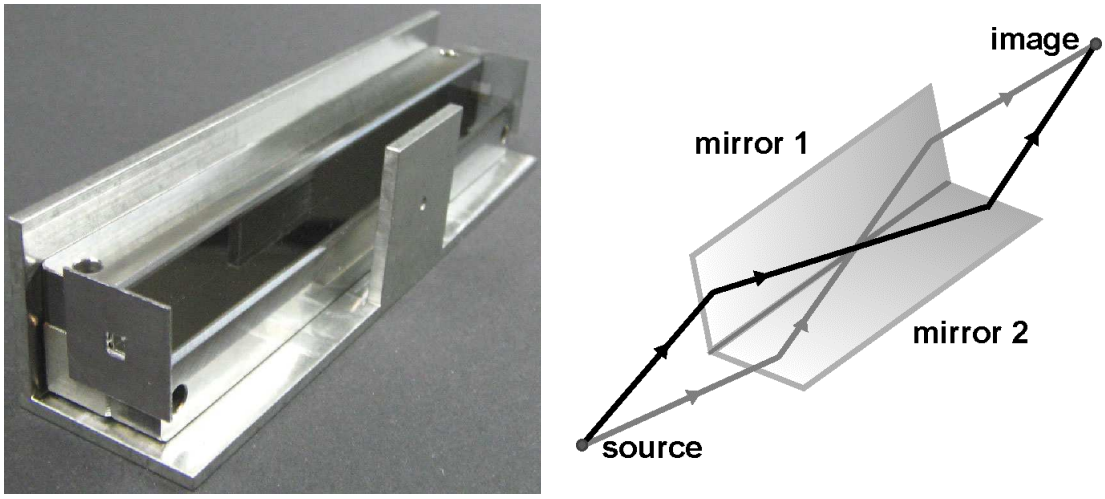

a) b)

Figure 3.5. Montel optic: a) photograph; b) principle scheme.

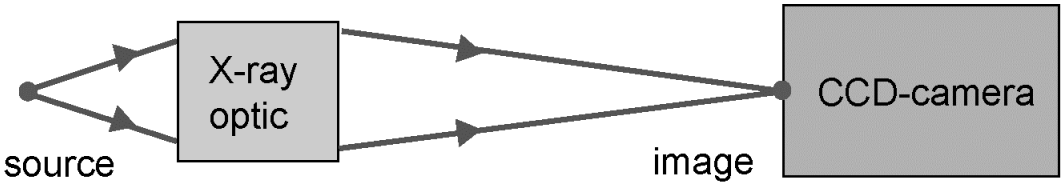

a)

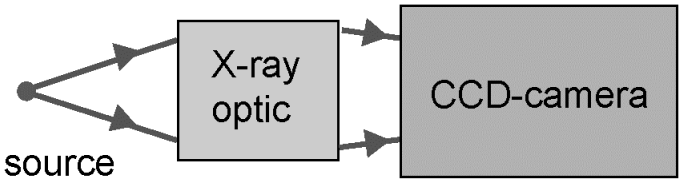

b)

Figure 3.6. Schemes of the experiments for testing of optics: a) measurement of the intensity distribution in the focal spot of the X-ray optic; b) measurement of the topography.

In a photograph of the Montel optic (figure 3.5.a) one can see that both reflectors are longer than the ones in the standard Kirkpatrick-Baez scheme. X-rays can go through the optic along two different paths as shown in figure 3.5.b. When the X-rays follow the first path, they are reflected first from “mirror 1” and then from “mirror 2”. X-rays following the second path are reflected first from “mirror 2” and then from “mirror 1”.
The thickness of the multilayers is also laterally graded along the mirror surface in order to fulfil the Bragg condition at each point of the mirror. It allows X-rays to be collected and focused over a large solid angle. Two different Montel optics with M=2.1 and M=7.3 magnifications are presented in this section.

Testing of the optics

The principle scheme of the experiment to characterize the optics is depicted in figure 3.6. For each optic the X-ray intensity distributions in the image plane (figure 3.6.a) and in the plane located directly after the X-ray optic (figure 3.6.b) were measured.

The distances between the X-ray source, the optic and the CCD-camera shown in the scheme in figure 3.6 are determined by the properties of the optics defined by the manufacturer. These distances and other parameters of the tested optics are listed in table 3.2. The last three columns in the table correspond to the three tested X-ray optics. The first optic is a SBM mirror. The second is a Montel optic with a magnification of M=2.1. The third is a Montel optic with a magnification of M=7.3. The upper part of the table contains parameters of the optics determined by the manufacturer. The lower section of the table shows the experimental data obtained in our laboratory.

Type of optic	SBM	Montel E17	Montel E19
Manufactured properties			
Source-optic distance d_{so} [mm]	120	140	60
Optic-image distance d_{oi} [mm]	380	300	440
Length[mm]	60	100	80
Capturing angle [$mrad^2$]	12x36	17x17	31x31
Magnification	3.2	2.1	7.3
Hor. convergence [deg]	0.64	0.46	0.24
X-ray wavelength [nm]	0.154	0.154	0.154
Experimental data			
Flux in the focus [norm.]	4.3	1	4.9
Angular flux density [norm.]	3.1	1	9.4
Size of the focus (hor. x ver.) [μm]	180 x 120	90 x 90	250 x 140

Table 3.2. Main parameters of the three tested multilayer mirrors. The following parameters of the optics are presented. “Source-optic distance d_{so}” is the distance between the source and the geometrical centre of the optic. “Optic-image distance d_{oi}” is the distance between the geometrical centre of the optic and the image of the X-ray source. “Length” is the length of the optic. ‘Magnification’ is the magnification of the optic determined as a ratio d_{oi}/ d_{so}. ‘Hor. convergence’ is the angular range of the X-rays going out of the optic. ‘Flux in the focus’ is the total number of K_α photons per pulse detected in the focus of the optic normalized to that of the Montel type of optics with a magnification of M=2.1. ‘Angular flux density’ is the number of photons per pulse in a unit angle detected in the focus. “Size of the focus” is the full width at half maximum of the diffracted X-rays distribution in the image plane.

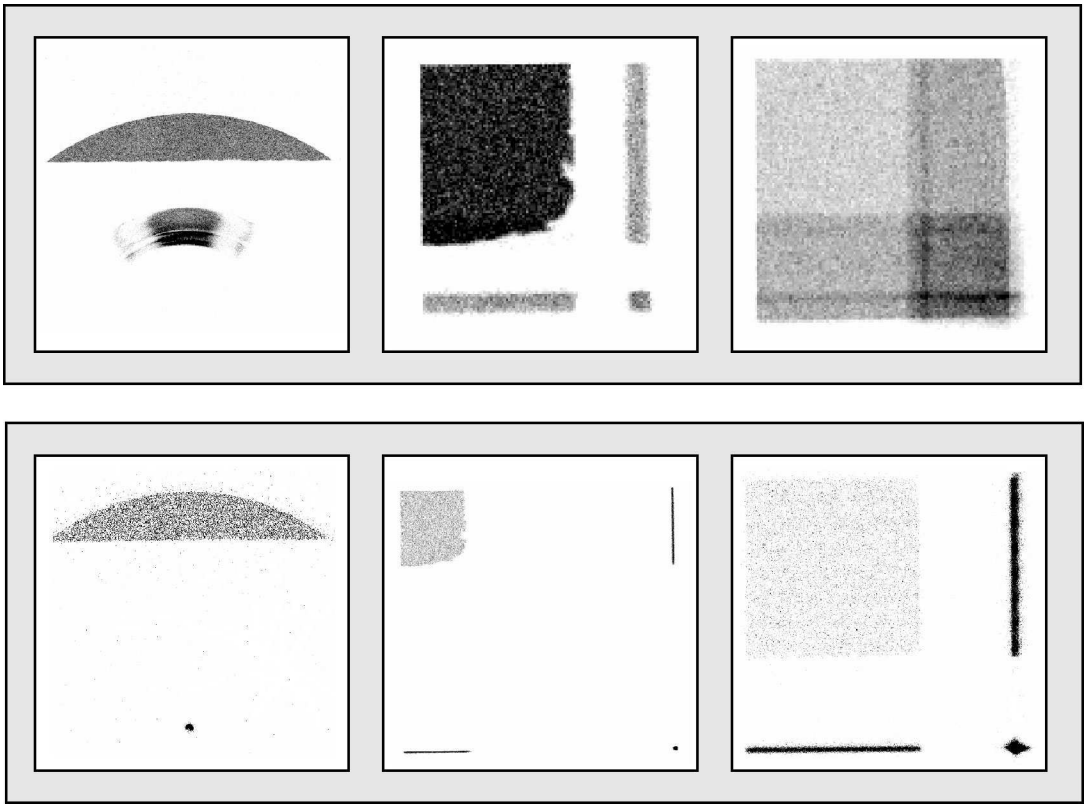

a) b) c)

Figure 3.7. Distributions of X-rays after they have passed through different optics: a) SBM optic; b) Montel optic with a magnification of M=2.1; c) Montel optic with a magnification of M=7.3. The upper panel shows the X-ray intensity distributions directly after passing through the optics. The lower panel depicts the X-ray intensity distributions in the image planes.

The distributions of the X-rays after passing through the optics are presented in figure 3.7. The upper panel shows the distributions when the X-ray detector was placed directly after the optics. The lower panel depicts the distributions in the image planes.

For the SBM optic in both the topography and focus pictures (figure 3.7.a) one can see that the distribution of the radiation passed through the optic consists of two parts. The former is the X-rays going directly through the aperture of the optic (the circle segments at the upper part of the pictures). The latter is the X-rays diffracted by the optic (the arc or the spot at the lower part of the pictures).

For the Montel optic the X-ray radiation passed through the optic consists of three components. The first one is the direct radiation passing through the entrance of the optic without reflections by the multilayer mirrors. It has the shape of a square aperture. The second component consists of two lines which are formed by the X-rays reflected by only one of the two mirrors.

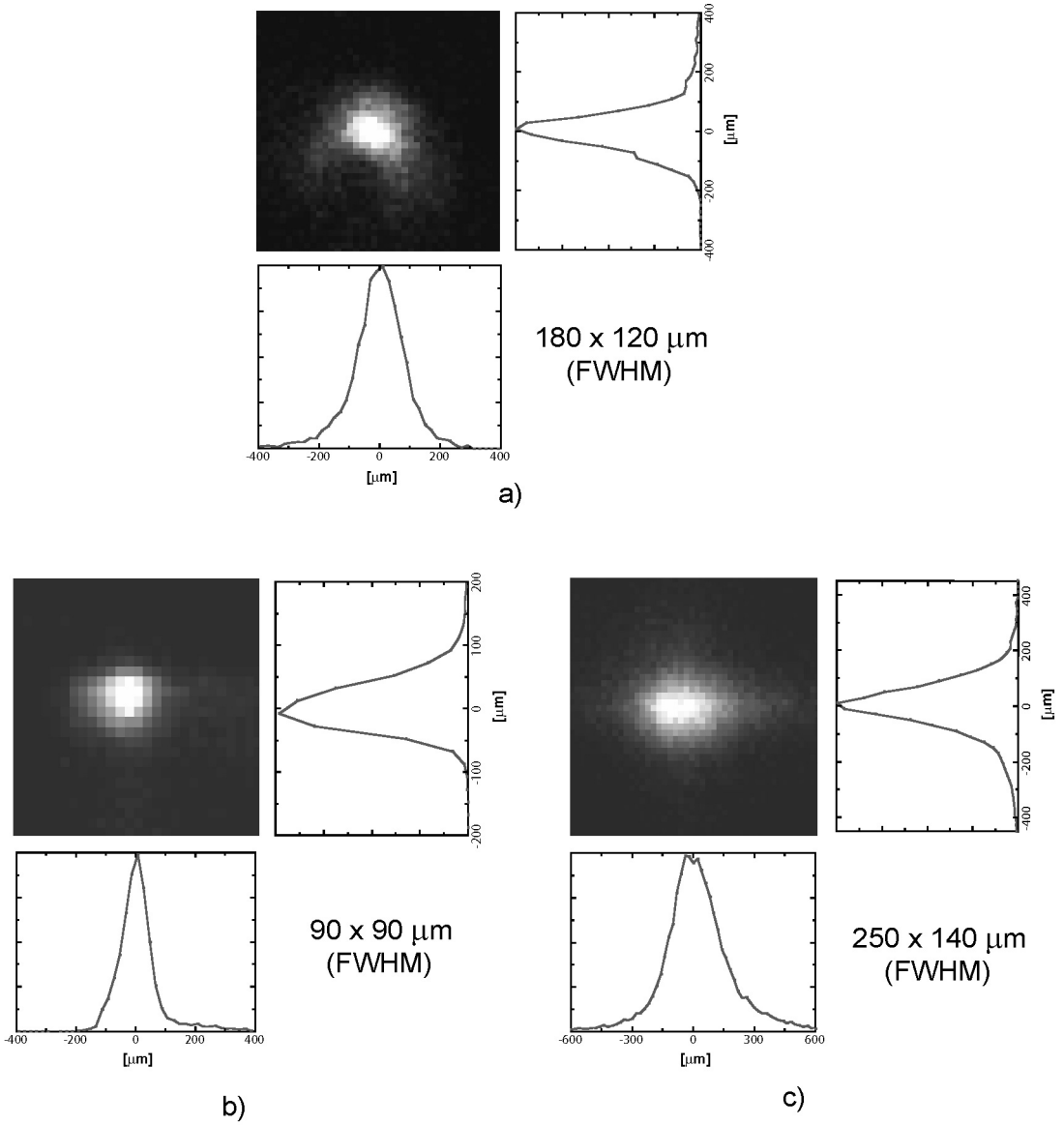

Figure 3.8. Images and cross-sections of the optics foci: a) SBM optic; b) Montel optic with a magnification of M=2.1; c) Montel optic with a magnification of M=7.3.

The third is a spot located at the intersection of the two lines. This spot is formed by sequential reflection of X-ray radiation by both multilayers and represents the radiation of interest. Note that for the M=7 Montel optic all three components overlap just after the exit of the optic and become separated only when they get closer to the image plane (figure 3.7.c). Figure 3.8 depicts magnified images of the optics foci shown at the lower panel in figure 3.7. The measured focal spot size for the Montel E19 optic with magnification M=7 reveals that the X-ray source size is about 20-30 μm. This value is consistent with the value for the X-ray source size obtained in experiments described in section 2.2 where the measurements were performed using a pinhole camera. The sizes of the focal spots for the SBM optic with a magnification of 3.2 and the Montel optic with a magnification of 2.1 are larger than the product of the source size and the magnification. Consequently, the measured distributions of the X-rays focused by these two optics are determined to a marked degree by the aberrations of the optics.

Diffraction test with the Montel E19 optic

An X-ray optic used in a time-resolved X-ray diffraction experiment is intended for the collection and focusing of the X-ray radiation on the sample under investigation. The X-ray radiation should be focused in such a way that the diffraction signal from the sample is maximal. As a monocrystalline sample diffracts only the X-rays in the narrow angular range determined by the width of its rocking curve it is important to have as many X-rays as possible within this angular range. The number of X-ray photons in a certain angular range is described by the ‘angular flux density’. As one can see in table 3.1 the Montel E19 optic has the largest angular flux density and in this respect it is the most attractive optic for diffraction experiments.

In order to estimate the performance of the optic in diffraction experiments it was compared with the toroidal mirror (No. 1) described in section 3.1 in the particular case of the (444) reflection of a 150 nm thick mono-crystalline Germanium sample.

The principle scheme of the performed diffraction experiment is shown in figure 3.9. The sample was placed in the focal spot of the Montel E19 optic.

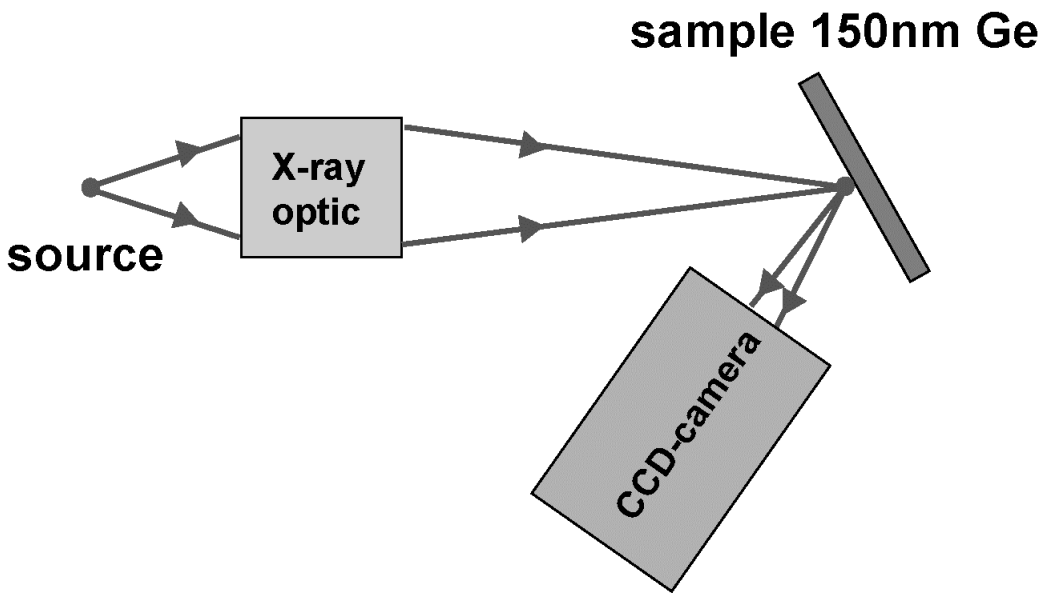

Figure 3.9. Principle scheme of the diffraction experiment with the Montel E19 optic.

The measured integrated intensity of the Ge (444) reflection was ~25±5 times larger than that of the Ge (444) reflection when X-rays were focused by the toroidal mirror. The accuracy of this ratio was determined by the accuracy with which the diffracted signal was measured when X-rays were focused by the toroidal mirror. In this case the signal detected by the CCD camera (see figure 3.9) was less than one photon per pulse. The X-ray flux of the X-ray source was kept the same during both diffraction experiments.

The corresponding measured fluxes of the focused X-rays were 17000 and 6000 ph/pulse for the Montel E19 optic and for the toroidal mirror No.1, respectively.

When the X-rays are focused by the Montel optic the sample can diffract only the $K_{\alpha 1}$ radiation (the Bragg condition can not be fulfilled for the $K_{\alpha 2}$ radiation for the cone of radiation incident on the sample). Taking this into account, one can estimate the relative number of X-ray photons diffracted by the sample for different X-ray optics using the values of the angular flux densities of the incident radiation. For the optics used the ratio of theoretically expected diffraction signals is equal to 20. Thus, the measured ratio of the signals diffracted from the sample is in line with what is theoretically expected.

3.3. Capillary optic

This section presents the characterization of a capillary optic that is designed for the focusing of femtosecond X-ray pulses.

The main component part of a mono-capillary optic is a thin lead glass tube of which the inner surface has an ellipsoidal shape (figure 3.10).

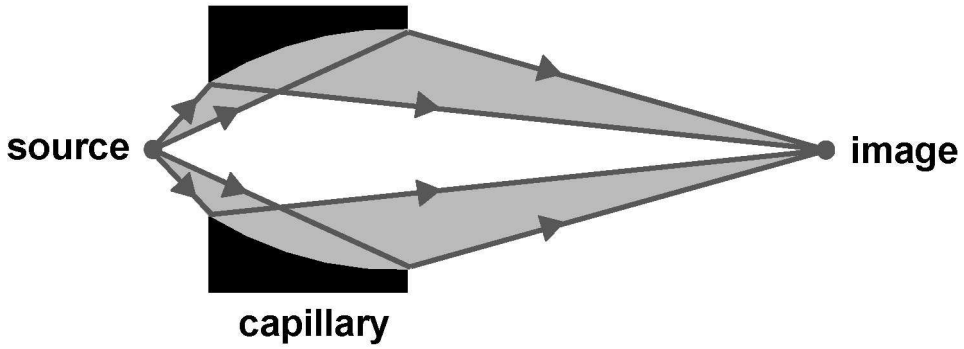

Figure 3.10. Principle scheme of the ellipsoidal capillary.

The principle of operation is based on the effect of total internal reflection of X-rays at grazing incidence. The angle of total reflection for the inner surface of the capillary is approximately 0.3 deg and it only slightly changes with a change of the X-ray wavelength. This means that a broad spectrum of X-rays can be reflected by the capillary and that the focused radiation is not monochromatic. Geometrical properties of the capillary optic tested here are listed in table 3.3.

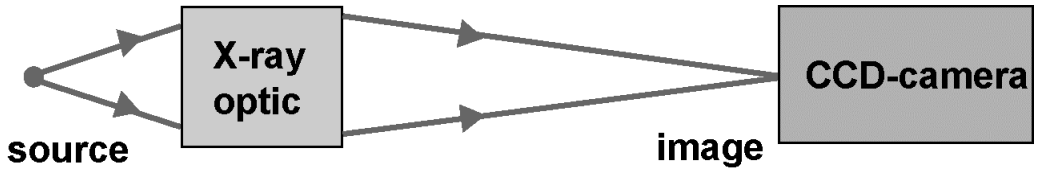

Figure 3.11. Principle scheme of the measurement of X-ray intensity distribution in the focal spot of the capillary optic.

Working distances	
Sample-optic [mm]	50
Optic-sample [mm]	476
Length of the optic [mm]	150
Capture angle [sr]	$4x10^{-4}$
Horizontal [deg]	1.3
Vertical [deg]	1.3
Horizontal convergence [deg]	0.18
Magnification	7
Wavelength [nm]	0.154

Table 3.3. Main geometrical properties of the capillary optic.

The measured intensity distribution of the focused X-rays is presented in figure 3.12. The two additional graphs in figure 3.12 reveal the horizontal and vertical cross-sections of the X-ray radiation intensity distribution in the focal plane.

The measured size (FWHM) of the focal spot is 190 and 160 μm in a horizontal and vertical direction, respectively. This size is small enough to carry out experiments and it is mainly limited by the size of the X-ray source (FWHM ~25 μm). The FWHM of the source size multiplied by the magnification of the optic (M=7) gives approximately the measured size of the focal spot. It is important to notice that there is also radiation which passes directly through the optic without reflection. It forms a weak background under the spot of the focused X-rays which is not seen in figure 3.12.

To check the performance of the capillary optic the diffraction signal of a Silicon monocrystalline sample placed in the focus of the capillary was measured. It was found that the integrated intensity of the Si (111) Bragg-reflection was approximately 3.5 times larger than the one when X-rays were focused by the toroidal mirror (No. 1) described in section 3.1.

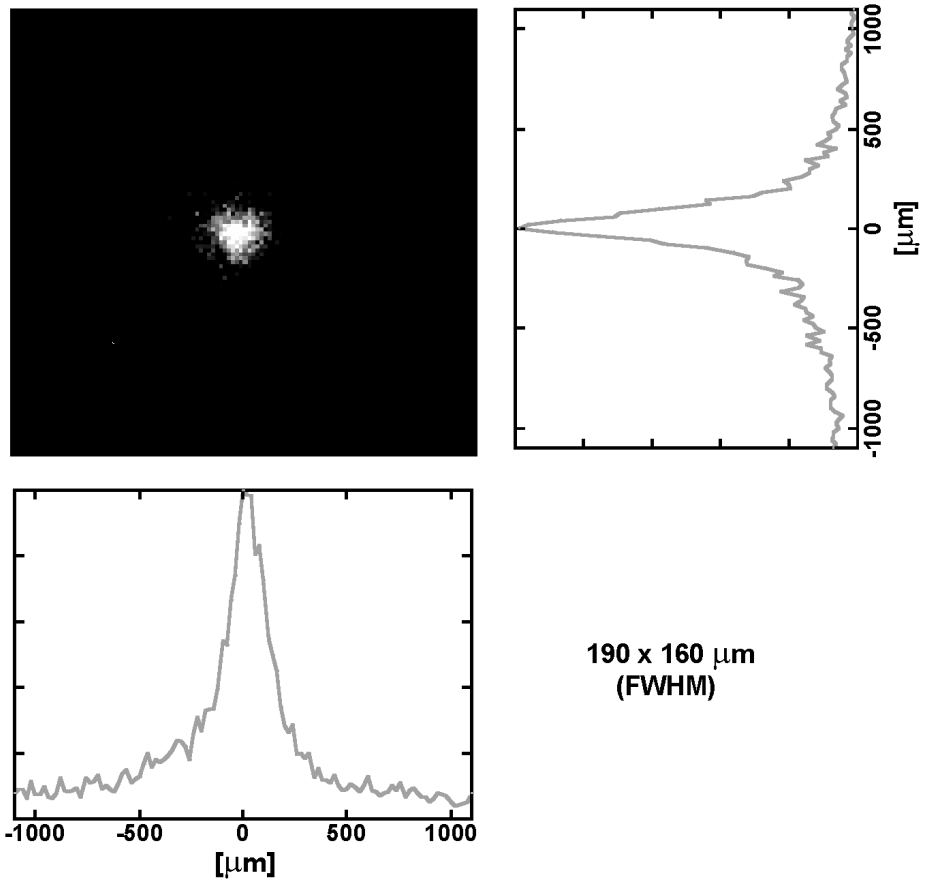

Figure 3.12. Intensity distribution of the X-ray radiation focused by the capillary optic.

The X-ray flux of the source was kept the same for both diffraction experiments. The measured angular flux density of the X-rays focused by the capillary optic is ~5 times larger than that of the toroidal mirror. As the rocking curve of the Si (111) reflection is much narrower than the convergence angle of the focused X-rays the magnitude of the diffracted signal should be proportional to the angular flux density. However, with the capillary optic less X-rays are diffracted from the sample than expected from the ratio of angular flux densities. This is most probably due to the fact that the radiation focused by the capillary is not monochromatic as it is in the case of the toroidal mirror but has a broad spectrum (much larger than the width of the Cu-K_α radiation) and only some of the wavelength components satisfying the Bragg condition can be diffracted by the sample.

Possibility of the time-resolved Debye-Scherrer diffraction

A small convergence angle of the X-rays focused by the capillary optic makes it possible to observe not only a single Bragg-reflection from single-crystalline samples but also to use other diffraction schemes.

Here a Debye-Scherrer (powder) diffraction experiment using femtosecond X-ray radiation is presented.

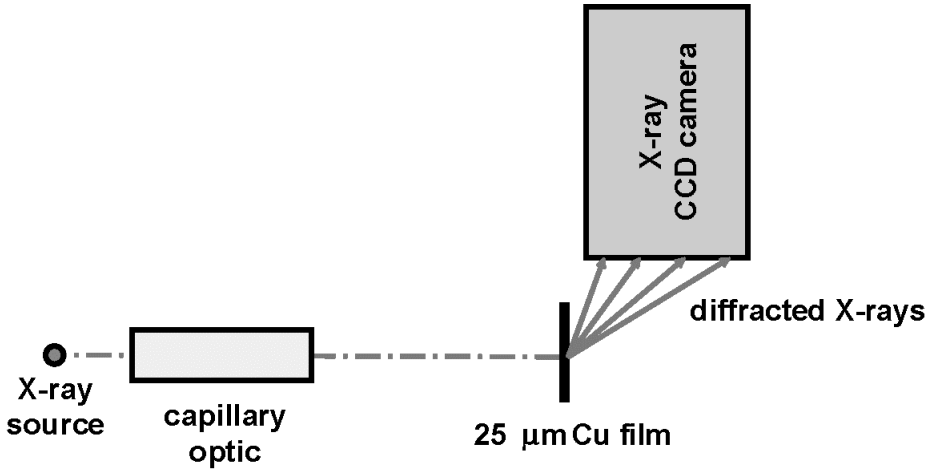

a)

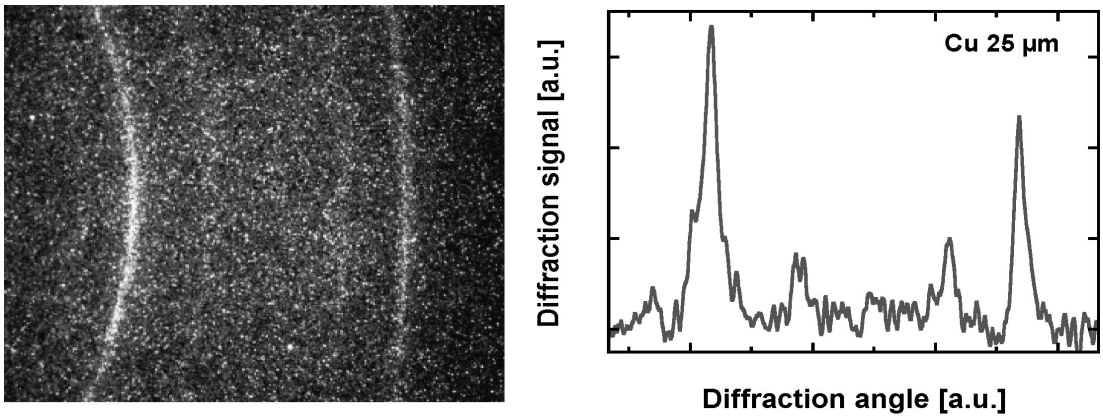

b) c)

Figure 3.13. Debye-Scherrer (powder) diffraction experiment: a) the principle scheme of the experimental setup for Debye-Scherrer powder diffraction; b) diffraction pattern of a 25 µm thick polycrystalline copper foil, using X-rays focused by the capillary; c) radial cross-section of the diffraction pattern.

The principle scheme of the experimental setup is shown in figure 3.13.a. A 25 μm thick polycrystalline copper foil was placed after the capillary. The diffracted signal was measured using the “Photonic Science” CCD-camera where the incoming X-rays first generate optical photons in a phosphor scintillator and the generated photons are then detected by a CCD-chip.

Figure 3.13.b presents a diffraction pattern obtained with 5 min exposure time in which one can see four different diffraction orders detected simultaneously. They can be seen even more clearly in figure 3.13.c which is a radial cross-section of the CCD-image in figure 3.13.b.

The result of this experiment is of great importance for performing future time-resolved Debye-Scherrer measurements, where many diffraction orders can be observed simultaneously. Furthermore, as the Debye-Scherrer method does not require single-crystalline samples, it makes it possible to cover a much larger range of materials which can be used and studied by TRXD.

3.4. Comparison of optics

Depending on the experimental conditions different properties of the particular optic can be of importance: monochromaticity, angular flux density, focal spot size, magnification and the total angular range of the focused X-rays.

Monochromaticity (spectral range of the focused radiation)

The optics which have a narrow spectral range of the focused radiation are well suited for experiments requiring a high angular resolution. High angular resolution is necessary, for example, in experiments on acoustic phonons in crystalline samples where the acoustic phonons are detected by observing the changes of the Bragg-reflection profiles. The toroidal mirror is the most monochromatizing type of optic among the three types of optics investigated here. It is followed by the multilayer optic which typically focuses the whole radiation of the K_α line but suppresses the radiation of the K_β line of a laser-plasma based X-ray source. The capillary optic focuses the broadest spectral range of the X-ray source radiation.

Angular flux density

A large angular flux density is required if one is interested in the integral intensity of the diffracted signal from the sample. The width of the single-crystalline sample rocking curve is usually much narrower than the convergence angle of the focused X-ray beam and the increase of the angular flux density directly leads to an increase of the diffracted signal intensity. The integrated intensity of the diffracted signal can be of interest, for example, in experiments on non-thermal melting, on the transient Debye-Waller factor and on optical phonons. Among the optics tested here, the Montel optic with magnification M=7.3 and the capillary optic have the highest

angular flux densities (the high value of magnification of these optics leads to the collimating effect and consequently to the increase of the angular flux density).

Focal spot size

The focal spot size should be smaller than the size of the excitation beam so that one can measure the local response of a homogeneously excited region of the sample. Optics having a small focal spot size may be used if one needs to investigate nonreversible changes in samples having small dimensions, or if the energy of the excitation beam is not large enough to induce changes over a significant area at the sample under study. It was found that all the tested optics allow the radiation to be focused onto a spot with a diameter of about 100-200 μm. The toroidal mirrors and the Montel optic with a magnification of M=2.1 have the smallest focal spot sizes of about 100 μm.

Magnification

Varying the magnification of the optic changes both the size of the focal spot and the convergence/divergence of the focused X-rays.
For applications where it is important for the size of the probe beam to be small it is recommended to use optics with smaller magnification.
The use of optics with a large magnification increases the magnitude of the diffracted signal from single-crystalline samples because of the increased angular flux density.
A large magnification has also a strong collimating effect which allows the use of other diffraction schemes instead of the single-reflection Bragg-diffraction. One of them is Debye-Scherrer diffraction from poly-crystalline materials. An example of such an experiment using the capillary optic is described in section 3.3.
Among the optics tested here the Montel E19 optic and the capillary optic have the largest magnifications equal to M=7.3 and M=7, respectively. The toroidal mirrors have the smallest magnification equal to one.

Total angular range

A large value of the total angular range is needed if large shifts of the rocking curves are expected. Toroidal crystals have the largest total angular range among the tested optics (1.4 deg) due to the low magnification (M=1). This, in combination with the high angular resolution, makes these optics most suitable for experiments where large angular shifts and changes of the rocking curves (for example induced by a transient strain) are of interest.

4. Time-resolved experiments

4.1. Diffraction of convergent and divergent X-ray beams in X-ray pump / optical probe experiments

As described in chapter 2, in a typical pump/probe experiment there are two beams which are focused on the sample under investigation. The first beam (called the pump beam) induces the changes in the sample. The second (called the probe beam) detects these changes. Focusing of the pump beam is required to achieve the necessary level of excitation and to avoid damage to large areas at the sample surface in irreversible experiments. At the sample surface the size of the probe beam should be significantly smaller than the size of the pump beam to insure that the measured signals represent only the local response of a homogeneously excited region.
This section discusses a particular dramatic effect which occurs when this condition is not fulfilled. In this particular case large and initially unexpected changes in the measured signal were observed when a divergent or convergent X-ray beam was diffracted from an inhomogeneously strained surface. A simple model has been developed to describe this phenomenon.

Adjusting the overlap between the optical pump and the X-ray probe beams

The typical sizes (FWHM) of the focused optical and X-ray beams used in the performed experiments were 400 and 100 μm, respectively (see figure 4.1). As X-ray radiation is not seen, it is not possible to adjust the spatial overlap of the beams just by optical observation of their relative positions at the sample surface.
Adjustment of the overlap between the two beams in this case is carried out by observing the magnitude of changes in the diffracted signal caused by the pump beam.
Maximal changes in the diffracted signal should be observed when the X-ray beam probes the area on the surface maximally excited by the optical beam, i. e. the area

excited by the part of the optical beam, having maximum intensity. For a bell-like-profile of the excitation beam it is the area excited by the beam centre.

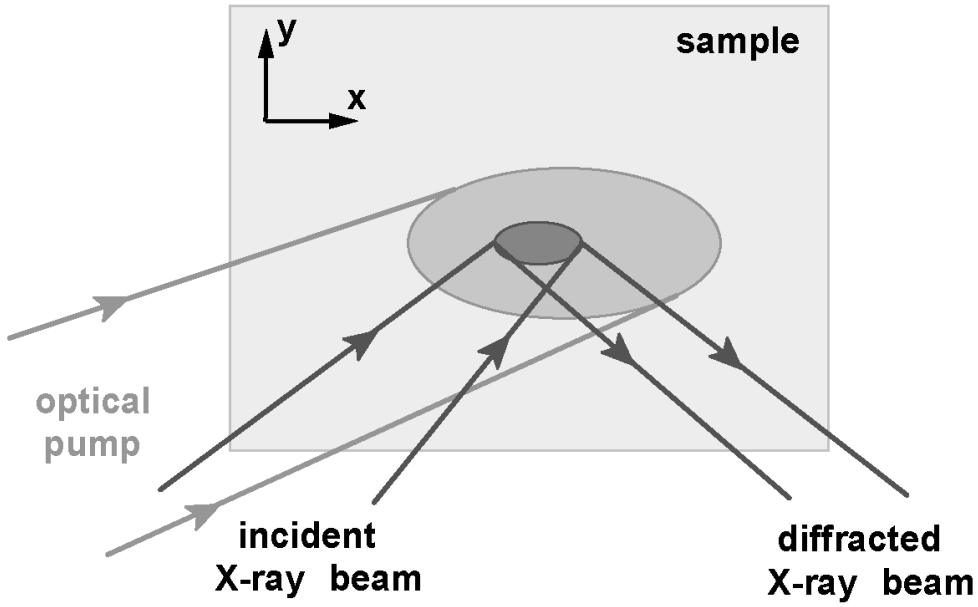

Figure 4.1. Geometry of the pump/probe experiment.

For typical excitation conditions below the melting threshold two types of changes of the diffracted signal can be observed: (i) changes of the angular integrated diffraction signal (integrated reflectivity), and (ii) changes of the angular diffraction profile (rocking curve).

Experiment

A thin monocrystalline 150 nm Germanium film on a Silicon substrate was used as a sample. The sample was excited by 120 fs, 800 nm laser pulses with peak fluences of about 30 mJ/cm^2. Ti-K_α X-ray pulses focused on the sample by the toroidal mirror No.2 (as described in section 3.1) were used for probing.

Having found the (apparent) overlap between the beams corresponding to the maximum change of the X-ray beam integrated reflectivity, the latter was measured as a function of the time delay between the pump and probe pulses. The results of such measurements for the (400), (311) and (111) Bragg-reflections are depicted in figure 4.2.

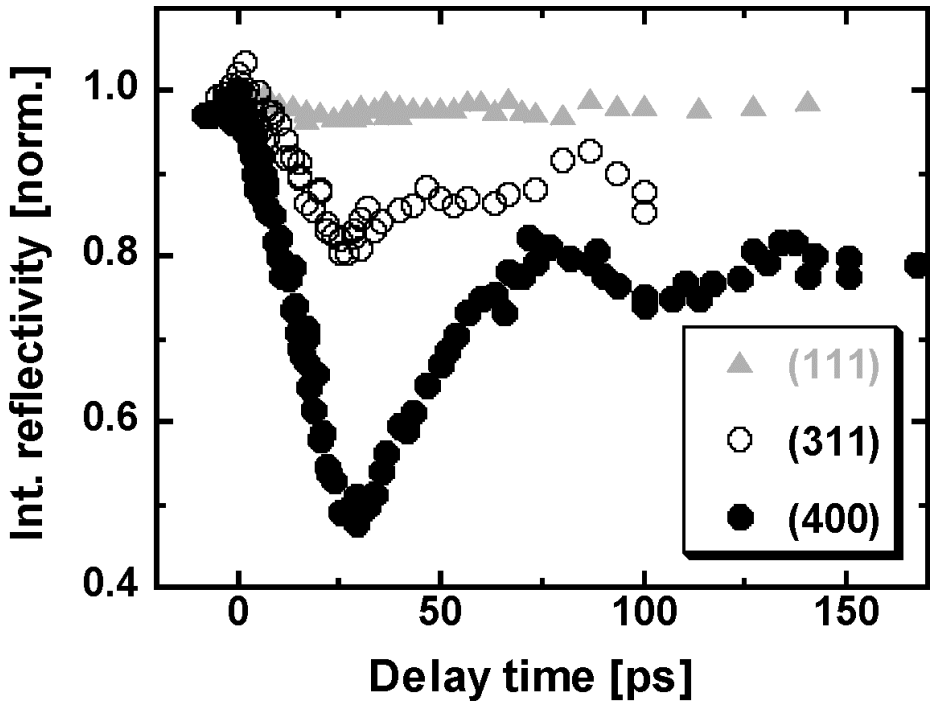

Figure 4.2. Angular integrated diffraction signal as a function of time delay between the pump and probe pulses for the (400), (311) and (111) Brag-reflections.

The measured data have two peculiarities. Firstly, the observed changes (up to 50 %) are significantly larger than the changes initially expected because of lattice heating by the excitation pulse. For the excitation fluence used in the experiment one expects decreases of the diffraction signal by only 1.1, 3.8 and 5.5 % for the (111), (311) and (400) reflections, respectively (see also chapter 4.2). Secondly, periodic changes of the magnitude of the diffraction signal were observed. The time to reach the first minimum is approximately 26 ps, which corresponds exactly to the time a longitudinal acoustic wave needs to travel through a 150 nm thick Germanium layer. The second feature is especially remarkable, because it is expected that the strain induced by acoustic waves leads to changes of the angular diffraction profile but not to changes of the integrated reflectivity. Therefore, the angular behaviour was also analysed. In particular, observations of the centre of gravity angular shift of the diffracted X-rays for different relative positions of the pump and probe beams on the sample surface revealed that the position of the beams corresponding to the maximum angular shift of the Bragg-reflection does not coincide with the position

corresponding to the minimum of the magnitude of the diffracted signal. Moreover, such a relative position of the beams was found where the integrated reflectivity becomes larger (!) than without excitation. The maximum and the minimum of the integrated reflectivity were located symmetrically relative to the position corresponding to the maximum angular shift of the Bragg-reflection. Figure 4.3 presents the dependence of the integrated reflectivity on the relative position of the pump and probe beams on the sample surface 26 ps after the optical excitation. The data shown in figure 4.3 correspond to a scan along the X-axis in figure 4.1, i.e. the pump beam was shifted in the X-direction.

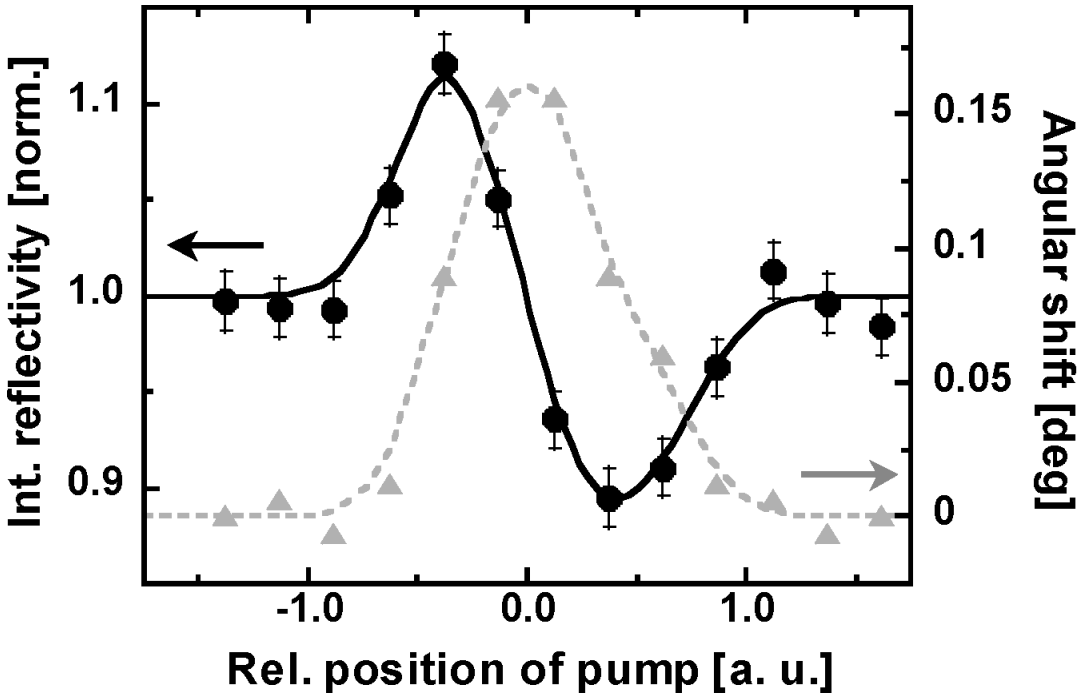

Figure 4.3. Dependence of integrated reflectivity (filled circles) and angular shift (grey triangles) of the diffracted signal on the relative position of the pump and probe beams on the sample surface along the X-axis. Integrated reflectivity dependence clearly shows a maximum and a minimum within the area excited by the optical beam. The curves represent a guide to the eye.

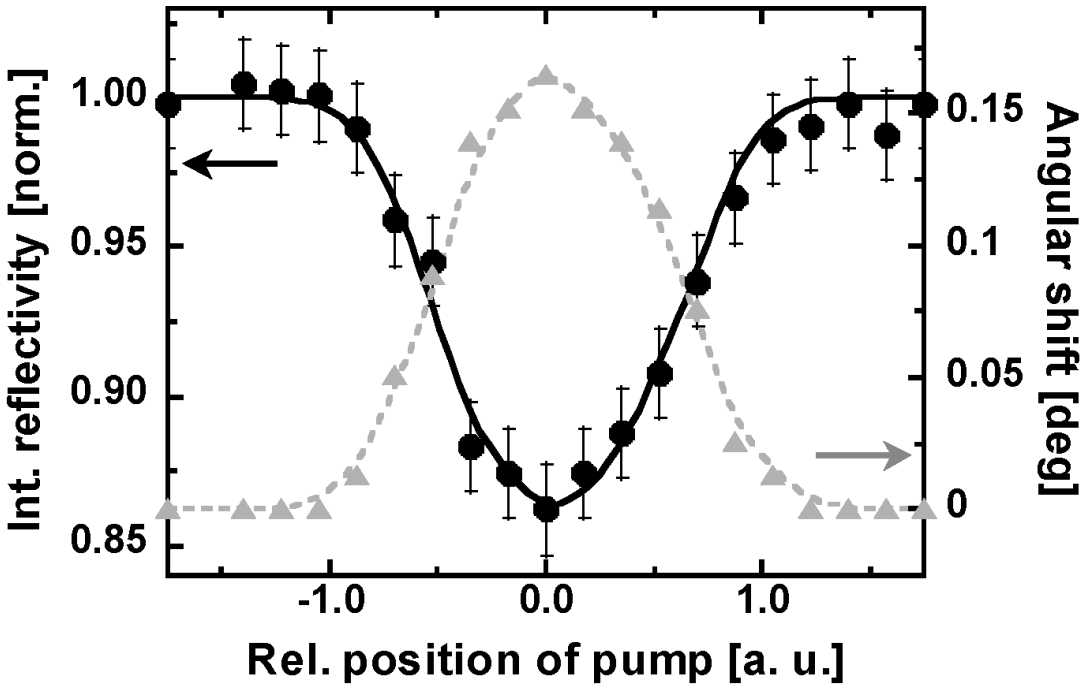

Figure 4.4. Dependence of integrated reflectivity and angular shift of the diffracted signal on the relative position of the pump and probe beams on the sample surface along the Y-axis. The angular shift and integrated reflectivity are symmetrical one relative to another.

However, for scans along the Y-axis the integrated reflectivity changes and the angular shift show a similar behaviour. So, either only a single minimum or only a single maximum was observed in the scan along Y depending on the relative location of the beams along the X-axis. Figure 4.4 depicts a vertical scan for the horizontal positions of the beams corresponding to the minimum of the integrated reflectivity in the horizontal scan.

To understand these results, one should take into account that there is one more free parameter in the experiment: The location of the sample surface relative to the X-ray toroidal mirror focal plane. Simple geometrical measurements allow the position of the focal plane to be determined with an accuracy of about 1-2 mm. In order to check the influence of the location of the sample surface relative to the focal plane, the sample was shifted downstream by ~4 mm in the direction perpendicular to the XY-plane in figure 4.1. After this shift, measurements reveal that the maximum and the

minimum in the horizontal scan ‘exchanged’ their positions. The horizontal scan for the described situation is depicted in figure 4.5.

Between these two positions a sample position was found where the maxima and minima in the horizontal scan disappeared (or they became so small, that they could no longer be resolved within the accuracy of the experiment).

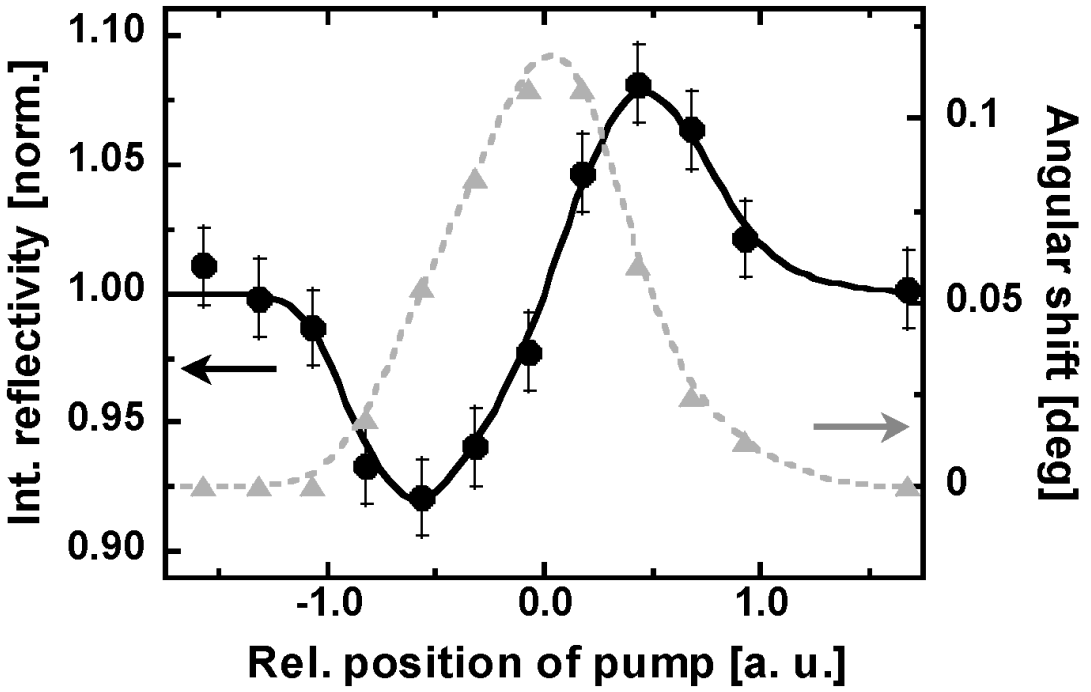

Figure 4.5. Dependence of integrated reflectivity and angular shift of the diffracted signal on the relative position of pump and probe beams on the sample surface along the X-axis. Sample position is behind the toroidal mirror focal plane.

A horizontal scan corresponding to this position is shown in figure 4.6. The oscillation behaviour presented in figure 4.2 also disappeared under these conditions.

The following paragraphs present a model which explains the changes of the magnitude of the diffracted signal when a convergent or divergent X-ray beam diffracts from an optically excited sample.

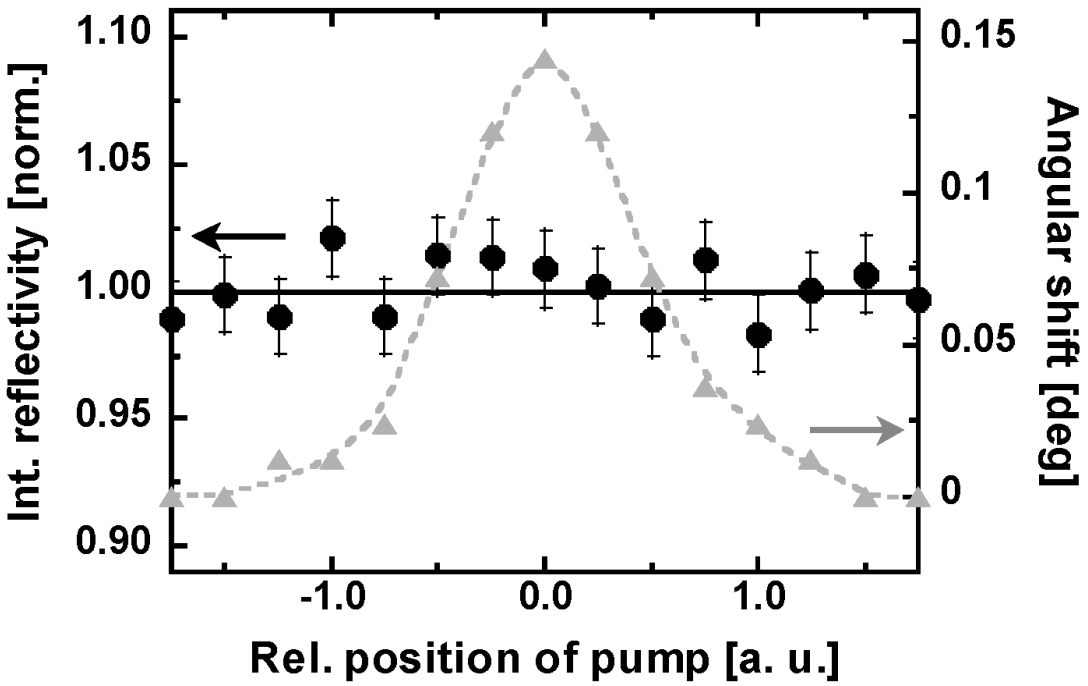

Figure 4.6. Dependence of integrated reflectivity and angular shift of the diffracted signal on the relative position of the pump and probe beams on the sample surface along the X-axis. The sample is in the toroidal mirror focal plane.

Consider diffraction of a convergent X-ray beam incident on an inhomogeneously strained sample (figure 4.7). In this case different parts of the incident X-ray radiation 'see' different lattice constants of the inhomogeneously excited sample in the areas where the increase and decrease were observed, i. e. there is a gradient of the lattice constant along the X-coordinate or, in accordance with the Bragg law, there is a gradient of the angle, satisfying the Bragg condition:

$$\Theta_{\mathrm{Br}}(x) = \Theta_{\mathrm{Br}}(x_0) + \left.\frac{d\Theta_{\mathrm{Br}}}{dx}\right|_{x_0} (x - x_0) \qquad (1)$$

The glancing angle of the X-ray beam Θ also depends on the X-coordinate, suppose:

$$\Theta(x) = \Theta(x_0) + \left.\frac{d\Theta}{dx}\right|_{x_0} (x - x_0) \qquad (2)$$

Assume that in the centre of the incident beam ($x=x_0$) the angle of incidence is equal to the Bragg-angle. Then for each $x \neq x_0$ there is a difference between the glancing angle $\theta(x)$ and the Bragg-angle $\theta_{Br}(x)$. The larger the difference $|x-x_0|$, the larger the difference between these two angles.

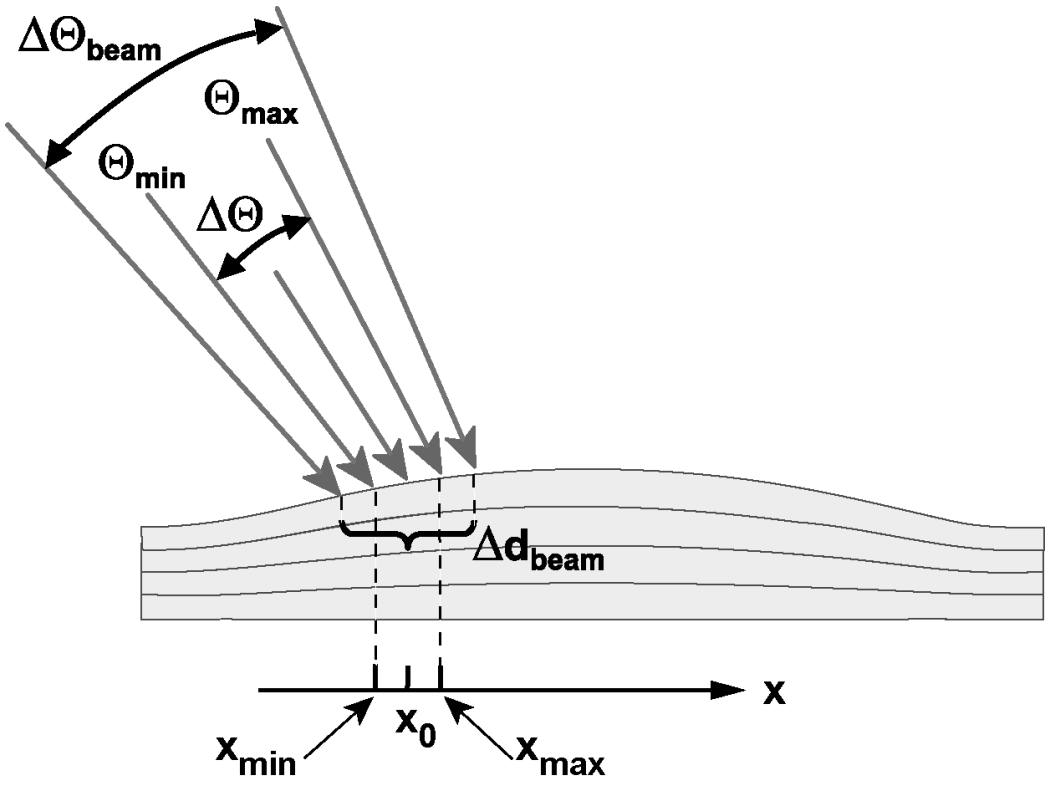

Figure 4.7. Profile of a sample heated by an optical beam. x_0 is the position of the centre of incident beam, x_{max} and x_{min} are positions where the difference between the angle of incidence and the Bragg-angle is equal to the half width at half maximum of the sample rocking curve $\Delta\theta_{RC}$.

In this case the effective width (FWHM) of the diffracted beam $\Delta\theta = \theta(x_{max}) - \theta(x_{min})$ is determined by the condition, that the difference between the local angle of incidence and the local Bragg-angle is equal to the half width at half maximum of the sample rocking curve $\Delta\theta_{RC}$. Thus, the minimum angle of incidence of the diffracted X-rays can be written as:

$$\Theta(x_{min}) = \Theta_{Br}(x_{min}) - \Delta\Theta_{RC}/2 \tag{3}$$

And the maximum angle as:

$$\Theta(x_{max}) = \Theta_{Br}(x_{max}) + \Delta\Theta_{RC}/2 \tag{4}$$

These formulas are valid when the difference $|x_{max}-x_{min}|$ is smaller than the size of the beam Δd_{beam}:

$$|x_{max} - x_{min}| < \Delta d_{beam} \tag{5}$$

The opposite case will be considered later.
The integrated reflectivity of the diffracted signal is determined as:

$$I = k\frac{\Theta(x_{max}) - \Theta(x_{min})}{\Delta\Theta_{beam}} = k\frac{x_{max} - x_{min}}{\Delta d_{beam}} \tag{6}$$

The coefficient k is determined by the rocking curve of the sample under investigation. In formula (6) it is taken into account, that:

$$\frac{\Theta(x_{max}) - \Theta(x_{min})}{x_{max} - x_{min}} = \frac{\Delta\Theta_{Beam}}{\Delta d_{beam}} \tag{7}$$

From (3) and (4) one derives that the fraction of the X-rays within the angular range:

$$\Theta(x_{max}) - \Theta(x_{max}) = \Theta_{Br}(x_{max}) - \Theta_{Br}(x_{min}) + \Delta\Theta_{RC} = \left.\frac{d\Theta_{Br}}{dx}\right|_{x_0}(x_{max} - x_{min}) + \Delta\Theta_{RC} \tag{8}$$

undergo Bragg-diffraction.

Substituting $\theta(x)$ and $\theta_{Br}(x)$ from equations (1) and (2) in (8) and expressing $\Delta\theta_{RC}$ one determines:

$$\Delta\Theta_{RC} = \left(\frac{\Delta\Theta_{Beam}}{\Delta d_{beam}} - \left. \frac{d\Theta_{Br}}{dx} \right|_{x_0} \right) (x_{max} - x_{min}) \tag{9}$$

Substituting $(x_{max}-x_{min})$ in (6) from (9) one obtains:

$$I = k \frac{\Delta\Theta_{RC} / \Delta d_{beam}}{\frac{\Delta\Theta_{Beam}}{\Delta d_{beam}} - \left. \frac{d\Theta_{Br}}{dx} \right|_{x_0}} \tag{10}$$

Formula (10) describes the diffracted beam integrated reflectivity as a function of the gradient $d\theta_{Br}/dx$.

In the particular case where there is no change of the lattice constant over the X-coordinate $(d\theta_{Br}/dx)=0$:

$$I \equiv I_{homogeneous} = k \frac{\Delta\Theta_{RC} / \Delta d_{beam}}{\frac{\Delta\Theta_{Beam}}{\Delta d_{beam}} - 0} = k \, \Delta\Theta_{RC} / \Delta\Theta_{beam} \tag{11}$$

This means that the diffracted signal intensity is determined by the ratio of the rocking curve width to the incident beam angular width.

If $(d\theta_{Br}/dx)=const_1$ $(const_1>0)$ then

$$I \equiv I_{const1} = k \frac{\Delta\Theta_{RC} / \Delta d_{beam}}{\frac{\Delta\Theta_{Beam}}{\Delta d_{beam}} - const_1} > I_{homogeneous} \tag{11.a}$$

In this case an increase of the diffracted intensity in the X-scan is observed.

If $(d\theta_{Br}/dx) = - const_2$ $(const_2>0)$ then

$$I \equiv I_{const\,2} = k\frac{\Delta\Theta_{RC}/\Delta d_{beam}}{\frac{\Delta\Theta_{Beam}}{\Delta d_{beam}} + const_2} < I_{homogeneous} \qquad (11.b)$$

Then a decrease of the diffracted intensity in the horizontal scan is observed.
One can see in figure 4.2 that the maxima and minima in integrated reflectivity really correspond to the areas of the sample having maximal gradient of the lattice constant. Similar considerations for a divergent beam reveal that for the gradient of the lattice constant corresponding to the maximum of the convergent beam integrated reflectivity, a minimum should be observed and vice versa. This fits the experimental results depicted in figure 4.5 and in figure 4.3.

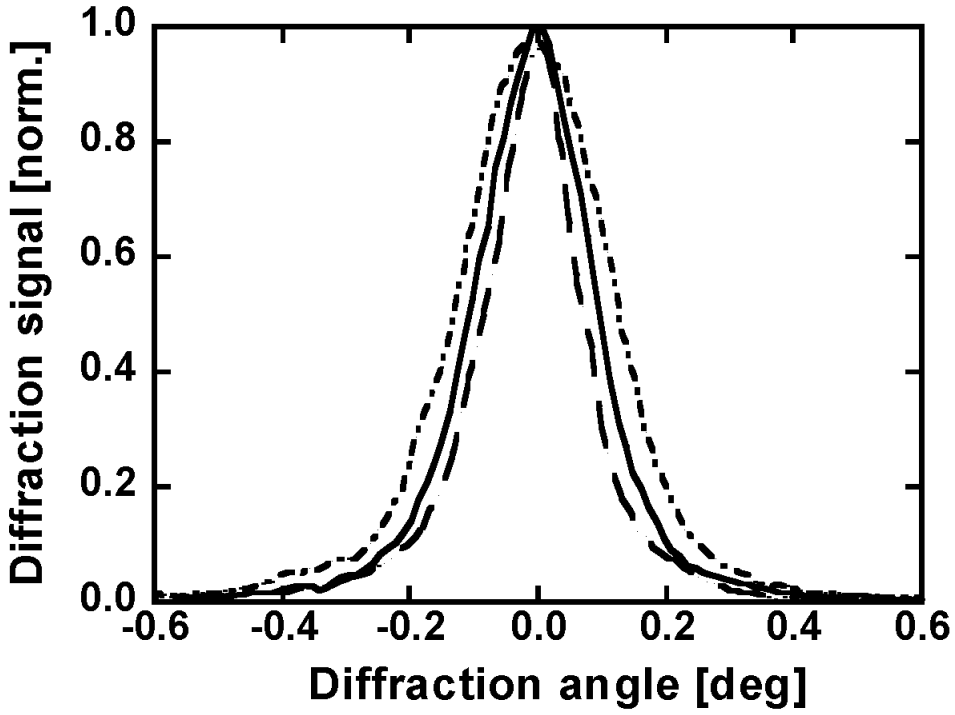

Figure 4.8. Rocking curves for different relative positions of the pump and probe pulses of the X-scan. The solid line represents the rocking curve without excitation. The dashed-dotted and the dashed lines show the rocking curves corresponding to the maximum and minimum in the X-scan in figure 4.3, respectively.

An interesting point to be noted here is that the change of the integrated reflectivity calculated by formulas (11.a) and (11.b) is due to the change of the angular range of the incident X-rays which undergo Bragg-diffraction. So, according to formula (8) a positive value of the derivative $(d\theta_{Br}/dx) > 0$ increases the angular acceptance range and a negative value of $(d\theta_{Br}/dx) < 0$ decreases the ang ular acceptance range relative to that of the unperturbed sample $\Delta\theta_{RC}$.

This model prediction has been verified in the experiment, as can be seen in figure 4.8. The rocking curve corresponding to the maximum in the X-scan in figure 4.3 is broader than the rocking curve of the unperturbed sample and the rocking curve corresponding to the minimum in the X-scan is narrower than that of the unperturbed sample.

By increasing the excitation inhomogeneity $(d\theta_{Br}/dx)$ the difference $(x_{max}-x_{min})$ can become larger than Δd_{beam} $(|x_{max}-x_{min}|>\Delta d_{beam})$. This means that the angular range of X-rays which can be accepted and which contributes to the X-ray diffraction signal is larger than the angular range of the X-rays incident on the sample. The diffraction signal grows and reaches its maximum I=k, when $d\theta_{Br}/dx = \Delta\theta_{Beam}/\Delta d_{Beam}$. Physically it means that the angle of incidence is equal to the Bragg-angle for all $x \in \Delta d_{beam}$. A further increase of the excitation inhomogeneity leads to an increase of the difference between the Bragg-angle and the incidence angle, and the integrated reflectivity of the diffracted signal decreases.

In conclusion, significant and initially unexpected changes of the diffracted signal from a thin Germanium film after femtosecond optical excitation were observed. A model was developed which explains these changes. The model takes into account the lateral spatial inhomogeneity of the lattice strain as well as the divergence (convergence) of the X-ray probe beam. In order to avoid misinterpretation of the experimental data, the described effects need to be considered and eliminated in any time-resolved laser pump/X-ray probe diffraction experiment in which X-ray beams are used for probing the changes caused in the sample by an excitation beam having finite dimensions. On the other hand the described effect can also be used for probing the transient lattice strain in laser-excited crystals.

4.2. Direct observation of lattice heating in Germanium after fs-optical excitation

The first response of a semiconductor upon optical excitation is a transfer of electrons from the valence to the conduction band [58]. This is valid under the assumption that the photon energy $\hbar\omega$ is larger than the band gap E_g. In figure 4.9 the transfer of an electron is shown schematically with the vertical arrow directed from the valence band to the conduction band.

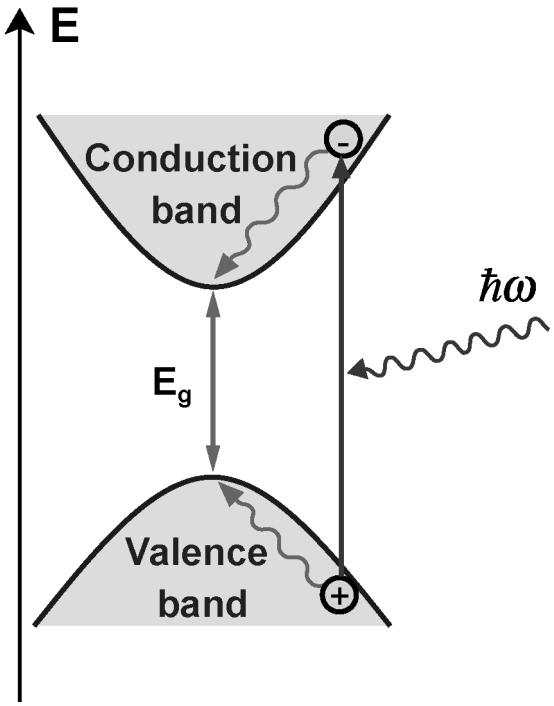

Figure 4.9. Primary electron excitation and relaxation in semiconductors.

The carriers produced in this way, i. e. the electrons in the conduction and the holes (vacancies) in the valence band, possess an excess of energy determined by the difference ($\hbar\omega$-E_g). Carrier-carrier interaction leads to a rapid equilibration within the electronic system within typically 1…10 fs (depending on the excitation conditions [59]). The carriers can thus be described by a temperature $T_{e\text{-}h}$ which is initially much higher than the temperature of the lattice T_L, because within this very short time no energy can be transferred to the lattice.

Energy relaxation of the excited carriers occurs via carrier-phonon scattering. As a rule, carrier-phonon scattering occurs during the first few hundred femtoseconds after excitation [58]. The energy transferred from an electron to the lattice during one act of electron-phonon scattering is much smaller than the total excess energy of the electron. Therefore, an electron needs many collisions to transfer its energy to the lattice. In this case we talk about the energy relaxation time τ_R, which is defined as the period during which the excess energy of the electrons is transferred to the lattice.
For periods smaller than the energy relaxation time ($t<\tau_R$) the matter is not in equilibrium and cannot be described by parameters of state as it is done in thermodynamics. Only for $t>\tau_R$ can one talk of a thermal regime, where the matter is in thermodynamical equilibrium and a thermodynamical approach can be applied, i.e. it makes sense to describe the matter with the equation of state (and with state variables like pressure and temperature).
Until recently, the relaxation of electrons was studied only by using optical pump/probe techniques, where the changes in the optical properties of the material were probed [60-71].
Measuring changes in the reflectivity or transmissivity as a function of the delay-time between pump and probe pulses maps out the changes in the electronic subsystem during electron-lattice energy relaxation. The excitation energy of the pump beam in such experiments is typically rather small to ensure weak perturbations of the electron distributions and consequently to cause a linear response of the system. Typical excitation fluences in experiments of this type are about 1 mJ/cm^2 or less. Under this condition, the measured changes in reflectivity and transmissivity can be directly related to the electron distribution [66].
A typical electron-lattice energy relaxation time determined by using optical pump-probe techniques was found to be in the order of about a picosecond.

For example, Del Fatti et al. [71] investigated transient optical reflectivity and transmissivity changes in Silver films using a femtosecond pump-probe technique and obtained an electron-phonon (e-ph) coupling time of 900 fs. Similar measurements by Groeneveld et al. [63] demonstrated an electron-phonon energy

relaxation time in Silver of 710 fs (for T = 300K) which decreases to 530 fs for T = 10K.

Experiments performed on Gold samples revealed relaxation times of 870 fs [63], 1 ps [66], and <1.5 ps [64].

A relaxation time of 1.6 ps in Nickel was reported by [65].

Huang et al. [69] presented time-resolved measurements on GaAs which demonstrated an electron-lattice energy relaxation time of about 7 ps.

Goldman et al. [70] used time-resolved photoelectron spectroscopy to directly observe the energy relaxation time of optically excited electrons in Silicon. An electron-phonon thermalization time of ~ 1 ps was reported.

Pump-probe measurements made by Fujimoto et al. [68] indicate an electron-phonon energy relaxation time in tungsten of several hundred picoseconds.

Thus, the electron-lattice energy relaxation has been studied in a lot of materials by various authors. However, the optical techniques they used only allowed them to probe directly the changes in the electronic subsystem during the electron-lattice energy relaxation. The information on the changes in the lattice subsystem could be derived from these experiments only indirectly.

A direct observation of the excitation and relaxation of the lattice phonons can be achieved by means of time-resolved Raman-scattering measurements where the intensity of the anti-Stokes scattered light is proportional to the number of phonons generated upon optical excitation [72]. However, only the long wave lattice phonons near the centre of the Brillouin-zone can be probed by this technique.

Harb et al. [73] and Park et al. [74] demonstrated direct observation of the lattice heating during the relaxation of optically excited electrons using time-resolved

electron diffraction. Their measurements revealed that the lattice heating occurs in Silicon and Aluminium within 2.0 and 0.6 ps, respectively. To the author's best knowledge, except the Raman-measurements these are the only two experiments on a direct observation of the lattice heating upon femtosecond optical excitation.

Experiments described in this section demonstrate that TRXD can also be used for direct measurement of the lattice heating during the electron-to-lattice energy transfer upon femtosecond optical excitation. The performed experiments revealed that the electron-lattice relaxation time in Germanium is equal to 1.1 ps.

4.2.1. Debye-Waller factor

This subsection discusses the changes of the diffracted signal caused by heating of the lattice during electron-lattice energy relaxation.

Debye [75] and Waller [76] showed that the increase of the crystal temperature leads to the decrease of the Bragg-reflection intensities, whereas the profile of the Bragg-reflection remains unchanged. This decrease is described by the Debye-Waller factor D(T):

$$D(T) = \frac{I_T}{I_O} = \exp(-\frac{1}{3} < \Delta\vec{r}^{\,2} > G^2) \tag{1}$$

I_T is the integrated intensity of the Bragg-reflection for T > 0 K and I_0 is the integrated intensity in the case of the "frozen" lattice, $< \Delta\vec{r}^{\,2} >$ is the mean square atomic displacement, G is a reciprocal lattice vector [77].

As is seen from formula (1), the Debye-Waller factor is due to the thermal vibrations of atoms near their equilibrium positions: D(T) decreases with the increase of the mean square atomic displacement $< \Delta\vec{r}^{\,2} >$, which in its turn increases with the increase of the lattice temperature.

The mean square displacement $< \Delta\vec{r}^{\,2} >$ can be calculated using the Debye theory of specific heat [78]. Formula (2) presents a result of this calculation taken from [79]:

$$D(T) = \exp(-M); \quad M = \frac{6h^2T}{mk_B\theta_D^2} \cdot \Phi(\frac{\theta_D}{T}) \cdot \frac{\sin^2(\theta_B)}{\lambda^2} \tag{2}$$

Here $\Phi(\Theta_D/T)$ is the Debye function which can be approximated by

$$\Phi(\frac{\theta_D}{T}) = \begin{cases} 1.642(T/\theta_D) + (\theta_D/4T), & (\theta_D/T) > 4.5 \\ 1 + (\theta_D/6T)^2 - (1/3600)(\theta_D/T)^4, & (\theta_D/T) < 4.5 \end{cases} \tag{3}$$

h is Plank's constant, T is the temperature of the material, m is the mass of the atom, λ is the wavelength of X-ray radiation, θ_B is the Bragg-angle, k_B is Boltzman's constant and θ_D is the Debye temperature of the material.

Taking into account the Bragg-law $2d_{hkl}\sin(\theta_B)=\lambda$ formula (2) can be written as:

$$D(T)=\exp(-M);\quad M=\frac{6h^2T}{mk_B\theta_D^2}\cdot\Phi\left(\frac{\theta_D}{T}\right)\cdot\frac{1}{(2d_{hkl})^2} \tag{4}$$

d_{hkl} is the distance between two neighboring Bragg-planes.

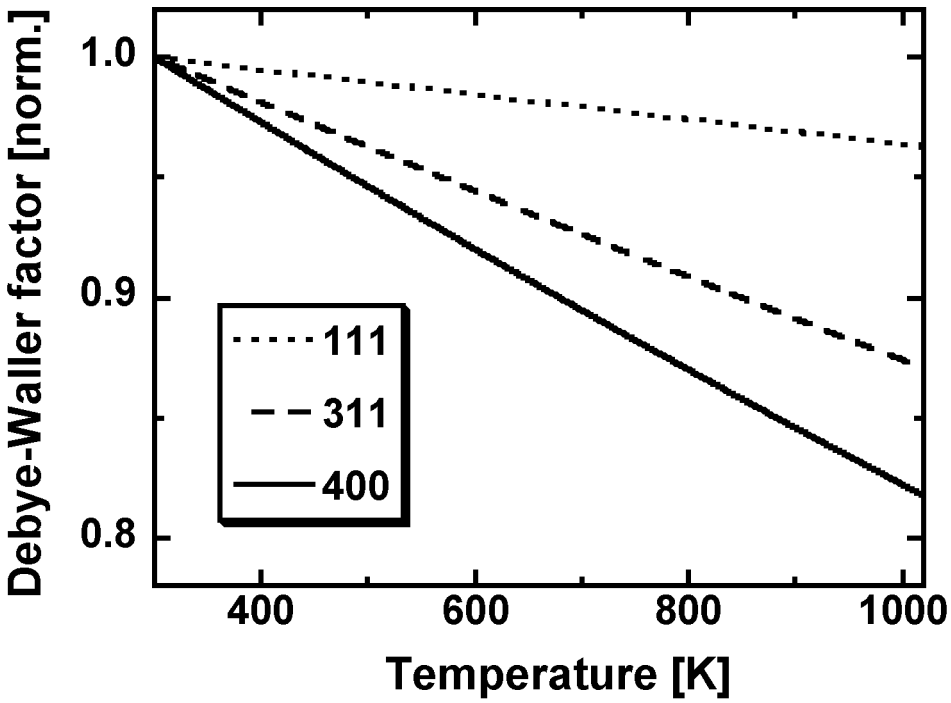

Figure 4.10. Calculated Debye-Waller factor.

As one can see from formula (4) the decrease of the Bragg-reflection intensity for a given material is large if the d_{hkl} is small. The temperature dependence of the Debye-Waller factor was calculated for the (111), (311) and (400) Bragg-reflections of Germanium for the Ti-K_α radiation ($\lambda_{Ti\text{-}K\alpha}$ = 0.275 nm). The result of the calculation is presented in figure 4.10. The data used for the calculation are listed in the table in

appendix A1. The values of the Debye-Waller factor presented in figure 4.10 are normalized to the values at room temperature.

Thus, the heating of the lattice during electron-phonon energy relaxation can be observed by measuring the changes in the integrated intensities of the Bragg reflections. Larger changes of the diffracted signal are expected for the reflections with higher Miller-indices.

4.2.2. Time-resolved measurements of the lattice heating in Germanium

This section presents the time-resolved X-ray diffraction measurements of the build-up of the incoherent lattice vibrations (lattice heating) in Germanium after femtosecond optical excitation.

The optical pump/X-ray probe technique described in section 2.3 was utilized to excite and probe incoherent lattice vibrations on a femtosecond time scale. A (111)-orientated monocrystalline 150-nm-thick Germanium film on a Silicon substrate was used as a sample [80, 81]. This sample was chosen for several reasons:

a) For the Ti-K_α X-ray radiation it was possible to observe three strong Bragg-reflections: Ge (111), (311) and (400).
b) The thickness of the Germanium film is comparable to the 200 nm linear absorption depth in Germanium at a wavelength of 800 nm [82]. This means that this sample can be effectively excited by the laser pulses produced by a Titanium-Sapphire laser system.
c) Fast diffusion of the excited electrons in Germanium leads to their fast redistribution through the whole film thickness within a few hundred femtoseconds [24, 83]. Thus, optical excitation of the sample should lead to practically homogeneous heating of the lattice through the whole thickness, whereas the heating of the substrate can be neglected as Silicon is practically transparent for λ=800 nm (linear absorption depth is about 10 μm [82]) and the hot electrons excited in the Germanium film cannot penetrate into the Silicon substrate because of the large potential barrier at the interface between Germanium and Silicon (difference in band gap).
d) The difference between the lattice constant in Germanium and that of Silicon allowed the X-ray probe depth to be matched with the optical excitation depth using the fact that under the appropriate angle of incidence, the Bragg condition can be satisfied for the Germanium film only.

e) Having a thin film as a sample also allowed the diffraction signals to be described using the kinematic approach: changes in the integrated reflectivity of the diffraction signal directly reflect the Debye-Waller effect.

If an optical pulse interacts with a solid, the energy of the pulse is initially deposited in the electron system. After that the energy of the hot electrons is transferred to the lattice until thermal equilibrium is reached. The idea of the experiments presented here is to measure directly the build-up of the incoherent lattice vibrations (lattice heating) after femtosecond optical excitation by observing the temporal evolution of the Bragg-diffraction signal.

The changes of the Bragg-reflection integrated reflectivity caused by heating of the lattice by a couple of hundreds degrees are in the order of several percent. A high accuracy of the measurements is thus required to register such small changes. The following measures were taken in order to perform such accurate measurements:

1) The sample was placed exactly in the focus of the toroidal mirror in order to avoid changes of the Bragg-reflection intensity due to effects connected with the diffraction of convergent (before the focus) or divergent (after the focus) X-rays from the excited sample. The detailed description of these effects and the methods to eliminate them were described in section 4.1.
2) For each time delay between the optical pump and the X-ray probe pulses, the magnitude of the diffraction signal was averaged over 1200 to 3600 laser pulses (this corresponds to 2 - 6 minute exposure times at the repetition rate of 10 Hz). Each average value of the diffracted signal was normalized to the average (over the same pulse sequence) value of the diffracted signal from a Gallium Arsenide crystal, used as a reference of X-ray production (see section 2.3).

Figure 4.11 depicts the measured integrated reflectivity of the Ge (400) Bragg-reflection as a function of time between the optical pump and the X-ray probe pulses for two different excitation fluences (26 and 35 mJ/cm^2). Zero time was put to the point where the diffraction signal starts to decrease. The preliminary adjustment of the zero time described in section 2.3 allowed it to be determined only with the

accuracy of about 200 fs. The values of the integrated reflectivity of the Bragg-reflection are normalized to that without laser excitation. The measurements reveal a clear decrease of the integrated reflectivity within a couple of picoseconds after the excitation down to ~93 and ~95,5 % for the excitation fluences of 35 and 26 mJ/cm^2, respectively.

For both sets of experimental data the decrease of the integrated reflectivity can be fitted by an exponential function with a time constant of τ=1.1 ps. From the measured decrease of the diffracted signal the lattice temperature after a couple of picoseconds can be calculated using the Debye-Waller factor. Using formula (4) in section 4.2.1 one obtains that the lattice temperatures after couple of picoseconds for the two sets of data shown in figure 4.11 are 550 and 460 K. This temperature is in good agreement with the temperature estimated from the heat capacity of Germanium.

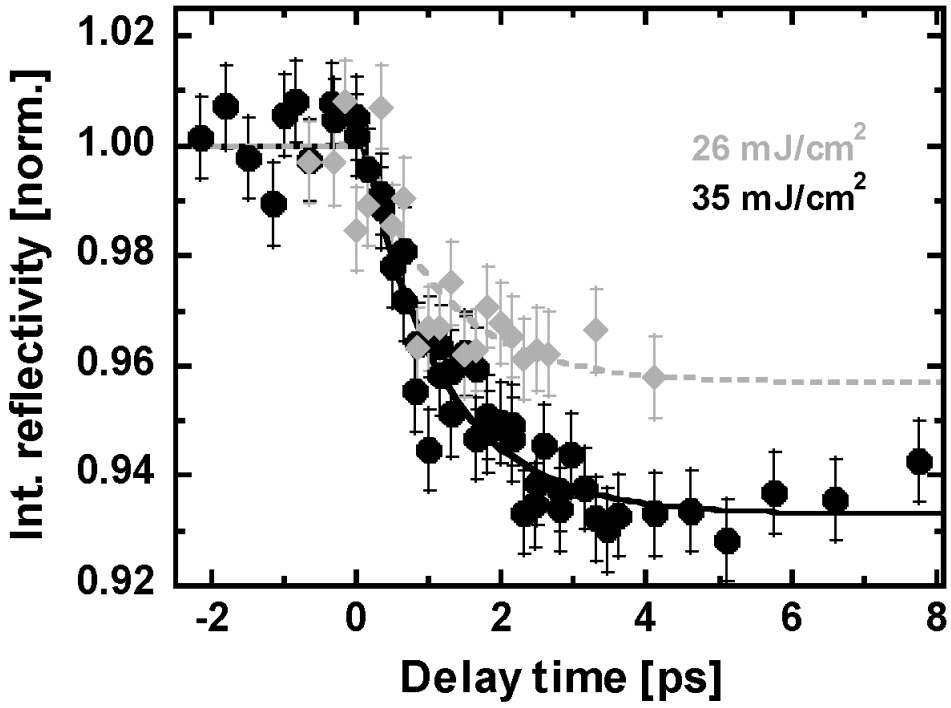

Figure 4.11. Measured time dependencies of the Ge (400) integrated reflectivity after fs-optical excitation.

Figure 4.12 depicts changes in the X-ray diffraction signal for three different Bragg-reflections (111), (311) and (400). As expected, the decrease of the Ge (111) diffraction signal is the smallest. The decrease of the Ge (311) diffraction signal is smaller than the decrease of the Ge (400) diffraction signal and larger than that of the Ge (111) reflection. The ratios of the measured changes are in excellent agreement with those expected from the Debye-Waller factor.

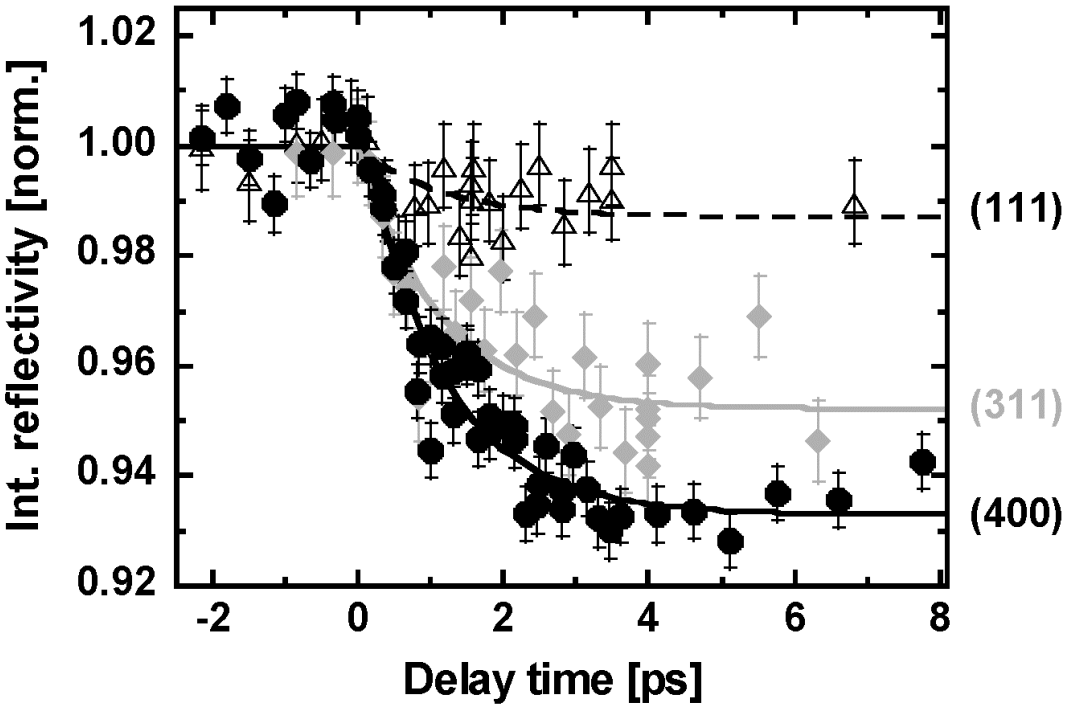

Figure 4.12. Measured temporal dependence of the Ge (400), (311) and (111) integrated reflectivities after fs-optical excitation.

Moreover, the experimental data for all reflections can be fitted with an exponential function with the same time constant t=1.1 ps (independent of the Bragg-reflection order*).

* The same time constant for the decrease of all Bragg-reflections is expected if the changes of the Debye-Waller factor are much smaller than its initial value. In this case the temporal decrease of the Debye-Waller factor just reflects the temporal build-up of the lattice vibrations. This is seen from formula (1) in section 4.1 if one presents the exponential function in this formula as the first two terms of the Taylor series ($e^{-x} \approx 1-x$).

Thus, one can draw the conclusion that the measured changes of the Bragg diffraction signals can be described by the Debye-Waller effect and thus attributed to the build-up of incoherent lattice vibrations. The obtained value of 1.1 ps can be taken as the electron-lattice energy relaxation time in Germanium. This time is in good agreement with the general time range for electron-lattice energy relaxation (see introduction to section 4.2).

Moreover, the experiments described in this section have demonstrated that TRXD can be used to investigate the electron-to-lattice energy transfer during the relaxation of electrons on the ultrafast time-scale.

4.3. Observation of the coherent acoustic phonons in a thin Germanium film after fs-optical excitation

The experiments described in section 4.2 have demonstrated that the energy of optically excited electrons is transferred to the lattice in just a couple of picoseconds. This time is too short for the material to expand. Therefore, directly after the excitation the material is in a transient state in which its temperature has increased but the volume and the lattice constant remained unchanged. Such an isochoric increase of temperature causes in a material the so called thermal pressure [21]. Moreover, the changes of the electron distribution function due to the excited electrons lead to the changes of the atomic interaction potential which causes the so called electronic pressure [21]. Thomsen et al. [20, 21] showed that the pressure induced by an ultrafast optical excitation relaxes by acoustic waves which can be considered as a coherent superposition of a broad spectrum of acoustic phonon modes. A typical time scale for acoustic phenomena is tens of picoseconds, which can be estimated as the ratio of the (typical) thickness of the heated layer (d~100 nm) and the typical speed of sound (a few km/s). The acoustic waves generated by ultrafast optical excitation were observed in a lot of experiments in different materials [22-33, 74, 84-92]. Particular attention should be paid to the fact that different authors have dissimilar and sometimes contradictable estimations of the electronic and thermal pressure contributions to the total pressure causing the acoustic waves.

Rose-Petruck et al. [22], Cavalleri et al. [25] and Lee et al. [30] investigated acoustic waves in GaAs and explained them just by the thermal pressure. Bargheer et al. [29, 84] reported the study on a multilayer GaAs/AlGaAs hetero-structure where the excitation of acoustic phonons in GaAs was attributed just to the electronic pressure. Baumberg et al. [85] measured acoustic phonon wave packets emitted from a single GaAs quantum well surrounded by AlGaAs layers. The generated acoustic phonons were also treated just by using the electronic pressure, whereas the acoustic phonons in GaAs/AlGaAs quantum wells observed by Matsuda [86] were described by both

electronic and thermal pressure contributions. Wright et al. [87] also considered both electronic and thermal pressure contributions to explain the observed acoustic phonon pulses optically excited in a thin slab of GaAs.

The experiments on acoustic phonons in InSb performed by Chin et al [88] were interpreted using only the thermal pressure. Similar measurements in InSb made by Lindenberg et al. [23], Reis et al. [26] and Morak et al. [33] were analysed by taking into account both electronic and thermal pressure contributions. The experimental data obtained by Lindenberg et al. [23] allowed them to estimate the relative strength of the electronic pressure contribution in InSb which was about a factor of two smaller than the thermal one.

Cavalleri et al. [24, 25] detected acoustic waves in a 400-nm-thick Germanium film and could describe them just by the thermal pressure. DeCamp et al. [28] studied acoustic waves in bulk Germanium which were treated using both electronic and thermal pressures. Chigarev et al. [89] explained acoustic pulses generated in bulk Germanium just by the electronic pressure.

Experiments on acoustic waves in Aluminium performed by Park et al. [74] and Tas et al. [90] were modelled by both time dependent electronic and thermal pressure contributions of the driving pressure. The study of coherent acoustic phonons generated in Gold and Silver by fs optical pulses was reported by Wright [91], where the phonon strain pulse shapes were explained by the electronic and thermal pressure contributions.

Wright et al. [92] observed volume contraction in a bulk Silicon crystal after fs optical excitation. The contraction was explained by the dominant electronic pressure contribution to the generated strain waves which is negative in Silicon.

Thus, the experimental data presented in literature for different materials do not give a clear picture about the nature of the pressure driving the acoustic waves after ultrafast optical excitation. For a number of materials, depending on particular

experimental conditions, the observed acoustic waves were described by completely different approaches, i. e. using either only the thermal or only the electronic or both pressure contributions. It is worth mentioning that the acoustic waves generated by "weak" optical excitation with fluences of about 0.1 mJ/cm^2 were explained mostly by the electronic pressure only, whereas the acoustic waves generated by "strong" excitation with fluences of about 10 mJ/cm^2 were explained mostly either by only the thermal or by both the thermal and electronic driving pressure contributions. The experiments with low excitation fluences are typically optical pump/probe experiments [85-87, 89-92]. The experiments with high excitation fluences are typically optical pump/X-ray probe or optical pump/electron probe experiments [22-26, 28-30, 33, 74, 84, 88].

The experiments described in this section reveal that some contradictions between the explanations of the nature of the driving pressure presented by different authors are only apparent. In particular, they clarify why for one and the same material depending on the experimental conditions, the acoustic waves can be explained either only by the electronic or only by the thermal or by both driving pressure contributions.

This section is structured as follows:

Subsection 4.3.1 discusses the theoretical expectations on the magnitudes and temporal dependencies of the electronic and thermal pressure contributions.

Subsection 4.3.2 presents measurements on the acoustic phonons in Germanium generated by ultrafast optical excitation. The results of the measurements are compared with the expectations given in section 4.3.1 and with the measurements published in literature. A comparison of the measured data with the theoretical model made it possible to estimate the relative strength of the electronic and thermal pressure contributions. The measured data are in agreement with the experimental data presented in literature.

4.3.1. Electronic versus thermal pressure

The 150-nm-thick Germanium film on a Silicon substrate used for the Debye-Waller measurements described in section 4.2. represents a simple and well defined system if one wants to clarify questions concerning the nature of the driving pressure causing acoustic waves after ultrafast optical excitation. So, the experiments described in section 4.2 revealed that ultrafast optical excitation leads to a homogeneous heating of the film by a few hundred Kelvin already after a couple of ps. As the volume of the sample can not change during this short time a homogeneous rise of the thermal pressure is expected through the whole thickness of the film.
Homogeneous distribution of the excited electrons through the film thickness due to the fast electron diffusion [83] ensures that the electronic pressure is also homogeneous through the whole thickness of the film.

The following paragraphs present a theoretical estimation of temporal dependencies and relative strengths of the electronic and thermal pressures for the experimental conditions.

Optical excitation of a semiconductor causes changes of the distribution functions of electrons and phonons $n_e(k)$ and $n_p(k)$ and consequently gives rise to stress (or pressure) in the sample under investigation [21].
Suppose the changes of the distribution functions of electrons and phonons are $\delta n_e(k)$ and $\delta n_p(k)$, respectively, then the induced stress σ is [21]:

$$\sigma = \sum_k \delta n_e(k) \frac{\partial E_K}{\partial \eta} + \sum_k \delta n_p(k) \hbar \frac{\partial \omega_K}{\partial \eta} \qquad (1)$$

E_k is the energy of an electron and ω_k is the frequency of a phonon of wave vector k, η denotes strain, $\hbar$ is the Plank's constant.

The first term in equation (1) is an electronic contribution to the stress associated with the deformation potential $\partial E_k/\partial\eta$. As electrons and holes after their thermal interband relaxation are located near the edges of the conduction and valence bands one can write the first term of equation (1) as follows:

$$\sigma^{e} = \frac{\partial E_g}{\partial \eta}\delta n_e = -B\frac{dE_g}{dP}\delta n_e \tag{2}$$

E_g is the band gap, P denotes pressure, δn_e is the total number of electrons in the conduction band (equal to the number of holes δn_p).

The second term in equation (1) describes the thermal stress. For each absorbed photon with energy E thermal phonons of total energy ($E-E_g$) are produced. For phonons described by a thermal distribution the second term in (1) can be written as [21]:

$$\sigma^{th} = -\frac{3B\beta}{c}(E - E_g)N_0 \tag{3}$$

B is the bulk modulus, c is the thermal capacity β is the linear thermal expansion coefficient, and N_0 is the concentration of electrons in the conduction band after optical excitation. It can be estimated by the following equation:

$$N_0 = (1-R)\cdot\left(1-e^{-\frac{d}{\xi}}\right)\cdot\frac{F}{E\cdot d} \tag{4}$$

F is the excitation fluence, E is the phonon energy of the incident light, R is the reflectivity, d is the film thickness, ξ is the absorption depth. For typical experimental conditions: R = 0.17, d = 150 nm, ξ = 200 nm [93], F = 35 mJ/cm^2, E = 1.55 eV one obtains:

$$N_0 \sim 4 \cdot 10^{21} \frac{1}{cm^3} \tag{4a}$$

The corresponding value of the thermal stress estimated by formula (3) is $\sigma^{th} \sim 4 \cdot 10^8$ Pa.

The ratio of the electronic to thermal pressure using equations (2) and (3) can be written as:

$$\frac{\sigma^e}{\sigma^{th}} = \frac{dE_g}{dP} \frac{c}{3\beta(E - E_g)} \tag{5}$$

For $dE_g/dP = 5.1\ 10^{-3}$ eV/kbar; $c = 1.98\ 10^6$ J/m^{3}K; $\beta = 5.9\ 10^{-6}$ K^{-1}; E = 1.55 eV; E_g = 0.66 eV [82, 94] one gets:

$$\frac{\sigma^e}{\sigma^{th}} = 6.3 \tag{6}$$

This estimation suggests that for the given experimental conditions the electronic pressure contribution should be many times larger than the thermal one.

Attention should be drawn to the fact that the thermal pressure depends only on the initial concentration of the electron-hole pairs and is time-independent as long as cooling due to heat conduction can be neglected. Krenzer et al. [95] showed that the temporal evolution of the film temperature can be described by an exponential law with a time constant:

$$\tau = \frac{c \cdot \rho \cdot d}{\sigma_K} \tag{7}$$

ρ is the density of Germanium and σ_K is the thermal boundary conductance for the Germanium-Silicon interface. For the experimental conditions c = 310 J/(kg K), ρ = 5323 kg/m^3, d = 150 nm, $\sigma_K = 10^4$ W/(K cm^2) [94, 96] the cooling time is equal to

$$\tau = 2.5\,\mathrm{ns} \tag{7a}$$

Thus, for $t \le \frac{\tau}{10} = 250\,\mathrm{ps}$ the cooling of the film can be neglected within less than 10 % error.

On the other hand the electronic pressure depends on the momentary concentration of the excited electron-hole pairs and is thus time-dependent. The concentration of the excited electron-hole pairs decreases over time due to interband relaxation of the excited carriers via Auger recombination. It leads to the decrease of the electronic pressure contribution.
The relaxation rate of the Auger recombination is given by:

$$\frac{\partial N}{\partial t} = -\gamma(N) \cdot N^3 \tag{8}$$

N is the concentration of excited electron-hole pairs, γ(N) is the Auger parameter. According to Yoffa [97] the Auger parameter can be expressed as:

$$\gamma(N) = \frac{\gamma_0}{\left(1 + \frac{N}{N_C}\right)^2} \tag{9}$$

N_C is the critical carrier density at which a sufficiently dense plasma screens the Coulomb interaction between carriers, γ_0 is the Auger parameter for $N \ll N_C$. For crystalline Germanium $\gamma_0 \sim 10^{-30}\,\mathrm{cm}^6/\mathrm{s}$ [94] and $N_C = 0.25 \cdot 10^{21}\,\frac{1}{\mathrm{cm}^3}$.[97].

For $N \gg N_C$ the relaxation rate of the Auger recombination can be expressed as:

$$\frac{\partial N}{\partial t} = -\gamma_0 \cdot N_C^2 \cdot N \tag{10}$$

This formula describes an exponential decay with the time constant:

$$\tau_{exp} = \frac{1}{\gamma_0 \cdot N_C^2} \tag{11}$$

For the value of γ_0 and N_C given above the time constant is equal to $\tau_{exp} = 16\,ps$.

When the concentration of the excited electrons decreases and becomes comparable to N_0, the decay time increases and becomes dependent on the momentary concentration of electrons:

$$\tau = \frac{1}{\gamma_0 \cdot N^2}\left(1 + \frac{N}{N_C}\right)^2 \tag{12}$$

If N gets much smaller than N_C, then the decay time can be written as:

$$\tau = \frac{1}{\gamma_0 \cdot N^2} \tag{13}$$

which also depends on the momentary concentration of electrons.

For the experiments described in this thesis the initial concentration of electrons $N_0 = 4 \cdot 10^{21} \frac{1}{cm^3}$ is significantly larger than the critical concentration $N_C = 0.25 \cdot 10^{21} \frac{1}{cm^3}$. Thus, the initial decrease of the excited carrier concentration is described by the screened Auger recombination with the constant recombination time given by formula (11). When the concentration of excited electrons becomes comparable to or smaller than N_C, then the decay time starts to be dependent on the momentary concentration of electrons.

To get an estimate of how much time electrons need to recombine the real decrease of their concentration can be fitted by an exponential function with some time constant τ_a. This represents the average time-constant for recombination of the excited carriers which starts as screened and finishes as unscreened Auger recombination. Figure 4.13 depicts the carrier density calculated by formulas (8) and (9) and its exponential fit. As one can see, an exponential function can fit the calculated dependence quite well. The time constant of the exponential fit in figure 4.13 is 23 ps.

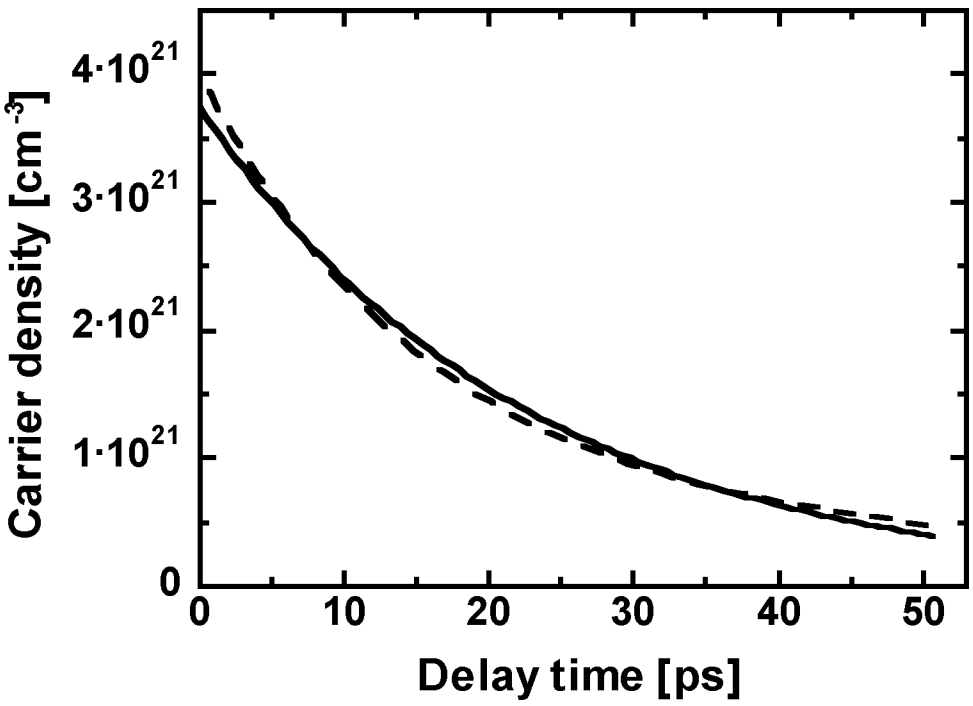

Figure 4.13. Temporal dependence of the carrier density for the Auger recombination calculated by formulas (8) and (9) (dashed line) and its exponential fit (solid line).

The electronic pressure which according to formula (2) is proportional to the concentration of the excited electrons can also be fitted by the same exponential law:

$$P_{el}(t) = P_0 \cdot \exp\left(-\frac{t}{\tau_a}\right) \tag{14}$$

P_0 is the electronic pressure at t = 0.

Consequently, for the experimental conditions the expected life-time of the electronic pressure is about a few tens of picoseconds and this comparable to the characteristic acoustic time $T = d / c_{sound}$.

It is important to note that the general conclusions concerning the behavior of the acoustic waves caused by this pressure do not depend too critically on the particular temporal dependence describing the monotonic decrease of the electronic pressure. An exponential dependence with a certain time constant just allows a simple and clear description of the measured data, as one can see in section 4.3.2.

4.3.2. Measurements of acoustic waves in Germanium

The lattice constant changes associated with acoustic waves can be observed by measuring the time dependent angular profiles of the Bragg-reflections ("rocking curves") from the sample under investigation. Figure 4.14 depicts measured rocking curves of the Ge (111) Bragg-reflection for different time delays after the optical excitation using a pump fluence of 35 mJ/cm^2, that is in the range of "strong" fluences for which typically electronic and thermal pressure contributions were considered to model the experimental results. The dashed line shows the rocking curve without laser excitation.

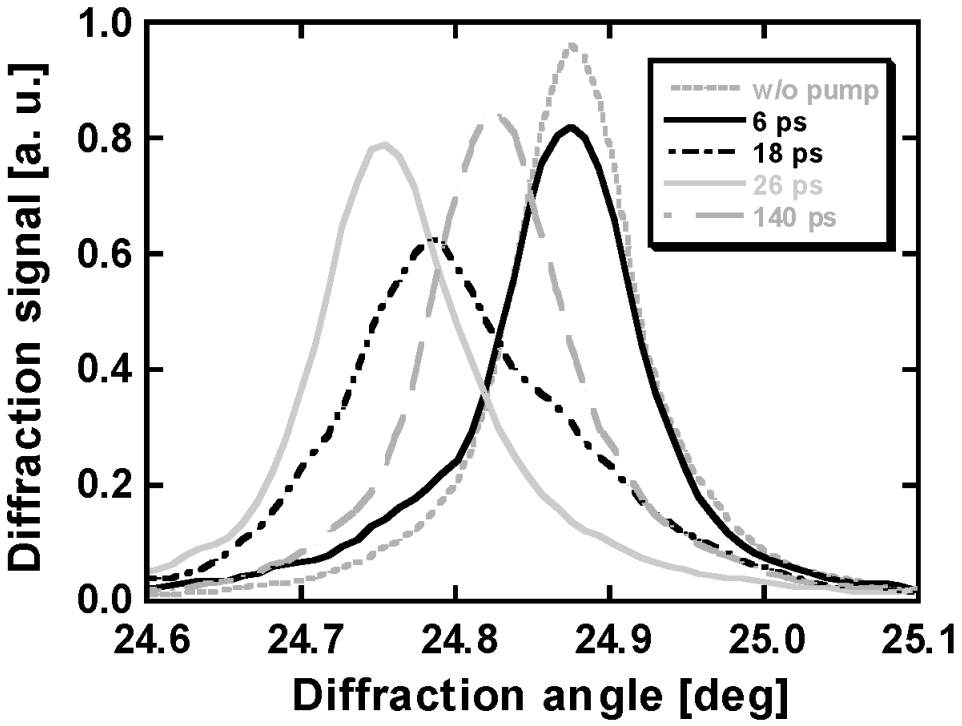

Figure 4.14. Measured rocking curves of the Ge (111) Bragg-reflection from Germanium for different time delays after femtosecond excitation.

As expected, an initial shift of the rocking curve to smaller Bragg-angles is observed, indicating an expansion of the lattice. The maximum angular shift is observed at 27 ps time delay. The curve for 140 ps represents the profile of the rocking curve when the temporal evolution of the measured rocking curves caused by the generated

acoustic waves is finished. The measured angular shift of ~0.05 deg for this time delay is due to thermal expansion. This shift corresponds to an increase of the lattice temperature up to 520 K. Attention should be paid to the fact that the lattice temperature measured in this way is in good agreement with the temperature obtained from the Debye-Waller measurements described in section 4.2.
The observed strong broadening of the rocking curve profiles over time suggests that the sample lattice is non-homogeneous strained.

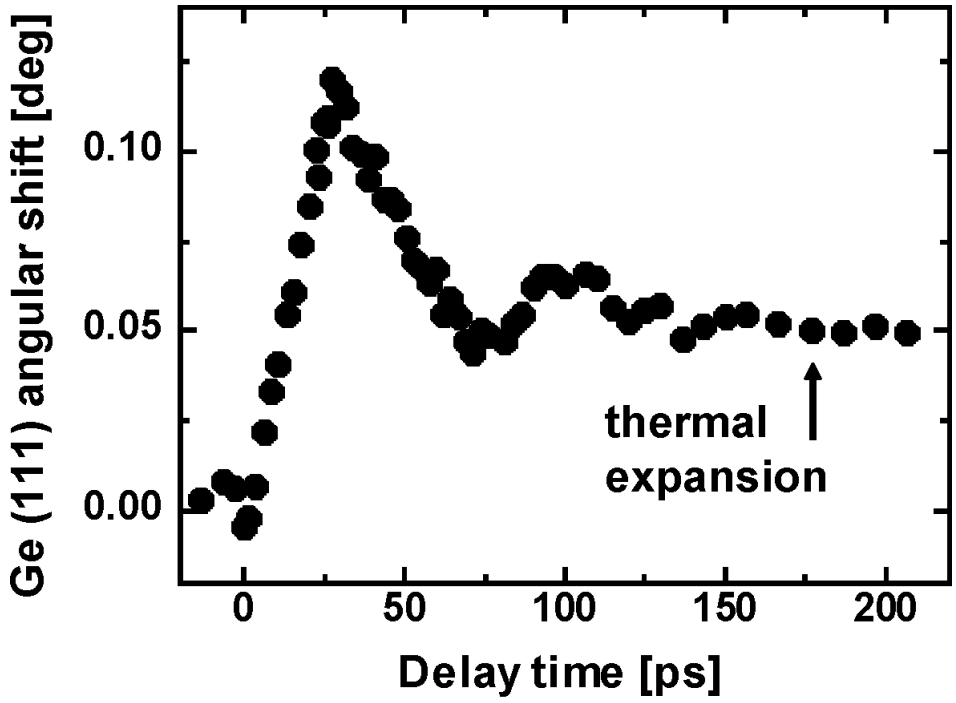

Figure 4.15. Angular shift of the Ge (111) rocking curve centre of gravity.

To quantitatively visualize the temporal changes of the rocking curves figure 4.15 shows the angular shift of the rocking curve centre of gravity versus time. An oscillating behaviour of the angular shift is observed. It can be seen in figure 4.15 that the Bragg-reflection moves initially towards smaller angles. The angular shift reaches its maximum after T = 27 ps. This time is equal to the time which an acoustic wave needs to travel through the thickness of the Germanium film ($T = (150\,\mathrm{nm})/(5555\,\mathrm{m/s}) = 27\,\mathrm{ps}$). After that recompression of the film takes place which leads to a shift of the Bragg-reflection back towards larger Bragg-angles. The

minimum of the angular shift is followed by a secondary maximum and minimum. After a time t~150 ps the position and the shape of the Bragg-reflection remain essentially unchanged and the shift of the Bragg-reflection corresponds to the angular shift due to thermal expansion, as discussed above. Cooling of the film due to heat conduction on this time scale can be neglected, as discussed in section 4.3.1.

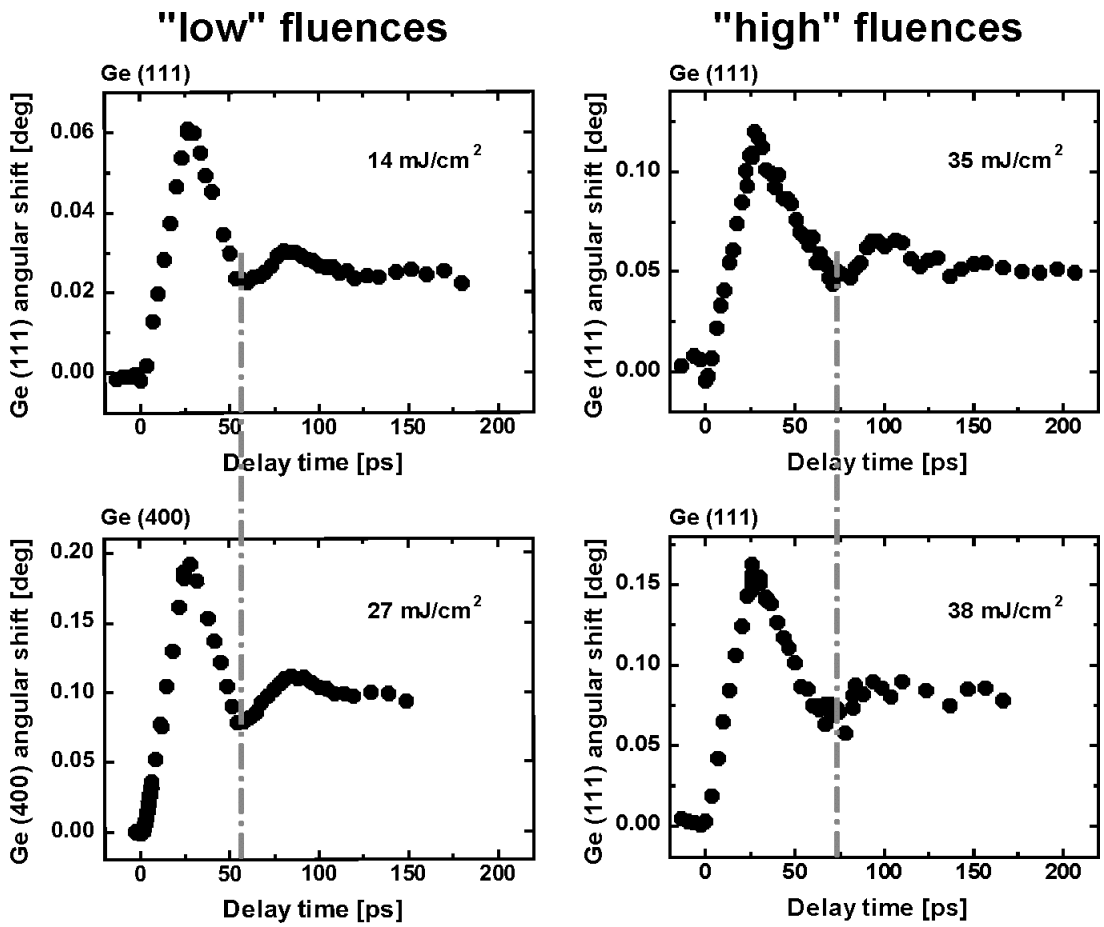

Figure 4.16. Temporal dependencies of the angular shifts for different excitation fluences.

A similar kind of behaviour was observed for different laser excitation fluences and different Bragg-reflections. Figure 4.16 depicts the measured temporal dependencies of the angular shifts for excitation fluences of 14, 27, 35 and 38 mJ/cm^2 for the Ge (111) and Ge (400) reflections (see also the measurements of acoustic waves presented in section 4.1). As one can see, the oscillations of the angular shifts are

observed for all fluences. A few points should be noted: (i) All measured time dependencies exhibit a ratio of the angular shift at 27 ps (maximum expansion) to the asymptotic shift equal to approximately 2…2.5. (ii) The time for recompression (the time between the first maximum and the first minimum) is 27 ps only for “low” fluences but almost twice as long for “high” fluences.

In an attempt to understand the observed behaviour, in particular the differences between “low” and “high” fluences, model calculations have been performed. The model describes the acoustic response upon impulsive excitation and uses the dynamical X-ray diffraction theory to calculate the diffracted signal from a non-homogeneously strained material.

It is assumed in the model, that the excess pressure in the film causes rarefaction waves which start to propagate from the Germanium interfaces into the bulk of the Germanium film. Likewise, it causes a compression wave which starts to propagate from the Germanium-Silicon interface into the bulk of Silicon. After the time determined by the film thickness and the sound speed the fronts of the strain pulses traveling in Germanium arrive at the opposite interfaces. The wave which reaches the Germanium-vacuum interface is completely reflected back (with change of sign). The wave reaching the Germanium-Silicon interface is partly transmitted to the Silicon substrate and partly reflected back. The amplitudes of the reflected waves are determined by the acoustic impedances of the interfaces.
The waves transmitted to the Silicon substrate from the Germanium film propagate from the interface into the bulk of the Silicon substrate and do not influence the waves propagating in the Germanium layer. These acoustic waves traveling in the sample consist of a broad spectrum of coherent phonon modes. The shape of the acoustic waves is determined by the time and spatial dependencies of the driving pressure.

In the simplest case one can assume that the driving pressure is constant (“simple acoustic model”).

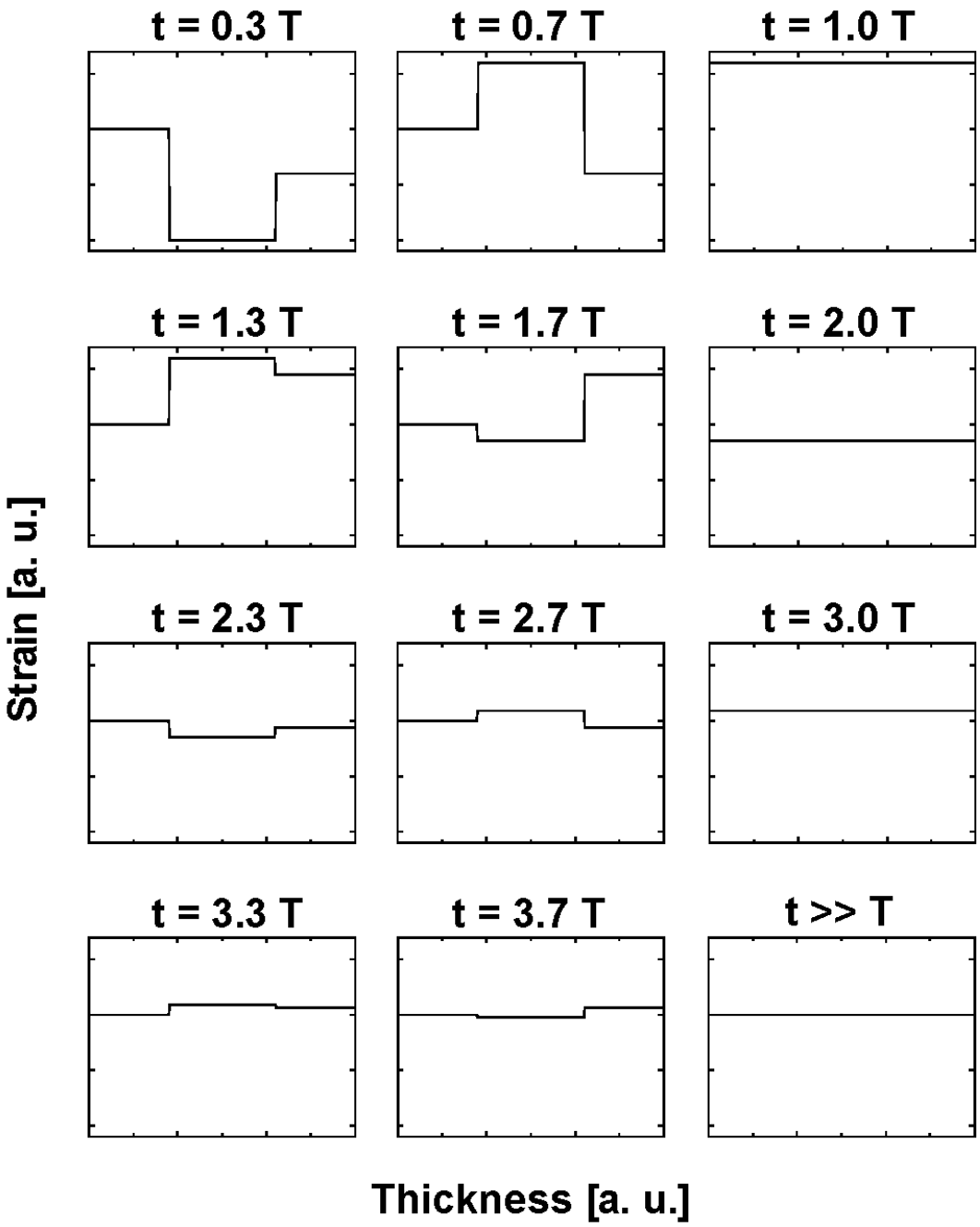

Figure 4.17. Simulation of the strain in a thin Germanium film on a Silicon substrate for different time delays after optical excitation. The Silicon substrate is assumed to be at the right interface of the Germanium layer. The left interface is free. Calculations are done in frames of the "simple acoustic model" where the driving pressure is assumed to be constant over time.

This case corresponds to the physical situation in which the driving pressure consists only of the thermal pressure which is independent of time and determined by the energy deposited into the Germanium film by the femtosecond laser pulse. Under these assumptions the solution of the acoustic equation results in a rectangular profile of the strain waves propagating in the Germanium film. The calculated strain profiles of the Germanium film for different time delays are shown in figure 4.14. The sum of the acoustic waves at t = T, 2T, 3T results in a homogeneous strain over the whole thickness of the film. As can be seen from figure 4.17 there is a final strain left in the Germanium film. This strain is determined by the thermal expansion of the material.
The angular shift of the Bragg-reflection centre of gravity caused by the strain waves described above was calculated using the dynamical theory of X-ray diffraction [98-100]. The result of these calculations for the Ge (111) reflection for an excitation fluence of 14 mJ/cm^2 is depicted in figure 4.18.

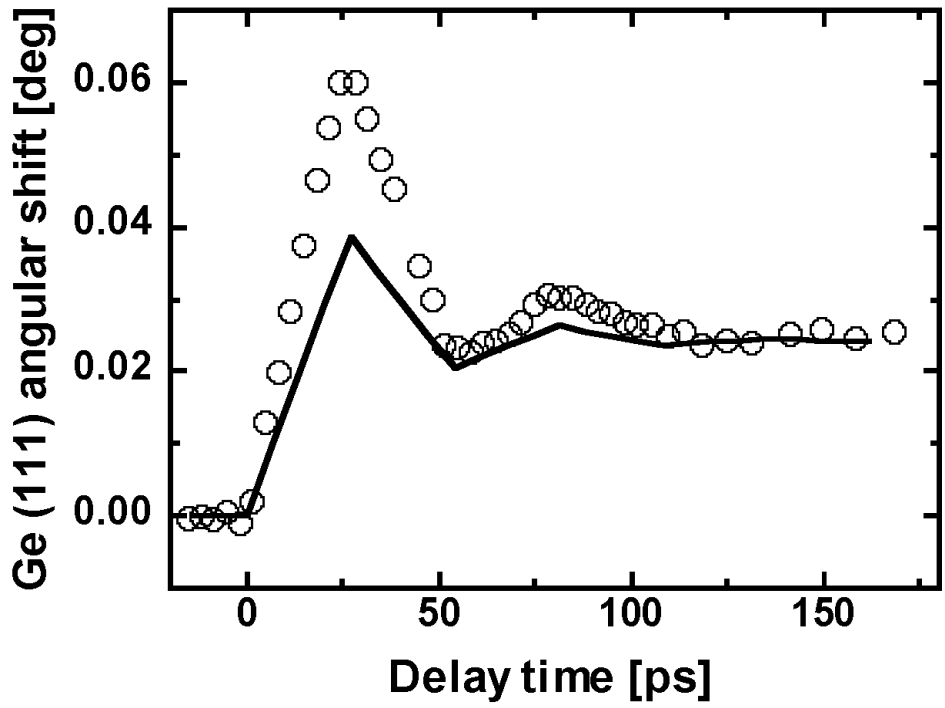

Figure 4.18. Temporal dependence of the angular shift of the rocking curve calculated in frames of the “simple acoustic model” taking into account only thermal pressure. Open circles represent the measured data.

It can be seen that the developed model qualitatively describes the measured oscillating behaviour of the diffracted signal but nevertheless there are quantitative disagreements between the model and the experimental data. Firstly, the ratio of the maximum-to-asymptotic angular shift in the experimental data is 2…2.5, whereas in the theoretical model it is just 1.6. The ratio of 1.6 obtained from the theoretical model is determined by the acoustic impedances of Germanium and Silicon, and independent of the value of excitation fluence. Secondly, the model does not explain the large value of the recompression time for “high” fluences shown in figure 4.16. The disagreements mentioned above suggest that the simple acoustic model with constant driving pressure is not complete and further development is required.

A better qualitative description of the experimental data can be expected by considering a time-dependent driving pressure.

One consideres here the case when the driving pressure decreases over time. This case corresponds to the physical situation in which a significant amount of electrons is excited into the conduction band. Photoexcitation of electrons and holes leads to an increase of the electronic pressure which is approximately proportional to the concentration of the excited electron-hole pairs (see section 4.3.1). Due to recombination the electronic pressure decreases over time.

Figure 4.19 exemplifies the calculated strain profiles as a function of depth for different times after optical excitation. The solid and dashed lines represent the strain profiles for the characteristic decay times of the electronic pressure equal to 40 and 2.55 ps, respectively (these values will be explained later). As one can see, the transient shape of the acoustic pulses resembles the temporal dependence of the pressure. The product of the sound speed and the decay constant gives the scale of the temporal strain profile. No strain caused by the electronic pressure is left over at long time delays.

The temporal dependencies of the X-ray reflection centre of gravity for the strain profiles depicted in figure 4.19 were calculated using dynamical X-ray diffraction theory. The result of this calculation is presented in figure 4.20.

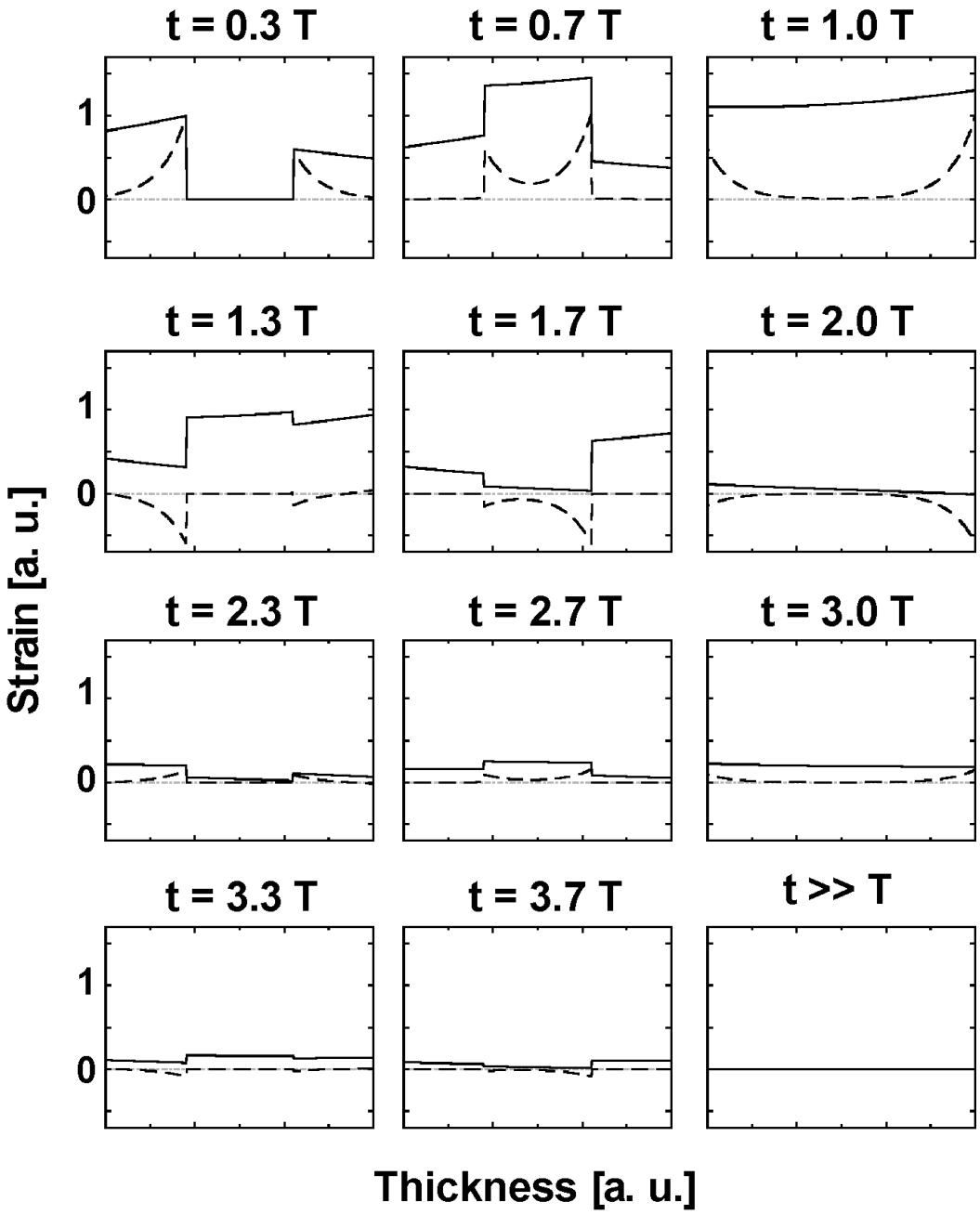

Figure 4.19. Simulation of the strain in a thin Germanium film on a Silicon substrate for different time delays after the optical excitation. The Silicon substrate is assumed to be at the right interface of the Germanium layer. The solid and the dashed lines represent the calculated strains for the driving pressure decay times of 40 and 2.5 ps, respectively.

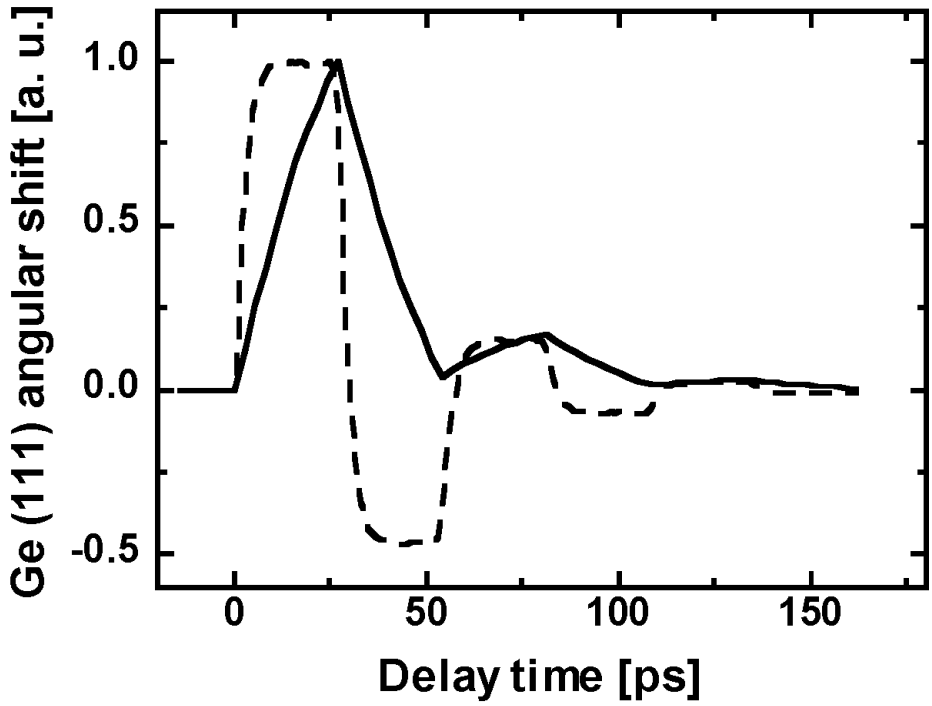

Figure. 4.20. Temporal dependencies of the angular shift of the rocking curves calculated for the strain profiles caused by the acoustic waves driven by the electronic pressure with the decay times of 40 ps (solid line) and 2.5 ps (dashed line).

The temporal dependence of the driving pressure causes an angular shift of the Bragg-reflection which strongly depends on the decay constant of the driving pressure. To qualitatively understand the difference between the two curves in the simplified view the angular shift can be understood approximately as a measure of the average strain. In this case, the rise time of the angular shift reflects directly the life-time of the electronic pressure.

Attention should be paid to the fact that the 2T periodicity of the diffraction signal angular shift is independent of the value of the decay time.

The following consideration will show which values of P_0 and τ_a give the best description of the experimental data.

Suppose the simple estimation of the electronic pressure contribution amplitude presented in section 4.3.1 is valid, and the initial electronic pressure is $P_{el} / P_{th} = 6.3$ times larger than the thermal one. The ratio of maximum-to-asymptotic amplitudes

2.5:1 then determines the electronic pressure decay time τ. For the value of the initial electronic pressure $P_{el} = 6.3 \cdot P_{th}$ obtained from the simple estimation in subsection 4.3.1 one deduces a decay time of τ = 2.55 ps. The corresponding dependence of the calculated angular shift of the Bragg-reflection centre of gravity can be seen in figure 4.21. Evidently, there is clear disagreement between the experimental data and the calculated dependence: The measured increase and decrease of the Bragg-reflection centre of gravity are almost linear with time whereas the calculated dependencies are curved lines. This is because of the strain contribution due to the time-dependent electronic pressure which has a small decay time.

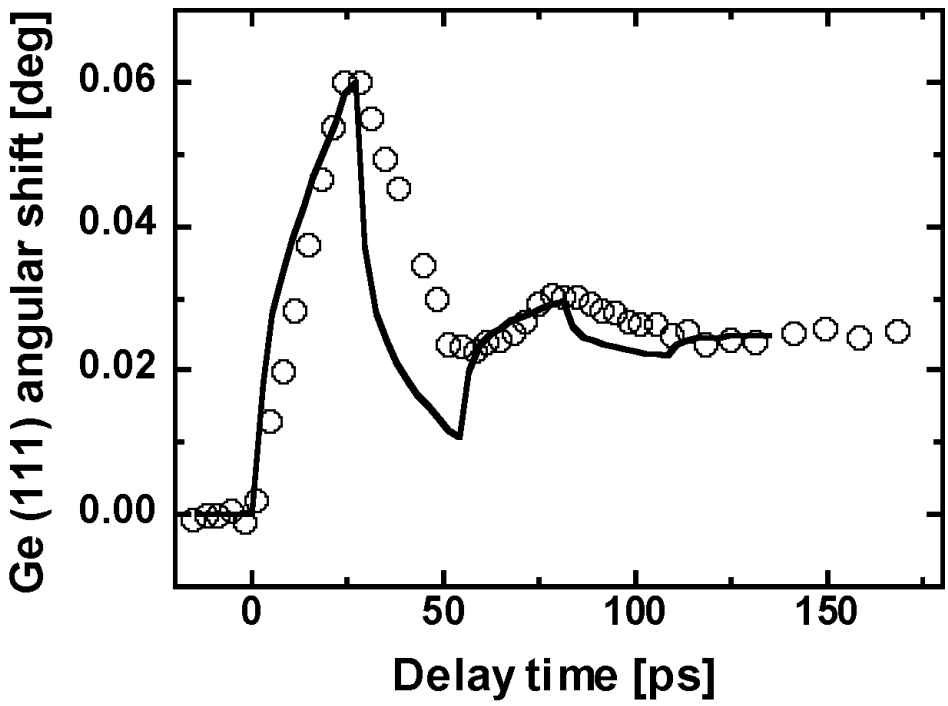

Figure 4.21. Calculated temporal dependence of the Bragg-reflection centre of gravity angular shift.

If one assumes that the decay time is very large compared to T, then the electronic pressure contribution would be present even at t ≥ 150 ps which contradicts the fact that the angular shift measured at this time delay is only due to thermal expansion. A very large value of the decay time would also mean that the electronic pressure is practically constant at the time scale of 100 ps and the acoustic waves can be

described in the frame of the "simple acoustic model" where the ratio of the maximum-to-final angular shift is equal to 1.6. This again contradicts the experimental data.

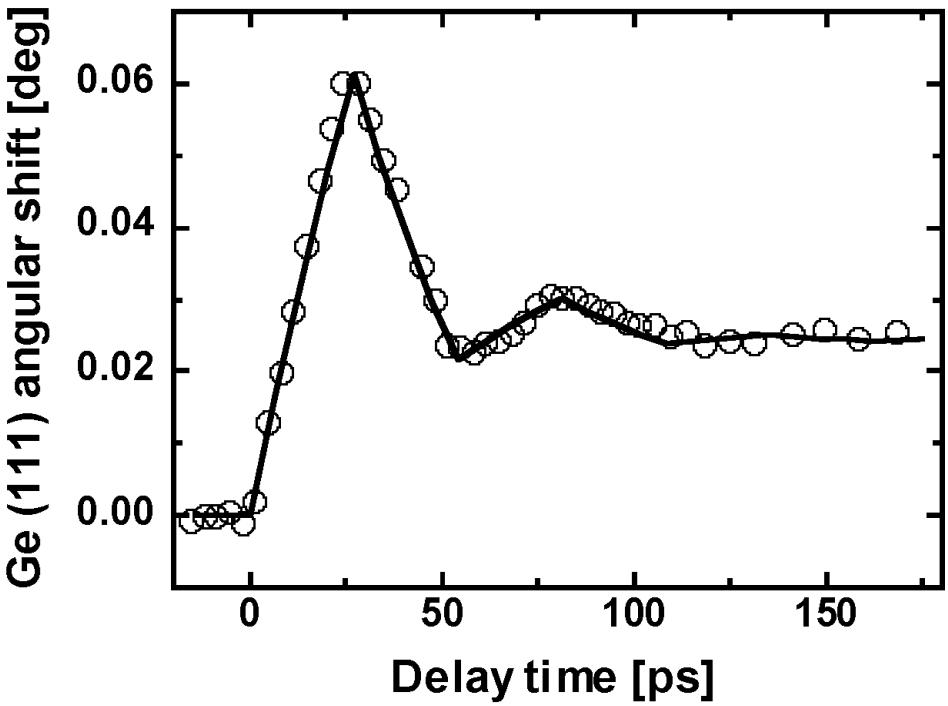

Figure 4.22. Temporal dependence of the Ge (111) Bragg-reflection angular shift. Open circles represent the measured data. Solid line corresponds to the calculated shift in frames of the acoustic model with time-dependent electronic pressure. P_{el}:P_{th} = 0.8, τ = 40 ps.

Thus, the only possibility left is that the decay time is of the order of the acoustic transit time T (τ~T=27 ps). To satisfy the ratio of maximum–to-final amplitude 2.5:1 for these values of τ, one needs to assume that the electronic pressure contribution is significantly smaller than 6.3. The best fit of the experimental data can be obtained for the electronic pressure contributions in the interval P_{el}:P_{th}= 0.7…0.95 with corresponding values of τ ~ 25…65 ps. It should be noted that these values of the decay time are comparable to what is theoretically expected from the Auger recombination rate for Germanium (see section 4.3.1). As an example figure 4.22

shows the fit of the experimental data for an excitation fluence of 14 mJ/cm^2 (the first graph in figure 4.16).
As one can see there is a good agreement between the experimental data and the theoretical model. Thus, including the electronic pressure contribution allowed the maximum-to-final angular shift ratio to be explained. However, the slow recompression observed for “high” fluences cannot be explained by this theoretical model. No matter what kind of time-dependence of the pressure is assumed there is no possibility to change the 27 ps periodicity in this way.

However a doubling of the recompression time is expected when the relative acoustic impedance at the Germanium-Silicon interface is changed. In this case the amplitude of the strain wave reflected from the interface does not change its sign, which means that compression and expansion waves are reflected as compression and expansion waves, respectively. The first minimum of the angular shift would be reached in this case after the twice transit time. The acoustic impedance is determined by the product of the density and the speed of sound and is equal to $2.96 \cdot 10^7$ and $2.18 \cdot 10^7$ kg/(m^2·s) for Germanium and Silicon, respectively [82]. Changes of the acoustic impedance due to the decrease of density can be excluded because the strain observed in the experiments is less than one percent. If the change of the acoustic impedance was connected with the variation of the speed of sound in Germanium, then a doubling of the expansion time should also be observed, but it remains invariable for any excitation fluence. The only possibility left is the change of the speed of sound in Silicon. However, a change of the relative acoustic impedance is expected if the speed of sound increases by 36 %. Since it is difficult to imagine a physical mechanism for such a large change of the speed of sound in Silicon, this represents only a principle possibility to explain the observed doubling of the recompression time.
The analysis of the rocking curves profiles described in the subsection “Rocking curves” will disclose that the slow recompression is not the only feature observed for the “high” excitation fluences which cannot be described by the theoretical model.

Delayed expansion

Another way to investigate the electronic pressure contribution is to observe the angular shift of the Bragg-reflection at very early time delays.

The electronic pressure is expected to appear directly after the optical excitation whereas the thermal pressure should grow “slowly” reflecting the increase of the lattice temperature. For Germanium the increase of the thermal pressure can be modelled by an exponential function with the time constant of 1.1 ps , according to the measurements presented in section 4.2. Thus, the angular shift of the Bragg-reflection measured directly after the optical excitation should be caused only by the electronic pressure contribution.

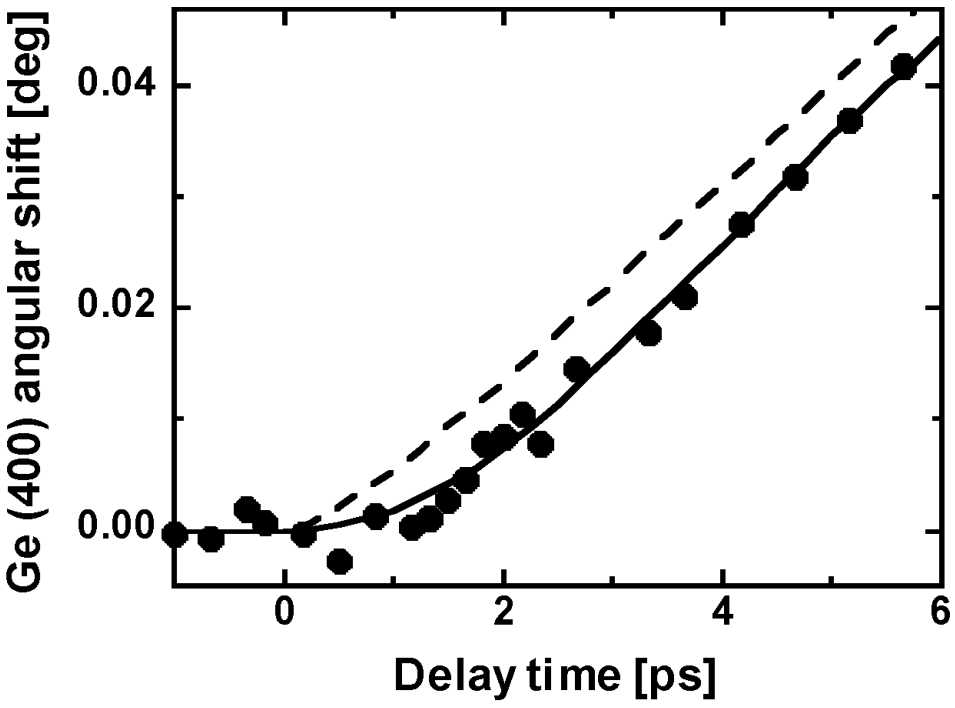

Figure 4.23. Angular shift of the Ge (400) Bragg-reflection centre of gravity after optical excitation. The filled circles correspond to the measured data. The solid line represents the calculated angular shift when the rocking curve is cut by a 1.5 degree angular window. The dashed line depicts the calculated angular shift of the complete rocking curve.

The filled circles in figure 4.23 show the measured shift of the Ge (400) Bragg-reflection centre of gravity during the first picoseconds after optical excitation. It can be clearly seen that the shift of the rocking curve centre of gravity is delayed by approximately 1 ps with respect to the optical excitation. However, this is not evidence for a delayed driving pressure. Modelling of the measured data revealed that this delay is apparent and produced by the limited angular width of the X-rays coming to the sample from the toroidal mirror. The calculated shift of the rocking curve cut by a 1.5 deg angular window fits the experimental data perfectly compared to the fit of the angular shift using the complete rocking curve (see figure 4.23).

Thus, the onset of the sample expansion due to the instantaneous driving pressure can not be seen in the angular shift of the Bragg-reflection because of the limited angular range of the X-rays incident on the sample. Therefore the shift of the Bragg-reflection caused by the electronic pressure contribution cannot be separated at early times using the current experimental set-up.

Rocking curves

Up to this point the analysis of acoustic waves was made by treating the periodic changes of the rocking curve centre of gravity. A complementary approach is to look at the shape of the rocking curves. In doing this it turned out that there is a difficulty even for the unexcited case. The measured rocking curve is broader than the calculated one and has no additional maxima in the wings.

Figure 4.24 depicts the measured and the calculated rocking curves of the Ge (111) reflection. The measured rocking curve is determined by the convolution of the calculated rocking curve with the apparatus function which includes broadening due to the experimental set-up (source size, optic) and also sample imperfections. The “real” apparatus function was approximated by a Lorenz-function with the width determined by the condition that the convolution of the calculated rocking curve for the unperturbed sample with the Lorenz-function gives a profile maximally close to that of the measured rocking curve. The solid line in figure 4.24 presents a convolution of the calculated rocking curve with the Lorenz-function having a FWHM = 0.026 deg.

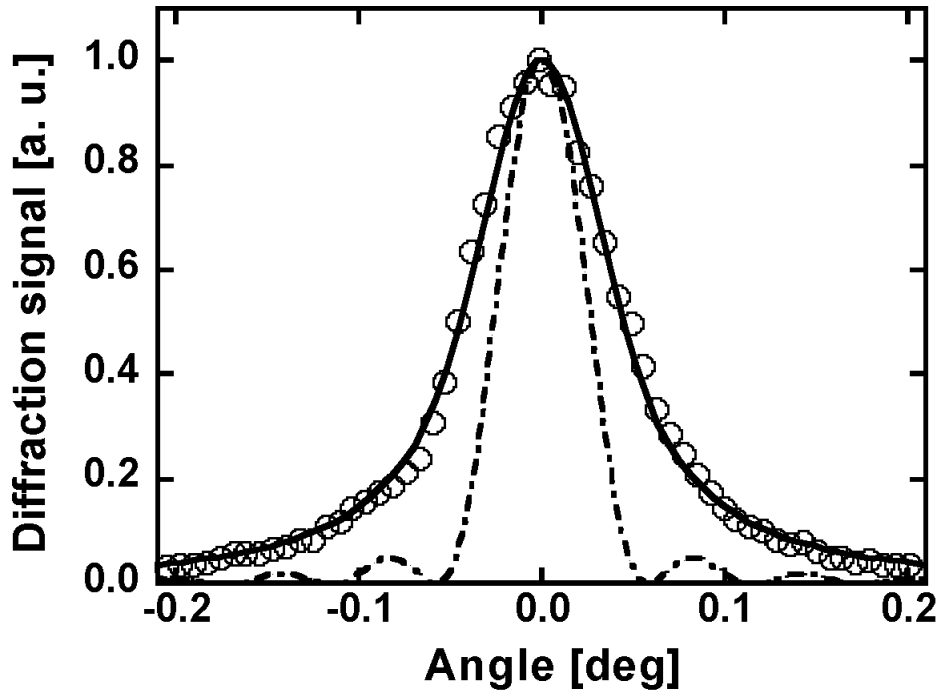

Figure 4.24. Ge (111) reflection rocking curves. The blank circles represent the measured rocking curve. The dashed-dotted line is the rocking curve calculated using the dynamical X-ray diffraction theory. The solid line represents the rocking curve obtained by convoluting the calculated rocking curve with the apparatus function.

Figure 4.25 presents the calculated, convoluted and measured rocking curves for different times after the optical excitation with a fluence of 14 mJ/cm^2. The comparison of the measured and calculated data shows that the temporal evolution of the measured rocking curves are well described by the model presented above.

A similar comparison was made for the "high" excitation regime where the long recompression time was observed (see figure 4.16). The result of the comparison for the excitation fluence of 35 mJ/cm^2 is depicted in figure 4.26. There is again qualitative agreement between the measured and the calculated temporal evolution of the rocking curves. However, the quantitative differences between them are significantly larger than in the case of "low" fluence (see figure 4.25). In particular, the measured rocking curves depicted in figure 4.25 are broader than the calculated ones for all positive time delays.

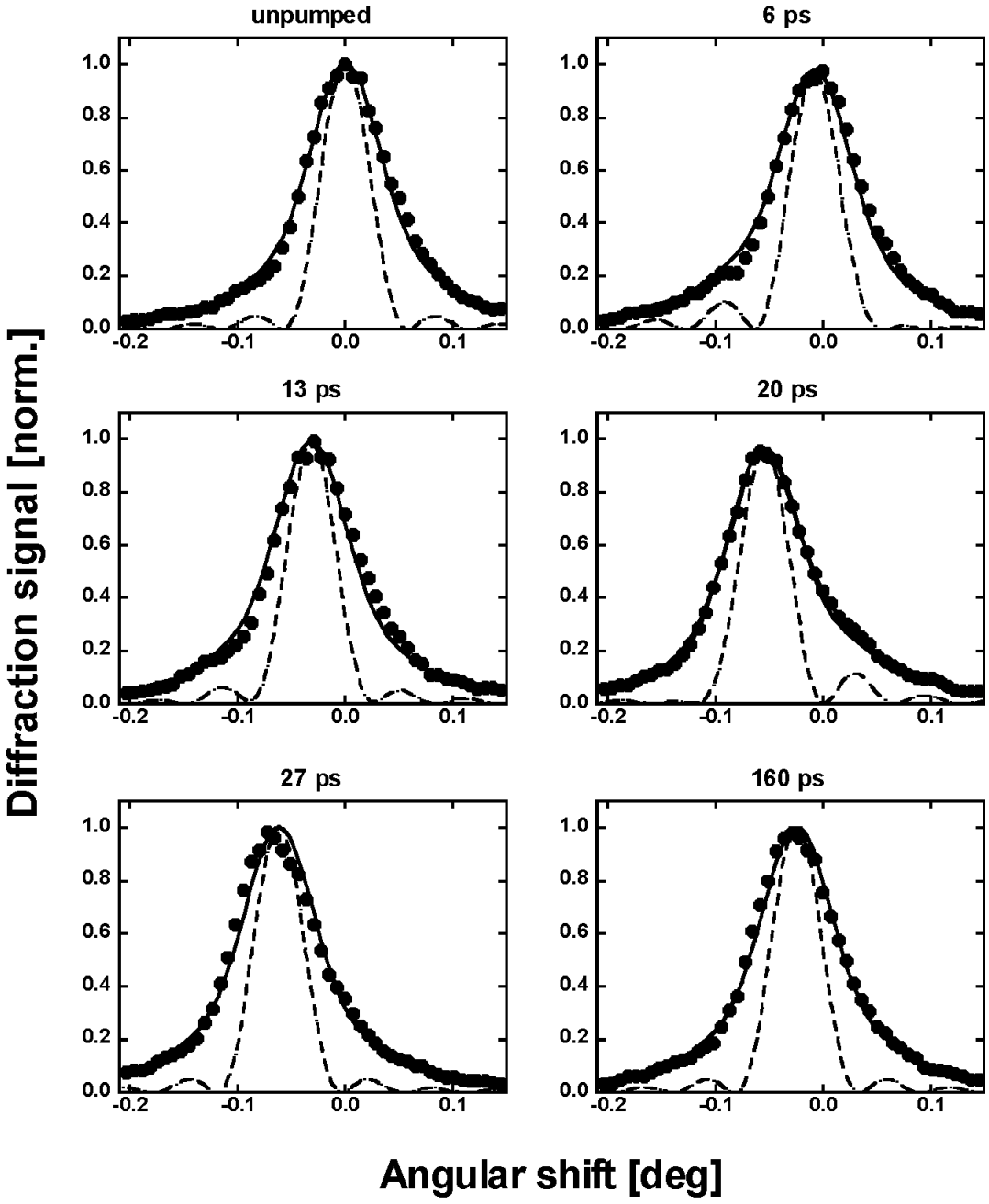

Figure 4.25. X-ray diffraction signal as a function of angle for different times after optical excitation with a fluence of 14 mJ/cm^2. The filled circles represent the measured rocking curves. The dashed lines show the calculated rocking curves. The solid lines depict the convolutions of the calculated rocking curves with the apparatus function.

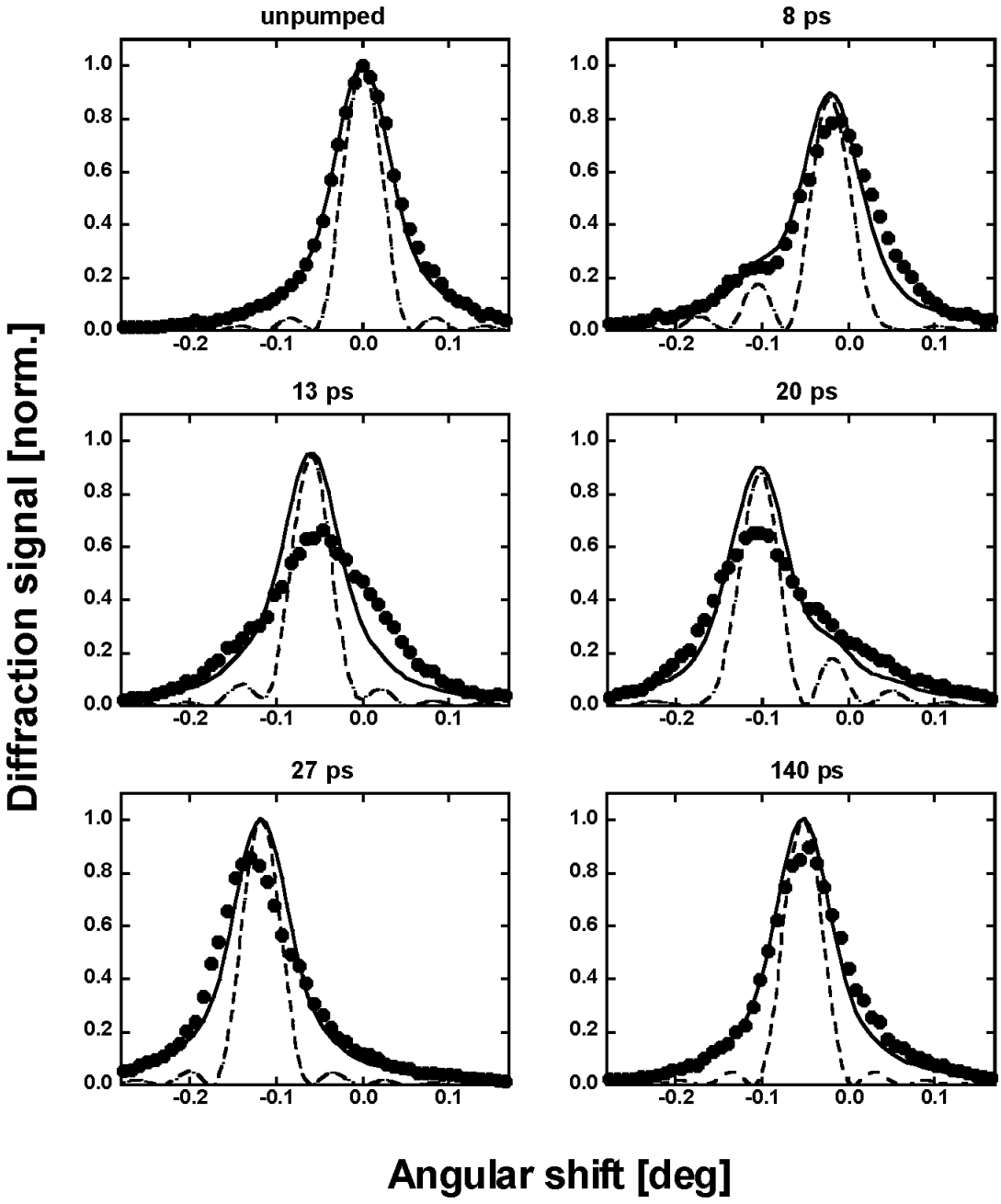

Figure 4.26. X-ray diffraction signal as a function of angle for different times after optical excitation with a fluence of 35 mJ/cm^2. The filled circles represent the measured rocking curves. The dashed lines show the calculated rocking curves. The solid lines depict the convolutions of the calculated rocking curves with the apparatus function.

This observation together with the observation of the “slow” recompression indicates that the theoretical model presented here is incomplete for the description of the measured data in the “high” excitation fluences regime. The broader profiles of the rocking curves measured for the “high” excitation fluences indicate that the sample strain has a more complicated spatial profile than that predicted by the model. This might be due to spatially non-homogeneous electronic and thermal pressure contributions over the film thickness which can be caused, for example, by a nonlinear absorption for the “high” fluences.

To summarise, acoustic phonons were observed in a thin Germanium film after femtosecond laser excitation. A model combining the dynamical X-ray diffraction theory and calculations of the temporal evolution of acoustic waves was developed. The developed model made it possible to describe the observed acoustic strain waves and to estimate the electronic pressure contribution in Germanium after femtosecond optical excitation.
The difference between the electronic pressure measured in the experiment and that expected from the theoretical estimation is most probably due to the fact that the theoretical estimation is made under the assumption that all excited electrons and holes are located near the edges of the conduction and the valence bands. In reality the excited electrons and holes are, generally speaking, distributed over the different energy levels within the Brillouin-zone. In this case the following information is required to obtain a direct calculation of the electronic pressure: (i) the deformation potentials of the energy levels in the Brillouin-zone for the excited material and (ii) the distribution function of the excited carriers. However, this information is not easily available for the experimental conditions.

On the other hand, the small value of the electronic pressure contribution in comparison with the theoretically estimated one is not entirely unexpected. The measurements of acoustic waves in a bulk InSb sample for approximately the same excitation conditions (excitation fluence 15 mJ/cm^2, excitation wavelength 800 nm) made by Lindenberg at al. [23] revealed that the electronic pressure was about a factor of two smaller than the thermal one. However, the estimation using the

theoretical model presented in section 4.3.1 gives a ratio of the electronic to the thermal pressure which is equal to $P_{el} / P_{th} = 7$ according to formula (5) of subsection 4.3.1. The values for calculation are taken from [94].

Thus, the measurements on another material also exhibit an electronic pressure contribution which, for similar excitation conditions, differs from that obtained using the simple theoretical estimation presented in section 4.3.1.

A better agreement between the experimental data and the theoretical model is expected for lower pump fluences when a smaller number of electrons is excited because in this case the excited carriers are expected to be located closer to the edges of the valence and conduction bands.

Furthermore, the decay time of the excited carriers in this case should be much larger than in the case of “strong” excitation, as follows from formula (13) in section 4.3.1. Therefore, the electronic pressure caused by the “weak” excitation in Germanium is expected to be dominant over a long time, according to the formulas (5) and (13) in section 4.3.1. So, the experiments on acoustic waves in bulk Germanium for the excitation fluence of 0.04 mJ/cm^2 performed by Chigarev [89] were explained by assuming a constant electronic pressure contribution and neglecting the thermal one which fits the theoretical model presented here.

The measurements on acoustic phonons in bulk Germanium using excitation fluences of 2 to 35 mJ/cm^2 performed by DeCamp et al. [28] were explained by both electronic and thermal pressure contributions having approximately the same magnitudes. This result is in good agreement with the result presented in this thesis. However the low temporal resolution (about 100 ps) in the experiments of DeCamp did not allow the temporal evolution of the electronic pressure contribution to be resolved. The shape of the strain waves propagating into the bulk of Germanium in the experiments of both DeCamp and Chigarev could be described only if one takes into account the fast electron diffusion. It provides credence, that the measured strain waves are really influenced by the electronic pressure contribution, and not by some abnormalities in the thermal response of the material upon ultrafast excitation.

The experiments on a 400 nm Germanium film using an excitation fluence of 15 to 40 mJ/cm^2 performed by Cavalleri et al. [24] were explained only by the thermal pressure. At first view, this result contradicts the result in this thesis and that of

DeCamp et al. [28]. However, as was shown here, the presence of the electronic pressure in a thin film is seen as an increase of the ratio of the maximum-to-asymptotic angular shift. The maximum angular shift depends on the average value of the electronic pressure during the acoustic transit time T. For a given decay time of the electronic pressure this average value is smaller for a larger film thickness (larger T). Thus, for a thicker film one would expect a smaller ratio of the maximum-to-asymptotic angular shift. For a 400-nm-thick film and the decay time obtained in the experiments presented in this thesis, the contribution of the electronic pressure to the maximum shift becomes almost three times smaller than the contribution of the thermal pressure and consequently the main features of the experimental data can be explained just by the thermal pressure, as was done by Cavalleri et al.

Thus, the considerations made above revealed that the contradictions between some data in the literature are only apparent: In fact, the experimental data presented in literature are in good agreement with each other and with the measurements described in this thesis.

However, it should be noted that not all the features of the experimental data could be explained with the theoretical model presented here. In particular, the theoretical model could not elucidate the “slow” recompression and “broad” rocking curves for the “high” excitation regime.

As the investigation of the acoustic waves generated by ultrafast optical excitation is a relevant and important topic in ultrafast science, it is of great importance to understand the unexpected features in the measured data and the effects causing them. This represents an interesting topic for further investigations.

5. Summary and outlook

5.1. Summary

This thesis is dedicated to the study of the atomic motion in laser irradiated solids on a picosecond to subpicosecond time-scale using the time-resolved X-ray diffraction technique.

In the second chapter, the laser system, the laser-plasma based X-ray source and the experimental setup for optical pump / X-ray probe measurements were presented. To perform the experiments described in this thesis, the construction of a new experimental setup for optical pump / X-ray probe measurements was required. The old experimental setup, due to its geometrical restrictions, did not allow the observation of some of the Bragg-reflections which are necessary for effective measurements of the transient Debye-Waller factor. In this chapter special attention is paid to the characterization of the used laser-plasma based X-ray source, because its parameters determine which applications the setup can be used for. The work on optimization of the laser system and the experimental setup allowed the experiments described in this thesis to be performed with high accuracy.

The optical pump / X-ray probe experiments required in particular efficient recollection and focusing of the radiation of the laser-plasma based X-ray source because its radiation is emitted into the full solid angle. The X-ray focusing elements are therefore key elements in the experimental setup. Chapter 3 is devoted to the characterization and comparison of different types of X-ray optics. For each optic the amount and distribution of the X-rays in the focal plane was determined. It was found that all the optics tested can focus the X-ray radiation into a spot with the size (FWHM) of 100-200 μm. The measured fluxes of X-rays in the foci of all the optics were large enough to perform TRXD experiments. It was shown that for each type of experiment it is possible to choose a suitable kind of optic. In particular for the experiments where the measurements of the X-ray reflection profiles (rocking

curves) are of interest, the toroidal mirrors are best suited to fulfill the role of the focusing optic due to their narrow bandwidth (thus high angular resolution) and large convergence angle of the focused X-rays.

Multilayer mirrors and capillary optics focus typically the whole K_α radiation of the X-ray source including the $K_{\alpha 1}$ and $K_{\alpha 2}$ lines. Therefore, they are suitable if one is interested in the integral intensity of the diffracted signal from the sample under investigation but the profile of the rocking curve is not of interest. As multilayer mirrors and capillary optics have a relatively small convergence angle (due to their large magnification) they can be used in experiments where no large shifts of the rocking curves are expected.

It turned out, that the Ge (400) toroidal mirror for Ti-K_α radiation, due to its relatively large bandwidth provides a good compromise when both the integrated intensity and the angular distribution of the diffracted signal are of interest. This mirror was used for the experiments discussed in this thesis.

Chapter 4 presented the time-resolved X-ray diffraction experiments performed for this thesis.

The first section of this chapter discusses the measurements of initially unexpected strain-induced transient changes of the integrated reflectivity of the X-ray probe beam. These changes should be taken into consideration in any type of experiment in which an X-ray beam probes a spatially inhomogeneously strained sample, otherwise they can mask other physical effects such as the Debye-Waller factor. In particular, this effect should be carefully considered in any optical pump / X-ray probe experiment where the size of the pump beam differs from the size of the probe beam by less than at least one order of magnitude.

The elimination of the strain-induced transient changes of the integrated reflectivity described in the first section of chapter 4 represented an important prerequisite to perform the study of lattice heating in Germanium after femtosecond optical excitation by measuring the transient Debye-Waller effect. These measurements are described in the second section of chapter 4. It was found that the energy of the excited electrons is transferred to the lattice in just over one picosecond. The process

of electron-to-lattice energy transfer had been investigated previously by the observation of changes in the electronic system of the material. The experiments discussed here demonstrate that TRXD enables us to investigate this process also “from the lattice point of view”, thus completing our understanding of the energy relaxation in solids after optical excitation.

The third section describes the investigations of acoustic waves upon ultrafast optical excitation and discusses the two different pressure contributions driving them: the thermal and the electronic ones. The experiments performed here made it possible to estimate the relative strength of the electronic and thermal pressure contributions. The measured data were in line with the data presented in the work of Lindenberg et al. [23]. The values of the strength and the decay time of the electronic pressure obtained from the experiments provided clarification on some seeming contradictions in the measurements on acoustic phonons in Germanium discussed in the literature.

5.2. Outlook

This section discusses different possibilities for future research based on the results of the experiments performed for this thesis.

The experiments on Germanium described in this thesis demonstrated that TRXD can be used for the direct observation of lattice heating during electron-to-lattice energy transfer. As electron-lattice relaxation time is an important characteristic of each material and as a direct determination of this time from the "view of the lattice" is succeeded hitherto only for a very limited number of materials (only Germanium in this thesis, Silicon in [73] and Aluminum in [74] to the author's best knowledge) it is important to carry out studies for a wider range of materials.
The type of samples which can be currently used in the present experimental setup is strictly limited to monocrystalline thin films. Recently, new monocrystalline films (Gold and Iron) have become available. The measurements of lattice heating on these films can be proposed as the next step.
One way of avoiding the limitations of using monocrystalline samples is to utilize other diffraction schemes instead of the simple single-reflection Bragg-diffraction. An example is Debye-Scherrer (powder-) diffraction from polycrystalline samples. The first test of Debye-Scherrer diffraction with femtosecond X-ray pulses from the X-ray source used in the experimental setup was presented in this thesis. The result is promising enough to consider the possibility of performing time-resolved Debye-Scherrer diffraction which allows many diffraction orders to be observed simultaneously. As the Debye-Scherrer type of diffraction does not require monocrystalline samples the number of material systems which could be studied in TRXD experiments would increase drastically.

The Debye-Waller measurements of the lattice heating require a high level of accuracy because the expected changes of the diffracted signal constitute just a couple of percents. The expected increase of the X-ray signal by using the new X-ray

multilayer optics makes it possibly to perform such measurements with higher accuracy.

An alternative approach of developing this type of measurement is to use the shorter wavelength Cu-K_α radiation which allows the observation of high order reflections for which the same change of the lattice temperature causes larger changes of the diffracted signal.

The investigation of the electronic and thermal driving pressures appearing in the sample after the optical excitation provided clarification on some seeming contradictions in the explanation of the experimental results presented in the literature by different authors. Nevertheless, there are still some features which are not understood and which seem to be related to the strength of excitation. In particular, the measured electronic pressure contribution is significantly lower than that expected from theoretical estimations.
It is therefore desirable to extend this kind of experiment towards lower fluences in order to study how the electronic pressure contribution changes with the concentration of the excited carriers. This extension would also provide an opportunity to verify the validity of the suggestion made in this thesis that the low value of the electronic pressure contribution is connected with the fact that the excited carriers are not located at the edges of the conduction and valence bands (as is assumed in the theoretical model) but distributed over different energy levels within the Brillouin-zone.

Other non-explained results are the “slow” recompression and broadening of the measured rocking curve profiles of the excited sample compared with the theoretical model.
The broader profiles of the rocking curves measured for the “high” excitation fluences suggest that the strain profiles of the sample are more complicated than that predicted by the theoretical model. It might be due to spatially non-homogeneous distributions of the electronic and thermal pressures driving acoustic waves. The spatially non-homogeneous distributions can be caused, for example, by nonlinear

absorption at the “high” fluences. This suggestion can be verified by performing experiments on samples of smaller thickness, where non-homogeneity of the sample heating is smaller.

If the slow recompression is connected with changes of the relative acoustic impedance of the Germanium-Silicon interface, then for some intermediate excitation energy the acoustic impedance of Silicon should be equal to the acoustic impedance of Germanium and no acoustic waves will be reflected from the Germanium-Silicon interface. In this case only the first maximum in the oscillatory behavior of the angular shift should remain, which can be verified in the experiment.

Appendixes

A1. Properties of Germanium

Debye-temperature [82]	374 K
Atomic mass [82]	72,61
Absorption coefficient (for λ=800 nm) 1/α [93]	200 nm
Speed of sound [82]	5 555 m/s
Density [82]	5 323 kg/m^3
Bulk modulus [82]	70 GPa
Linear expansion coefficient [82]	5.9·10^{-6} 1/K
Specific heat [82]	1,98 J/(cm^3 K)
Melting temperature [82]:	1 210 K
Energy gap [94]	0.66 eV

Table A1.1. Properties of Germanium.

A2. Analytical solution of the wave equation

This appendix presents the model describing the acoustic response of a sample upon ultrafast optical excitation. First, the response of a semi-infinite sample is described. Secondly, this model is extended to the case of a thin film.

In the model one considers an ultrashort laser pulse that deposits its energy into an isotropic substrate and thereby generates a near instantaneous stress (or pressure). If the illuminated area A is much larger than the absorption depth ξ, the stress near the centre of the beam spot can be regarded as uniaxial. In this case the stress only exerts on the z-axis and the equations of elasticity have the following form [21]:

$$\sigma = \rho \mathrm{v}^2 \eta - \mathrm{P}(\mathrm{z},\mathrm{t}) \tag{1}$$

$$\rho \frac{\partial^2 \eta}{\partial \mathrm{t}^2} = \frac{\partial^2 \sigma}{\partial \mathrm{z}^2} \tag{2}$$

η denotes strain, ρ is material density and v is the sound speed, B is the bulk modulus, P(z,t) is the pressure induced by optical excitation.

Substituting η in (2) from (1) one obtains:

$$\frac{1}{\mathrm{v}^2}\frac{\partial^2 \eta(\mathrm{z},\mathrm{t})}{\partial \mathrm{t}^2} - \frac{\partial^2 \eta(\mathrm{z},\mathrm{t})}{\partial \mathrm{z}^2} = -\frac{1}{\rho \cdot \mathrm{v}^2}\frac{\partial^2}{\partial \mathrm{z}^2}\mathrm{P}(\mathrm{z},\mathrm{t}) \tag{3}$$

This non-homogeneous differential equation can be solved analytically after defining the initial and border conditions.
For the initial conditions determined by (4) and (5)

$$\eta(\mathrm{z},0) = \eta_0(\mathrm{z}) \tag{4}$$

$$\frac{\partial \eta(z,0)}{\partial t} = \eta_1(z) \tag{5}$$

and the border condition determined by (6)

$$\eta(0,t) = \eta_2(t) \tag{6}$$

the solution of the acoustic equation is given as [99, 100]:

$$\begin{aligned}\eta(z,t) &= \frac{1}{2}[H_0(z-vt) + H_0(z+vt)] + \\ &\frac{1}{2v}\int_{z-vt}^{z+vt} H_1(\xi)d\xi + \frac{v}{2}\iint_D H(\xi,\tau)d\xi d\tau + H_2(t-\frac{z}{v})\end{aligned} \tag{7}$$

where

$$H_0(z) = \begin{cases}\eta_0(z); z \geq 0 \\ -\eta_0(-z); z < 0\end{cases} \tag{8}$$

$$H_1(z) = \begin{cases}\eta_1(z); z \geq 0 \\ -\eta_1(-z); z < 0\end{cases} \tag{9}$$

$$H_2(z) = \begin{cases}0; t < \frac{z}{v} \\ -\eta_2(-t); t > \frac{z}{v}\end{cases} \tag{10}$$

$$H(z,t) = \begin{cases}-\frac{1}{\rho \cdot v^2}\frac{\partial^2}{\partial z^2}P(z,t); z \geq 0 \\ \frac{1}{\rho \cdot v^2}\frac{\partial^2}{\partial z^2}P(-z,t); z < 0\end{cases} \tag{11}$$

The area D corresponds to the triangle depicted in figure A3.1.

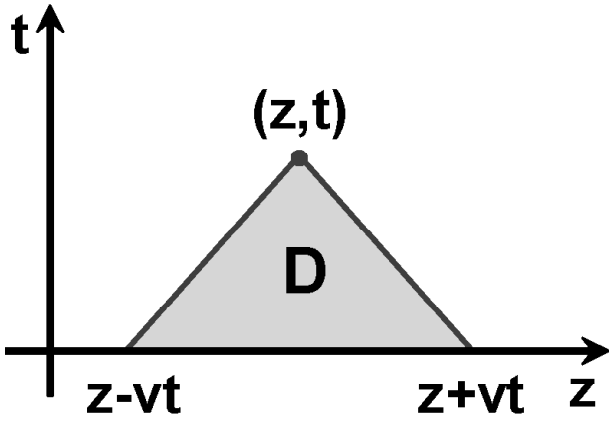

Figure A3.1. The area of integration for the double integral in solution of the acoustic equation.

Consider the particular case in which the energy deposited into a bulk sample is absorbed only due to the linear absorption (model described by Thomsen et al. in [21]). In this model the driving pressure is give by equation (12):

$$P(z) = 3B\beta(1-R)\frac{Q}{A\,d\,C}\exp\left(-\frac{z}{d}\right) \tag{12}$$

Where R is the reflectivity of the sample, C is the specific heat, β is the linear expansion coefficient, d is the absorption depth.

In this case the acoustic equation has the form:

$$\frac{1}{v^2}\frac{\partial^2\eta(z,t)}{\partial t^2} - \frac{\partial^2\eta(z,t)}{\partial z^2} = -3B\beta(1-R)\frac{Q}{\rho v^2 A\,d^3\,C}\exp\left(-\frac{z}{d}\right) \tag{13}$$

As initial conditions one takes zero deformation and zero derivation of it [21]:

$$\eta(z,0) = 0 \tag{4´}$$

$$\frac{\partial \eta(z,0)}{\partial t} = 0 \tag{5´}$$

As a border condition one assumes that the stress at the surface is zero $\sigma(z = 0) = 0$. Thus, according to equation (1) the border condition can be written as:

$$\eta(0,t) = \frac{P(0,t)}{\rho v^2} = 3B\beta(1-R)\frac{Q}{\rho v^2 A d C} \tag{6´}$$

Thus, for z>vt the solution of (3´) is given by:

$$\begin{aligned} \eta(z,t) &= \frac{v}{2}\iint_D -3B\beta(1-R)\frac{Q}{\rho v^2 A d^3 C}\exp(-\frac{\xi}{d})d\xi d\tau = \\ &= (1-R)\frac{QB}{AdC}\frac{1+\nu}{1-\nu}\left[\exp(-\frac{z}{d})\left(1-\frac{1}{2}\exp(-\frac{vt}{d})\right)-\frac{1}{2}\cdot\exp(-\frac{z-vt}{d})\right] \end{aligned} \tag{14}$$

For z<vt the solution of (3´) is given by:

$$\begin{aligned} \eta(z,t) &= \frac{v}{2}\iint_D -3B\beta(1-R)\frac{Q}{\rho v^2 A d^3 C}\exp(-\frac{\xi}{d})d\xi d\tau + \\ &+ 3B\beta(1-R)\frac{Q}{\rho v^2 A d C} = \\ &= (1-R)\frac{QB}{AdC}\frac{1+\nu}{1-\nu}\left[\exp(-\frac{z}{d})\left(1-\frac{1}{2}\exp(-\frac{vt}{d})\right)+\frac{1}{2}\cdot\exp(\frac{z-vt}{d})\right] \end{aligned} \tag{15}$$

Combining these two formulas one obtains the solution presented by Thomsen in [21]:

$$\eta(z,t) = \\ = (1-R)\frac{QB}{AdC}\frac{1+\nu}{1-\nu}\left[\exp(-\frac{z}{d})\left(1-\frac{1}{2}\exp(-\frac{vt}{d})\right)-\frac{\mathrm{sgn}(z-vt)}{2}\cdot\exp(-\frac{|z-vt|}{d})\right] \quad (16)$$

Figure A3.2 depicts the strain profile calculated in the frame of the "Thomsen model" for different times after optical excitation. As can be seen in figure A3.2 for the large time delays (t >> d/v) the lattice strain can be represented with two components. The former is a static thermal strain near the surface of the sample. The latter is a bipolar strain component propagating into the crystal with the speed of sound v.

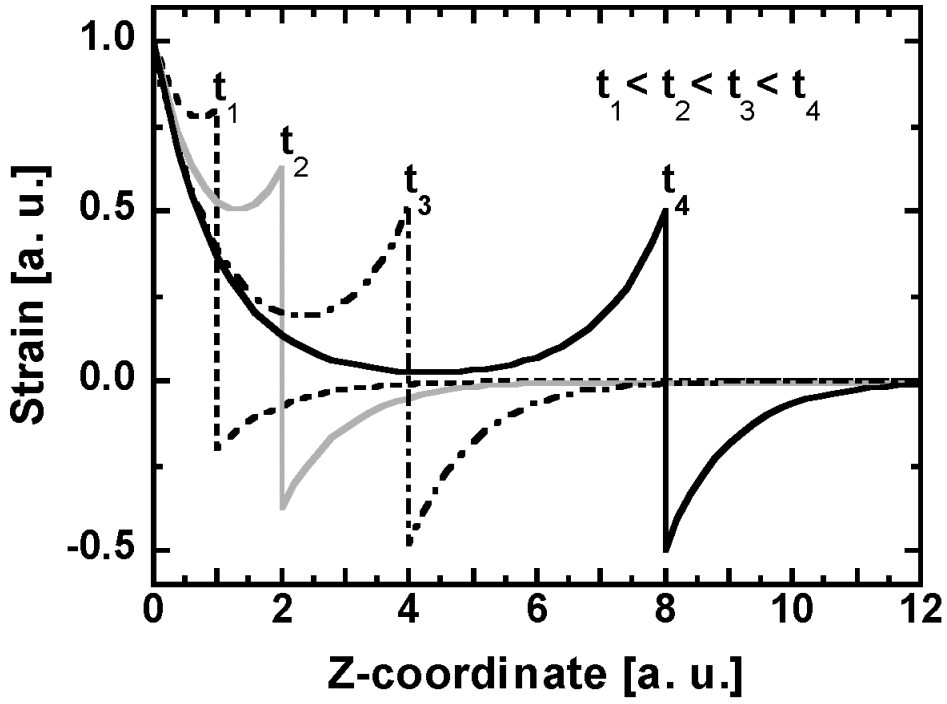

Figure A3.2. Calculated strain profile in the frame of the Thomsen model for different time delays after optical excitation.

To obtain a solution for the case of a thin film (experimental conditions for the measurements in this thesis) consider first the particular case of the solution for a bulk material. In this case one takes the same initial and border conditions as in the

Thomsen model, however the pressure is assumed to be independent of z (which is in most of the cases true for thin films) and dependent on time:

$$P(z,t) = f(t) \tag{17}$$

The solution of the acoustic equation in this case according to formula (7) has the form:

$$\eta(z,t) = \frac{1}{\rho \cdot v^2} f\left(t - \frac{z}{v}\right) \tag{18}$$

for $t > \frac{z}{v}$

and

$$\eta(z,t) = 0 \tag{19}$$

for $t < \frac{z}{v}$.

This solution represents a strain wave propagating from the border (z=0) into the bulk of material with the speed v. No deformation occurs for the coordinates z which are larger than v·t, according to formula (11). Figure A3.3 exemplifies this solution for $f(t) = \exp(-t/\tau)$, where τ is some constant.

If such a wave strikes a boundary with another material, then the wave is partly transmitted into the other material and partly reflected back. The amplitudes of the transmitted and reflected waves are determined by the acoustic impedances of the materials. The reflection coefficient is given as $R = \frac{Z_1 - Z_2}{Z_1 + Z_2}$, where Z_1 and Z_2 are the acoustic impedances ($Z_i = \rho_i \cdot v_i$) determined as a product of the material density and the speed of sound (the wave is assumed to come from the material with the

impedance Z_1 and enter material with the impedance Z_2). In the frame of linear acoustic the reflected wave adds itself linearly to the wave incident at the boundary.

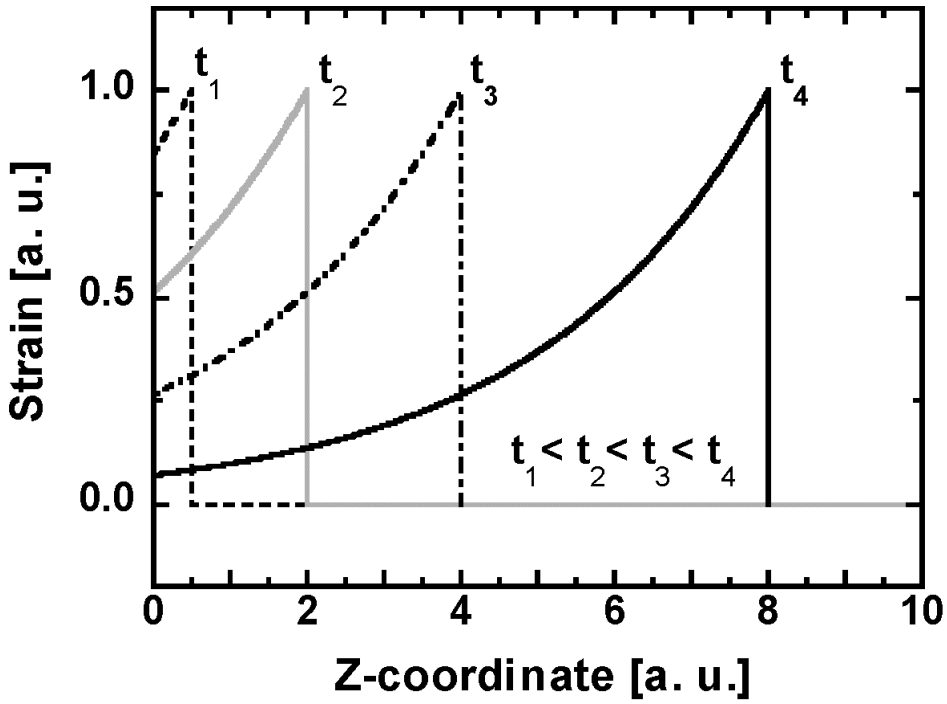

Figure A3.3. Calculated strain profile for the time-dependent driving pressure.

In the case of a thin film there are two acoustic waves which start to propagate from the two film boundaries. If these waves reach the other boundary reflection takes place as discussed above. The total strain profile is determined as a sum of the strain profiles caused by each of the waves. The examples of the strain profiles in this case are presented in figures 4.17 and 4.19 for the time-independent and exponentially decreasing function f(t), respectively. In these figures the amplitude of the wave starting to propagate from the Germanium-Silicon interface is determined by the condition that the pressures at the left and right sides of the interface are the same.
Appendix A.4 contains the code of the “Matlab”-program with the help of which these profiles were calculated.

A3. Simulation of the X-ray diffraction signal from strained crystals

This section presents the formalism which was used for the calculations of the Bragg-diffraction patterns.

The formalism for the scattering of X-rays from strained crystals using the dynamical diffraction theory was developed and introduced by Takagi and independently by Taupin in the 1960s [101,102]. Larson et. al. in [79] presented it in a notation with convenient units. Here, the extension of the model in [79] is presented, which provides the possibility to calculate diffraction for s- and p-polarized X-rays (only s- in [79]) and for the asymmetric diffraction, when the Bragg-planes are not parallel to the crystal surface.
In the notation of Larson et. al. [79] the scattering amplitude X from a strained crystal is given by the differential equation:

$$i\frac{dX}{dA} = X^2(1+ik) - 2X(y+ig) + (1+ik) \tag{1}$$

X is the normalized complex scattering amplitude given by:

$$X(A) = X_1 + iX_2 \tag{2}$$

A is the dimensionless depth within the crystal

$$A = \frac{r_e k_{pol} f'(\psi) e^{-M} \lambda t}{V_c \sqrt{|\gamma_0 \gamma_H|}} \tag{3}$$

k_{pol} is a polarization factor equal to unity and cos(ψ) for perpendicular and parallel polarization components, respectively; γ_0, γ_H represent the component of the incident and diffracted beam along the surface normal. $f(\psi) = f'(\psi) + if''(\psi)$ is the

X-ray structure factor, ψ is the scattering angle, e^{-M} is the Debye-Waller factor introduced in subsection 4.2.1. Coefficients g and k are given by

$$g = -\frac{f''(0)(1+b)}{2k_{pol}f'(\psi)e^{-M}\sqrt{|b|}} \tag{4a}$$

$$k = \frac{f''(\psi)}{f'(\psi)} \tag{4b}$$

where $b = \frac{\gamma_0}{\gamma_H}$ is the so-called asymmetry parameter, which is equal to unity for symmetrical reflections ($\gamma_0 = \gamma_H$).

y is the dimensionless angular deviation of the crystal from the Bragg angle

$$y = \frac{b\pi V_c \sin(2\theta_B)(\Delta\theta)}{k_{pol}\lambda^2 r_e f'(\psi)e^{-M}\sqrt{|b|}} - \frac{(1+b)f'(0)}{2k_{pol}f'(\psi)e^{-M}\sqrt{|b|}} \tag{5}$$

where $\Delta\theta = \theta - \theta_B$.

A depth-dependent lattice strain can be considered as a depth-dependent variation in θ_B. The change in the local Bragg-angle θ_B caused by strain distribution ε(A) is given by

$$\delta(A) = -\varepsilon(A)\tan(\theta_B) \tag{6}$$

and equation (5) can be generalized as follows:

$$y = \frac{b\pi V_c \sin(2\theta_B)[\Delta\theta + \varepsilon(A)\tan(\theta_B)]}{k_{pol}\lambda^2 r_e f'(\psi)e^{-M}\sqrt{|b|}} - \frac{(1+b)f'(0)}{2k_{pol}f'(\psi)e^{-M}\sqrt{|b|}} \quad (7)$$

Having determined all parameters in equation (1) one can solve it numerically for example using the Runga-Kutta method after separating equation (1) into two coupled equations

$$\frac{dX_1}{dA} = k(X_1^2 - X_2^2 + 1) + 2X_2(X_1 - y) - 2gX_1 \quad (8)$$

$$\frac{dX_2}{dA} = -(X_1^2 - X_2^2 + 1) + 2X_1(X_2 k + y) - 2gX_2 \quad (9)$$

The reflectivity of the crystal is determined by the square of the scattering amplitude absolute value as follows

$$R = |X(0)|^2 \quad (10)$$

where X(0) = X(A=0) is obtained by numerical integration of equation (8) and equation(9).

The point to be mentioned is that the formulas (5), (10) and (14) in [79] contain misprints. The correct way to write them is given in this appendix in equations (3), (4b) and (8), respectively. Appendix A4 presents the code of the “Matlab”-program which makes calculations based on this theory.

A4. “Matlab”-code of the program which calculates the diffraction signal from a strained crystal

```
%This is a starting point of the program
global T SO Strain A0 Theta Theta_assym Strain El_Contr

%Input parameters

%expected strain for the given excitation fluence
Strain = 0.00092;%for the Ge (111), 14 mJ/cm2

%electronic pressure contribution (the ratio of the electronic to the thermal pressures)
El_Contr = 0.8; %ratio 2.5 for the Ge (111) 14 mJ/cm2

%choose material
Material = 1;
%Material==1 - Ge
%Material==2 - GaAs
if Material == 1
%Structure factor for the scattering angle psi=0 (source XOP)
F0_Re = 255.157867 %real part
F0_Im = 20.190248 %imaginary part


%Structure factor for the Ge (111) reflection (source XOP)
Fpsi_Re = 154.2156 %real part
Fpsi_Im = 14.2767 %imaginary part
%Structure factor for the Ge (400) reflection (source XOP)
%Fpsi_Re = 162.762409327015 %real part
%Fpsi_Im = 20.1902484586520 %imaginary part
end;
```

```
if Material == 2
%Structure factor for psi=0 (source XOP)
F0_Re = 254.95874778 %real part
F0_Im = 20.263407 %imaginary part
%Structure factor for the GaAs (400) reflection (source XOP)
Fpsi_Re = 162.1582078997 %real part
Fpsi_Im = 20.263407 %imaginary part
end;



%Debye-Waller factor
DWF = 1;

%electron radius
R_electron = 2.817940325/1000000000000000 %m,
%wavelength
lambda = 2.74851/10000000000 %m

%Bragg angle
if Material == 1
Theta = 24.8823 %deg; the (111)-reflection
%Theta = 76.33502 %deg; the (400)-reflection

end;
%Theta_assym = -54.7356; %Asymmetry angle
Theta_assym = 0; %Asymmetry angle

b=sin((Theta+Theta_assym)*pi/180)/sin((Theta-
Theta_assym)*pi/180)%Asymmetry parameter

if Material == 2
Theta = 76.48800%degrees
```

```
end;
%polarization coefficient
KPol = 1; %s-polarization
%KPol = cos(2*Theta*pi/180); %p-polarization
if Material == 1
%unit cell size
a = 5.6578/10000000000 %m
end;
if Material == 2
%unit cell size
a = 4*1.413425/10000000000 %m
end;



%unit cell volume
Vc = a*a*a %m3

%Recalculation to a reduced spatial (i.e. depth) coordinate
Thickness_to_Acomplex =
KPol*R_electron*DWF*(Fpsi_Re)*lambda/(Vc*sqrt(abs(sin((Theta+Theta_as
sym)*pi/180)*sin((Theta-Theta_assym)*pi/180))))%corrected by Author

%Thickness
D=150/1000000000;
%D=400/1000000000;
%recalculation of the thickness to the reduced coordinate
Amax = Thickness_to_Acomplex*D;

if Material == 1
Velocity = 5555; %speed of sound
end;
```

```
if Material == 2
Velocity = 4730; %speed of sound
end;


%coefficients from the Larson paper [79]
g=-F0_Im*(1+b)/(2*KPol*Fpsi_Re*DWF*sqrt(abs(b)));

k=Fpsi_Im/Fpsi_Re;% corrected by Author, taken from Zachariazen. With this value one gets the same RC (rocking curve) as XOP gives!!!!!

%recalculation of the angle to the dimensionless units
Angle_to_y =
b*pi*Vc*sin(2*Theta*pi/180)/(KPol*lambda*lambda*R_electron*Fpsi_Re*DW
F*sqrt(abs(b)));

%calculation of the RC is done in the angular region [Theta_min, Theta_max]
Theta_max = 0.6; %deg
Theta_min = -0.8; %deg%limits of the angular range

%recalculation of the angular range to the dimensionless units
yMax=Angle_to_y*(Theta_max*pi/180+0)-
(1+b)*F0_Re/(2*sqrt(abs(b))*KPol*Fpsi_Re*DWF);
yMin=Angle_to_y*(Theta_min*pi/180+0)-
(1+b)*F0_Re/(2*sqrt(abs(b))*KPol*Fpsi_Re*DWF);
%Number of points in the range Theta_min to Theta_max
N=280
%angular step
yDelta=(yMax-yMin)/N
%uMax and uMin determine the temporal period during which the rocking curves are calculated
uMin=0
```

```
uMax=27*6*1*1
%initialization of the arrays to save the result of calculations
R0=zeros(1,N+1)';
R=zeros(N+1,uMax+1);
%begin of the main loop
for u=uMin:uMax
%the following two lines determine for which time delays the rocking curves are calculated
step = 6;
T=step*u*D/Velocity/(uMax-uMin)
tic
%begin of the loop which calculates the rocking curve for the given time delay
for s=1:N+1
%definition of the angle for which the diffracted signal should be calculated
y=yMin+(s-1)*yDelta;
%call a function to calculate one point of the rocking curve
[A,X]=ode45('DynXDiffrEquT',[Amax 0], [0; 0],[],y,k,g,Angle_to_y,T,Velocity,
D,Thickness_to_Acomplex);
%calculation of the X-ray reflectivity
R0(s)=(X(length(A),1).^2+X(length(A),2).^2);
end;
R(:,u+1)=R0;
ExecTime=toc

end;%end of the main loop
%choose how the result should be presented
ResultType = 3;
%1 RC(rocking curve)
%2 temporal dependence
%3 center of gravity temporal dependence
if ResultType == 1
%Here the RC will be plotted
```

```
Maximum = max(R(:,1))
Angles = Theta_min:(Theta_max-Theta_min)/(N):Theta_max;
plot(Angles, R(:,1),'LineWidth',2)
title(['maximum = 'num2str(max(R(:,1)))])
xlabel('Angular shift [deg.]');
ylabel('Intensity p-polarization [a. u.]');
if KPol == 1
  ylabel('Intensity s-polarization [a. u.]');
end;
end;

if ResultType == 2
%here the temporal dependence of the rocking curve profile in a false color representation will be depicted as a result
Times = step*uMin*(150/1000000000)/Velocity/(uMax-
uMin):(step*uMax*(150/1000000000)/Velocity/(uMax-uMin)-
step*uMin*(150/1000000000)/Velocity/(uMax-uMin))/(uMax-
uMin):step*uMax*(150/1000000000)/Velocity/(uMax-uMin);

imagesc(Times,[Theta_min Theta_max],R)

xlabel('time [ps.]');
ylabel('angular shift [deg.]');
  %here we prepare an array of the RC
  m_save_RC = R;
  %here we prepare an array of the RC plus angles as the first column
  Angles = Theta_min:(Theta_max-Theta_min)/(N):Theta_max;
  for s=1:N+1
  m_save_RC_ang(s,1) = Angles(s);
  end;
  for u=uMin:uMax
    for s=1:N+1
```

```
      m_save_RC_ang(s, u+2) = R(s,u+1);
    end;
  end;
  %here we save the data
  filename_RC = 'D:\Res1\my_RC.txt';
  save(filename_RC,'m_save_RC','-ASCII','-tabs')
  filename_RC_ang = 'D:\Res1\my_RC_ang.txt';
  save(filename_RC_ang,'m_save_RC_ang','-ASCII','-tabs')

end;

if ResultType == 3
%Here the center of gravity temporal dependence will be plotted
%initialization of the arrays which will be needed to show and save the data
CenterGrav = [0 0];
CenterGrav_corr = [0 0];
Int_Intensity = [0 0];

for u=uMin:uMax
  M0 = 0;
  M1 = 0;
  for s=1:N+1
    M1 = M1 + R(s,u+1)*(Theta_min +(Theta_max - Theta_min)*(s-1)/(N));
    M0 = M0 + R(s,u+1);
  end;
  CenterGrav(u+1) = M1/M0;
  Int_Intensity(u+1) = M0;
end;
for u=uMin:uMax
  CenterGrav_corr(u+1) = CenterGrav(1)-CenterGrav(u+1);
end;
CenterGrav_corr(u+1)
```

```
Times = step*uMin*27/(uMax-uMin):(step*uMax*27/(uMax-uMin)-
step*uMin*27/(uMax-uMin))/(uMax-uMin):step*uMax*27/(uMax-uMin);
%the center of gravity is plotted here
plot(Times, CenterGrav_corr,'LineWidth',2)

%title(['maximum = 'num2str(max(R(:,1)))])
xlabel('time [ps.]');
ylabel('angular shift [deg.]');
axis([0 170 -0.002 0.14])
v = axis
%here some horizontal lines are drawn at the plot
  line([D/Velocity*1000000000000 D/Velocity*1000000000000],[0 0.2],
'color',[.8 .8 .8])
  line([2*D/Velocity*1000000000000 2*D/Velocity*1000000000000],[0 0.2],
'color',[.8 .8 .8])
  line([3*D/Velocity*1000000000000 3*D/Velocity*1000000000000],[0 0.2],
'color',[.8 .8 .8])
  line([4*D/Velocity*1000000000000 4*D/Velocity*1000000000000],[0 0.2],
'color',[.8 .8 .8])

  %here we prepare arrays with the data we want to save
  My_size = size(Times);
  %here we prepare the array to save the centre of gravity
  m_save_array=zeros([My_size(2) 2]);
  m_save_array(:,1) = Times(:);
  m_save_array(:,2) = CenterGrav_corr(:)
  %here we prepare the array to save the intensity
  m_save_array_Int=zeros([My_size(2) 2]);
  m_save_array_Int(:,1) = Times(:);
  m_save_array_Int(:,2) = Int_Intensity(:);

  %here we prepare an array of RC
```

```
m_save_RC = R;
%here we prepare an array of RC plus angles as the first column
Angles = Theta_min:(Theta_max-Theta_min)/(N):Theta_max;
for s=1:N+1
m_save_RC_ang(s,1) = Angles(s);
end;
for u=uMin:uMax
  for s=1:N+1
    m_save_RC_ang(s, u+2) = R(s,u+1);
  end;
end;
%Here we prepare an array with some parameters of the calculation
Parameters(1,1) = D;
Parameters(2,1) = Theta_min;
Parameters(3,1) = Theta_max;

Parameters(4,1) = N;
Parameters(5,1) = uMin;
Parameters(6,1) = uMax;
Parameters(7,1) = step;
Parameters(8,1) = Fpsi_Re;
Parameters(9,1) = Fpsi_Im;
Parameters(10,1) = Theta;
Parameters(11,1) = Strain;
Parameters(12,1) = El_Contr;
Par = ' D; Theta_min; Theta_max; N; uMin; uMax; step; Fpsi_Re; Fpsi_Im;
Theta; Strain; El_Contr;';

%here we save the calculated data
filename = 'D:\Res\mycenter_grav.txt';
save(filename,'m_save_array','-ASCII','-tabs')
filename_RC = 'D:\Res\my_RC.txt';
```

```
 save(filename_RC,'m_save_RC','-ASCII','-tabs')
 filename_RC_ang = 'D:\Res\my_RC_ang.txt';
 save(filename_RC_ang,'m_save_RC_ang','-ASCII','-tabs')
 filename_Int = 'D:\Res\my_Int.txt';
 save(filename_Int,'m_save_array_Int','-ASCII','-tabs')
 filename_Parameters = 'D:\Res\my_Parameters.txt';
 save(filename_Parameters,'Parameters','-ASCII','-tabs')
 filename_Par = 'D:\Res\my_Par.txt';
 save(filename_Par,'Par','-tabs')

end;

save Session8



%the following function calculates the diffracted signal for the given strain profile
function dX = DynXDiffrEquT(A,X,flag,y,k,g,Angle_to_y,Time,Velocity,
Thickness,Thickness_to_Acomplex)
global T A0 Amax Theta Theta_assym Strain El_Contr

%here we call a function that calculates the profile of the strained film
S1 = strainFilm(A/Thickness_to_Acomplex,Time, Thickness,Velocity,
1830000000000, 1,
Strain*El_Contr)+strainFilm(A/Thickness_to_Acomplex,Time,
Thickness,Velocity, 0, 1, Strain);
%here the profile is recalculated to the dimensionless units
S=Angle_to_y*S1*tan(Theta*pi/180)*cos(abs(Theta_assym*pi/180))*cos(abs(
Theta_assym*pi/180))*(1-tan(abs(Theta_assym*pi/180))/tan(Theta*pi/180));
%here the differential equation to be calculated is determined
dX=[k*(X(1)^2-X(2)^2+1)+2*X(2).*(X(1)-y-S)-2*g*X(1);-(X(1)^2-
X(2)^2+1)+2*X(1).*(X(2)*k+y+S)-2*g*X(2)];
```

```
%this function calculates the strain profile for the bulk sample
function S = strainT(A, Time, Velocity, Gamma, No, SO)
global A0

%choose the model describing strain
StrainType = 3;
%StrainType == 1 is the Thomsen model
%StrainType == 2 is the Auger decay model
%StrainType == 3 is the model with an exponential stress dependence


if StrainType ==1
 %Thomsen model
 if A > (Time*Velocity)
   S=SO*(exp(-A/A0)-1/2*exp((Time*Velocity-A)/A0) - 1/2*exp(-
(Time*Velocity+A)/A0));
 else
   S=SO*(exp(-A/A0)+1/2*exp(-(Time*Velocity-A)/A0) - 1/2*exp(-
(Time*Velocity+A)/A0));
 end
end

if StrainType ==2
 %Auger decay model

 %the following lines determine strain as a function of the coordinate 'A'(which is
equal to Z) and time 'Time'
 if A > (Time*Velocity)
   S=0;
```

```
  else
    S=SO/(sqrt(1+ 2*Gamma*No*No*(Time-(A/Velocity))));
  end
end

if StrainType ==3
  %exponential dependence model
  tau = 40/1000000000000;%for the Ge (111) 14 mJ/cm2 el_Contr = 0.8 and for the Ge (111) 35 mJ/cm2 El_Contr = 0.62;%ratio 2.3
  %the following lines determine strain as a function of the coordinate 'A' (which is equal to Z) and time 'Time'
  if A > (Time*Velocity)
    S=0;
  else
    if Gamma == 0
      S=SO;% instantaneous thermal pressure
      %S=SO*(1-exp(-(Time-(A/Velocity))/(1.1/1000000000000)));%exponential increase of the thermal pressure
    else
      S=SO*exp(-(Time-(A/Velocity))/tau);
  end
  end
end



%this function calculates the strain profile of the film sample
function SFilm = strainFilm(A, Time, Thickness, Velocity, Gamma, No, SO)
global A0
%here we define local variables equal to the input parameters
T = Time;
D = Thickness;
```

```
V = Velocity;

R = 0.15; % Reflection coefficient at the Germanium-Silicon interface. It is
calculated from the acoustic impedances.
Rel_Ampl = 0.6; % Relative amplitude of the wave propagating from the
Germanium-Silicon interface

%The following if-else construction describes the wave origins from the
Germanium-vacuum interface
%the terms with R*R*R*R are neglected. (0.15^4=5*10^-4)
if (T*V) <= D
  SFilm1 = strainT(A, Time, Velocity, Gamma, No, SO);
elseif (T*V) <= 2*D
  SFilm1 = strainT(A, T, V, Gamma, No, SO) - R*strainT(2*D-A, T, V,
Gamma, No, SO);
elseif (T*V) <= 3*D
  SFilm1 = strainT(A, T, V, Gamma, No, SO) - R*strainT(2*D-A, T, V,
Gamma, No, SO) + R*strainT(2*D+A, T, V, Gamma, No, SO);
elseif (T*V) <= 4*D
  SFilm1 = strainT(A, T, V, Gamma, No, SO) - R*strainT(2*D-A, T, V,
Gamma, No, SO) + R*strainT(2*D+A, T, V, Gamma, No, SO) -
R*R*strainT(4*D-A, T, V, Gamma, No, SO);
elseif (T*V) <= 5*D
  SFilm1 = strainT(A, T, V, Gamma, No, SO) - R*strainT(2*D-A, T, V,
Gamma, No, SO) + R*strainT(2*D+A, T, V, Gamma, No, SO) -
R*R*strainT(4*D-A, T, V, Gamma, No, SO)+ R*R*strainT(4*D+A, T, V,
Gamma, No, SO);
elseif (T*V) <= 6*D
  SFilm1 = strainT(A, T, V, Gamma, No, SO) - R*strainT(2*D-A, T, V,
Gamma, No, SO) + R*strainT(2*D+A, T, V, Gamma, No, SO) -
R*R*strainT(4*D-A, T, V, Gamma, No, SO)+ R*R*strainT(4*D+A, T, V,
Gamma, No, SO)- R*R*R*strainT(6*D-A, T, V, Gamma, No, SO);
```

```
else
  SFilm1 = strainT(A, T, V, Gamma, No, SO) - R*strainT(2*D-A, T, V,
Gamma, No, SO) + R*strainT(2*D+A, T, V, Gamma, No, SO) -
R*R*strainT(4*D-A, T, V, Gamma, No, SO)+ R*R*strainT(4*D+A, T, V,
Gamma, No, SO)- R*R*R*strainT(6*D-A, T, V, Gamma, No, SO)+
R*R*R*strainT(6*D+A, T, V, Gamma, No, SO);
end

%The following if-else construction describes the wave origins from the
Germanium-Silicon interface
%the last term with R*R*R and the terms with R*R*R*R are neglected.
(0.15^4=5*10^-4)
if (T*V) <= D
  SFilm2 = strainT(D-A, T, V, Gamma, No, SO);
elseif (T*V) <= 2*D
  SFilm2 = strainT(D-A, T, V, Gamma, No, SO) - strainT(D+A, T, V, Gamma,
No, SO);
elseif (T*V) <= 3*D
  SFilm2 = strainT(D-A, T, V, Gamma, No, SO) - strainT(D+A, T, V, Gamma,
No, SO) + R*strainT(3*D-A, T, V, Gamma, No, SO);
elseif (T*V) <= 4*D
  SFilm2 = strainT(D-A, T, V, Gamma, No, SO) - strainT(D+A, T, V, Gamma,
No, SO) + R*strainT(3*D-A, T, V, Gamma, No, SO) - R*strainT(3*D+A, T, V,
Gamma, No, SO);
elseif (T*V) <= 5*D
  SFilm2 = strainT(D-A, T, V, Gamma, No, SO) - strainT(D+A, T, V, Gamma,
No, SO) + R*strainT(3*D-A, T, V, Gamma, No, SO) - R*strainT(3*D+A, T, V,
Gamma, No, SO)+ R*R*strainT(5*D-A, T, V, Gamma, No, SO);
elseif (T*V) <= 6*D
  SFilm2 = strainT(D-A, T, V, Gamma, No, SO) - strainT(D+A, T, V, Gamma,
No, SO) + R*strainT(3*D-A, T, V, Gamma, No, SO) - R*strainT(3*D+A, T, V,
```

```
Gamma, No, SO)+ R*R*strainT(5*D-A, T, V, Gamma, No, SO)-
R*R*strainT(5*D+A, T, V, Gamma, No, SO);
else
  SFilm2 = strainT(D-A, T, V, Gamma, No, SO) - strainT(D+A, T, V, Gamma,
No, SO) + R*strainT(3*D-A, T, V, Gamma, No, SO) - R*strainT(3*D+A, T, V,
Gamma, No, SO)+ R*R*strainT(5*D-A, T, V, Gamma, No, SO)-
R*R*strainT(5*D+A, T, V, Gamma, No, SO)+ R*R*R*strainT(7*D-A, T, V,
Gamma, No, SO);
end

%the result is a sum of the two waves
SFilm = SFilm1 + Rel_Ampl*SFilm2;



%this part of the program package is to test how the calculated strain profile for the
thin film looks
global T A0
Thickness = 150/1000000000; %Film thickness
Velocity = 5555; %Sound speed

T=10*Thickness/Velocity %Time

Gamma=4*1.83*1000000000000; %Auger coefficient
%Gamma=0*1000000000000; %Auger coefficient
No=1; %Electron concentration
SO = 1;% strain amplitude due to the thermal pressure contribution
%S0_electr = SO*0.8;% strain amplitude due to the electronic pressure contribution
%depth changes from A_Min till A_Max
A_min = 0;
A_max = Thickness;
ResultType = 1;
```

```
s = [0];
z = [0];

%ResultType == 1 in this case the program will show a strain profile for the given time T
%ResultType == 2 in this case the program will show a temporal dependence of the average strain
if ResultType ==1
  N = 451;  %number of points in the depth interval [0, Thickness]
  for n=1:N
        A=A_min + (A_max - A_min)*(n-1)/(N-1);
        s(n)=strainFilm(A, T, Thickness, Velocity, Gamma, No,
S0_electr);%+strainFilm(A, T, Thickness, Velocity, 0, No, SO);
  end
  s
  avgStr = 0;
  for n=1:N
    avgStr = avgStr +s(n);
  end
  avgStr/N

  %the following lines provide a plot of the calculated strain s(n)
  %z=1:1:N;
  %z = zeros(N);
  for n=1:N
    z(n) = Thickness*1000000000*(n-1)/(N-1);
  end
  plot(z,s,'LineWidth',2)

  axis([1 z(N) -0.1 1.1])
  line([3 150-2],[0 0], 'color',[.8 .8 .8])
  %plot(s)
```

```
  %title(['Time=' num2str(Velocity*T/Thickness)])
  title(['Time= ' num2str(T*1000000000000) ' ps;' '   ( Time / 27ps ) = '
num2str(T*1000000000000/27) ';    (Tau / 27 ps) = 2.55/27 '])

  xlabel('Thickness [nm.]')
  ylabel('Strain [a. u.]')
  %here we prepare an array of the data to be saved
  m_save_array=zeros([N 2]);
  m_save_array(:,1) = z(:);
  m_save_array(:,2) = s(:);
  %here we save the data
  filename = ['D:\el_pr_tau2_55\' num2str(T*1000000000000) '.txt'];
  save(filename,'m_save_array','-ASCII','-tabs')
end

if ResultType ==2
  %here we calculate the temporal dependence of the average strain

  %we calculate the time from TMin to TMax
  TMin = 0;
  TMax = 150/1000000000000; %ps
  TMax = 162/1000000000000; %ps

  TimeIntervals = 12; %TimeIntervals+1 is the amount of intervals for the
calculations within [TMin Tmax]

  N = 150;  %number of points in the depth interval [0, Thickness]
  Times = [0 2];
  for tt=0:TimeIntervals
    Times(tt+1) = 0;
    avStrain(tt+1) = 0;
  end;
```

```
 %starting point of the main loop where the strain profiles are calculated
 for tt=0:TimeIntervals
   TCurrent = TMin + (TMax-TMin)*tt/TimeIntervals;
   for n=1:N
         A=A_min + (A_max - A_min)*(n-1)/(N-1);
         s(n)=strainFilm(A, TCurrent, Thickness, Velocity, Gamma, No,
S0_electr)+strainFilm(A, TCurrent, Thickness, Velocity, 0, No, SO);
   end
   Times(tt+1) = TCurrent*1000000000000;
   avgStr = 0;
   for n=1:N
     avgStr = avgStr +s(n);
   end
   avStrain(tt+1) = avgStr/N
 end
 Times
 %here we plot the temporal dependence of the average strain
 plot(Times,avStrain,'LineWidth',2)
 axis([TMin*1000000000000 TMax*1000000000000  -0.25 2.7])
 %here we draw a horizontal line
 line([TMin*1000000000000 TMax*1000000000000],[0 0], 'color',[.8 .8 .8])
 %here we draw vertical lines
 line([Thickness/Velocity*1000000000000
Thickness/Velocity*1000000000000],[0 2.5], 'color',[.8 .8 .8])
 line([2*Thickness/Velocity*1000000000000
2*Thickness/Velocity*1000000000000],[0 2.5], 'color',[.8 .8 .8])
 line([3*Thickness/Velocity*1000000000000
3*Thickness/Velocity*1000000000000],[0 2.5], 'color',[.8 .8 .8])
 line([4*Thickness/Velocity*1000000000000
4*Thickness/Velocity*1000000000000],[0 2.5], 'color',[.8 .8 .8])
```

```
  %title(['(Tau / 27 ps) = 1.5
'])%,'FontName','Helvetica','FontSize',18,'Color','black')
  title(['(electronic pressure)/(thermal pressure) = 0.8; tau = 40
ps'])%,'FontName','Helvetica','FontSize',18,'Color','black')
  xlabel('Time
[ps.]')%,'FontName','Helvetica','FontWeight','Bold','FontSize',20)
  ylabel('Strain [a.
u.]')%,'FontName','Helvetica','FontWeight','Bold','FontSize',20)

  %here we prepare an array of the data to be saved
  m_save_array=zeros([TimeIntervals+1 2]);
  m_save_array(:,1) = Times(:);
  m_save_array(:,2) = avStrain(:);
  %here we save the data from the array m_save_array
  filename = 'd:\aaa1_165.txt';
  save(filename,'m_save_array','-ASCII','-tabs')
end



%this file is to test how the calculated strain profile for the bulk sample looks like
global T A0
S0=1%strain amplitude
Velocity = 5555; %speed of sound
%Velocity = 4730; speed of sound
T=3*27/1000000000000 %Time
Thickness = 150/1000000000; %Film thickness

A0=800/1000000000 %absorbtion depth

Gamma=1.83*1000000000000; %Auger coefficient
%Gamma=0*1000000000000; %Auger coefficient
```

```
%this part of the program package is to test how the calculated strain profile for the bulk sample looks like
No=1; %concentration of electrons
SO = 1;% strain amplitude
%here we define a depth interval [0, Thickness]
A_min = 0;
A_max = Thickness;
N = 1000;  %number of points in the depth interval [0, Thickness]
s = zeros(N);

%the following loop calculates the strain profile
for n=1:N
        A=A_min + (A_max - A_min)*n/N;
   s(n)=strainT(A, T, Velocity, Gamma, No, 1.4)+strainT(A, T, Velocity, 0, 0, 1);
end

%Here the calculated strain will be plotted
z = zeros(N);
for n=1:N
  z(n) = Thickness*1000000000*n/N;
end
plot(z,s,'LineWidth',2)
axis([1 z(N) -0.4 2.4])

line([14 Thickness*1000000000-14],[0 0], 'color',[.8 .8 .8])
xlabel('Thickness [nm.]','FontSize',12,'FontWeight','bold','FontName','Arial')
ylabel('Strain [a. u.]','FontSize',12,'FontWeight','bold','FontName','Arial')
```

Bibliography

[1] W. C. Röntgen,
Über eine neue Art von Strahlen,
Sitz. ber. an die med.-phys. Gesellschaft Würzburg, 1895.

[2] M. von Laue,
Eine quantitative Prüfrung der Theorie für die Interferenz-Erschei-nungen bei Röntgenstrahlen,
Sitz. ber. der Kgl. Bayer. Akad. Wiss., **363**, 73 (1912).

[3] M. von Laue,
Interferenzerscheinungen bei Röntgenstrahlen,
Ann. Phys. Lpz., **41**, 989 (1913).

[4] W. H. Bragg, W. L. Bragg,
The reflection of X-rays by crystals,
Proc. Roy Soc. London, **A88**, 249 (1913).

[5] S. Backus, G. Durfee, M. M. Murnane and H. C. Kateyn,
High power ultrafast lasers,
Rev. Sci. Instr., **69**, 1207, (1998).

[6] E. B. Treacy,
Optical pulse compression,
IEEE J. Quan. Electron., **5**, 454, (1969).

[7] C. Rischel, A. Rousse, I. Uschmann, P. A. Albouy, J. P. Geindre, P. Audebert, J. C. Gauthier, E. Förster, J. L. Martin and A. Antonetti,
Femtosecond time-resolved X-ray diffraction from laserheated organic films,

Nature, **390,** 490 (1997).

[8] A. Cavalleri, M. Rini, H. H. W. Chong, S. Fourmaux, T. E. Glover, P. A. Heimann, J. C. Kieffer, and R. W. Schoenlein,
Band-selective measurements of electron dynamics in VO_2 using femtosecond near-edge X-ray absorption,
Phys. Rev. Lett., **95**, 67405 (2005).

[9] A. M. Lindenberg, J. Larsson, K. Sokolowski-Tinten, K. J. Gaffney, C. Blome, O. Synnergren, J. Sheppard, C. Caleman, A. G. MacPhee, D. Weinstein, D.P. Lowney, T. Allison, T. Matthews, R. W. Falcone, A.L. Cavalieri, D. M. Fritz, S. H. Lee, P. H. Bucksbaum, D. A. Reis, J. Rudati, P. H. Fuoss, C. C. Kao, D.P. Siddons, R. Pahl, J. Als-Nielsen, S. Düsterer, R. Ischebeck, H. Schlarb, H. Schulte-Schrepping, Th. Tschentscher, J. Schneider, D. von der Linde, O. Hignette, F. Sette, H. N. Chapman, R.W. Lee, T. N. Hansen, S. Techert, J. S. Wark, M. Bergh, G. Huldt, D. van der Spoel, N. Timneanu, J. Hajdu, R. A. Akre, E. Bong, P. Krejcik, J. Arthur, S. Brennan, K. Luening, J. B. Hastings,
Atomic scale visualization of inertial dynamics,
Science, **308**, 392 (2005).

[10] K. J. Gaffney, A. M. Lindenberg, J. Larsson, K. Sokolowski-Tinten, C. Blome, O. Synnergren, J. Sheppard, C. Caleman, A. G. MacPhee, D. Weinstein, D. P. Lowney, T. Allison, T. Matthews, R. W. Falcone, A. L. Cavalieri, D. M. Fritz, S. H. Lee, P. H. Bucksbaum, D. A. Reis, J. Rudati, P. H. Fuoss, C. C. Kao, D. P. Siddons, R. Pahl, K. Moffat, J. Als-Nielsen, S. Düsterer, R. Ischebeck, H. Schlarb, H. Schulte-Schrepping, Th. Tschentscher, J. Schneider, D. von der Linde, O. Hignette, F. Sette, H. N. Chapman, R. W. Lee, T. N. Hansen, S. Techert, J. S. Wark, M. Bergh, G. Huldt, D. van der Spoel, N. Timneanu, J. Hajdu, R. A. Akre, E. Bong, P. Krejcik, J. Arthur, S. Brennan, K. Luening, J.B. Hastings,

Observation of structural anisotropy and the onset of liquidlike motion during the nonthermal melting of InSb,
Phys. Rev. Lett., **95**, 125701 (2005).

[11] M. Bargheer, N. Zhavoronkon, M. Woerner, and T. Elsaesser,
Recent progress in ultrafast X-ray diffraction,
Chemphyschem, **7**, 783 (2006).

[12] T. Pfeifer, C. Spielmann and G. Gerber,
Femtosecond X-ray science,
Rep. Prog. Phys., **96**, 443 (2006).

[13] C. W. Siders, A. Cavalleri, K. Sokolowski-Tinten, C. Toth, T. Guo, M. Kammler, M. Horn-von Hoegen, K. R. Wilson, D. von der Linde and C. P. J. Barty,
Detection of nonthermal melting by ultrafast X-ray diffraction,
Science, **286**, 1340, (1999).

[14] A. Rousse, C. Rischel, S. Fourmaux, I. Uschmann, S. Sebban, G. Grillon, Ph. Balcou, E. Förster, J. P. Geindre, P. Audebert, J. C. Gauthier, and D. Hulin,
Non-thermal melting in semiconductors measured at femtosecond resolution,
Nature, **410**, 65(2001).

[15] K. Sokolowski-Tinten, C. Blome, C. Dietrich, A. Tarasevitch,M. Horn-von Hoegen, D. von der Linde, A. Cavalleri, J. Squier and M. Kammler,
Femtosecond X-ray measurement of ultrafast melting and large acoustic transients,
Phys. Rev. Lett., **87,** 225701 (2001).

[16] T. Feurer, A. Morak, I. Uschmann, Ch. Ziener, H. Schwoerer, Ch. Reich, P. Gibbon, E. Förster, R. Sauerbrey, K. Ortner and C. R. Becker, *Femtosecond silicon K_α pulses from laser-produced plasmas,* Phys. Rev. E, **65**, 016412 (2001).

[17] P. B. Hillyard, K. J. Gaffney, A. M. Lindenberg, S. Engemann, R. A. Akre, J. Arthur, C. Blome, P. H. Bucksbaum, A. L. Cavalieri, A. Deb, R.W. Falcone, D. M. Fritz, P. H. Fuoss, J. Hajdu, P. Krejcik, J. Larsson, S. H. Lee, D. A. Meyer, A. J. Nelson, R. Pahl, D. A. Reis, J. Rudati, D. P. Siddons, K. Sokolowski-Tinten, D. von der Linde, and J. B. Hastings, *Carrier-density-dependent lattice stability in InSb***,** Phys. Rev. Lett., **98**, 125501 (2007).

[18] K. Sokolowski-Tinten, C. Blome, J. Blums, A. Cavalleri, C. Dietrich, A. Tarasevitch, I. Uschmann, E. Förster, M. Kammler, M. Horn-von Hoegen and D. von der Linde, *Femtosecond X-ray measurement of coherent lattice vibrations near the Lindemann stability limit,* Nature, **422**, 287 (2003).

[19] D. M. Fritz, D. A. Reis, B. Adams, R. A. Akre, J. Arthur, C. Blome, P. H. Bucksbaum, A. L. Cavalieri, S. Engemann, S. Fahy, R. W. Falcone, P. H. Fuoss, K. J. Gaffney, M. J. George, J. Hajdu, M. P. Hertlein, P. B. Hillyard, M. Horn-von Hoegen, M. Kammler, J. Kaspar, R. Kienberger, P. Krejcik, S. H. Lee, A. M. Lindenberg, B. McFarland, D. Meyer, T. Montagne, É. D. Murray, A. J. Nelson, M. Nicoul, R. Pahl, J. Rudati, H. Schlarb, D. P. Siddons, K. Sokolowski-Tinten, Th. Tschentscher, D. von der Linde, J. B. Hastings, *Ultrafast bond softening in Bismuth: Mapping a solid's interatomic potential with X-rays,* Science, **315**, 633 (2007).

[20] C. Thomsen, J. Strait, Z. Vardeny, H. J. Mark. J. Tauc, and J. Hauser, *Coherent phonon generation and detection by picosecond light pulses,* Phys. Rev. Lett., **53**, 989 (1984).

[21] C. Thomsen, H. T. Grahn, H. J. Maris, and J. Tauc, *Surface generation and detection of phonons by picosecond light pulses,* Phys. Rev. B, **34**, 4129, (1986).

[22] C. Rose-Petruck, R. Jimenez, T. Guo, A. Cavalleri, C. W. Siders, F. Raksi, J. A. Squier, B. C. Walker, K. R. Wilson, and C. P. J. Barty, *Picosecond-milliangström lattice dynamics measured by ultrafast X-ray diffraction,* Nature, **398**, 310, (1999).

[23] A. M. Lindenberg, I. Kang, S. L. Johnson, T. Missalla, P. A. Heimann, Z. Chang, J. Larsson, P. H. Bucksbaum, H. C. Kapteyn, H. A. Padmore, R. W. Lee, J. S. Wark and R. W. Falcone, *Time-resolved X-ray diffraction from coherent phonons during a laser-induced phase transition,* Phys. Rev. Lett., **84**, 111, (2000).

[24] A. Cavalleri, C.W. Siders, F. L. H. Brown, D. M. Leitner, C. Tóth, J. A. Squier, C. P. J. Barty, K. R. Wilson, K. Sokolowski-Tinten, M. Horn-von Hoegen, D. von der Linde, and M. Kammler, *Anharmonic lattice dynamics in germanium measured with ultrafast X-ray diffraction,* Phys. Rev. Lett., **85**, 586 (2000).

[25] A. Cavalleri, C. W. Siders, C. Rose-Petruck, R. Jimenez, Cs. Tóth, J. A. Squier, C. P. J. Barty, K. R. Wilson, K. Sokolowski-Tinten, M. Horn-von

Hoegen, and D. von der Linde,
Ultrafast x-ray measurement of laser heating in semiconductors: Parameters determining the melting threshold,
Phys. Rev. B, **63**, 193306 (2001).

[26] D. A. Reis, M. F. DeCamp, P. H. Bucksbaum, R. Clarke, E. Dufresne, M. Hertlein, R. Merlin, R. Falcone, H. Kapteyn, M. M. Murnane, J. Larsson, Th. Missalla, and J. S. Wark,
Probing impulsive strain propagation with X-Ray pulses,
Phys. Rev. Lett., **86**, 3072 (2001).

[27] J. Larsson, A. Allen, P. H. Bucksbaum, R. W. Falcone, A. Lindenberg, G. Naylor, T. Missalla, D. A. Reis, K. Scheidt, A. Sjögren, P. Sondhauss, M. Wulff, J. S.Wark,
Picosecond X-ray diffraction studies of laser-excited acoustic phonons in InSb,
Appl. Phys. A, **75**, 467 (2002).

[28] M. F. DeCamp, D. A. Reis, A. Cavalieri, P. H. Bucksbaum, R. Clarke, R. Merlin, E.M. Dufresne, D. A. Arms, A.M. Lindenberg, A.G. MacPhee, Z. Chang, B. Lings, J. S.Wark, and S. Fahy,
Transient strain driven by a dense electron-hole plasma,
Phys. Rev. Lett., **91**, 165502 (2003).

[29] M. Bargheer, N. Zhavoronkov, Y. Gritsai, J. C. Woo, D. S. Kim, M. Woerner, T. Elsaesser,
Coherent atomic motions in a nanostructure studied by femtosecond X-ray diffraction,
Science, **306**, 1771 (2004).

[30] S. H. Lee, A. L. Cavalieri, D. M. Fritz, M. C. Swan, R. S. Hegde, M.

Reason, R. S. Goldman, and D. A. Reis,
Generation and propagation of a picosecond acoustic pulse at a buried interface: Ttime-resolved X-ray diffraction measurements,
Phys. Rev. Lett., **95**, 246104 (2005).

[31] Y. Hayashi, Y. Tanaka, T. Kirimura, N. Tsukuda, E. Kuramoto, and T. Ishikawa,
Acoustic pulse echoes probed with time-resolved X-ray triple-crystal diffractometry,
Phys. Rev. Lett., **96**, 115505 (2006).

[32] C. V. Korff Schmising, M. Bargheer, M. Kiel, N. Zhavoronkov, M. Woerner, T. Elsaesser, I. Vrejoiu, D. Hesse, and M. Alexe,
Strain propagation in nanolayered perovskites probed by ultrafast x-ray diffraction,
Phys. Rev. B, **73**, 212202 (2006).

[33] A. Morak, T. Kämpfer, I. Uschmann, A. Lübcke, e. Förster, and R. Sauerbrey,
Acoustic phonons in InSb probed by time-resolved x-ray diffraction,
Phys. Stat. Sol. B, **243**, 2728 (2006).

[34] M. Born and E. Wolf,
Principles of optics,
Cambridge University Press, 1988.

[35] D. Kühlke, U. Herpers and D. von der Linde,
Soft X-ray emission from subpicosecond laser-produced plasmas,
App. Phys. Lett., **50**, 1785 (1987).

[36] G. Jenke,

Erzeugung von XUV- und Röntgenstralung mit Femtosecunden-Laserimpulsen,
Dissertation, 1999.

[37] A. Rousse, P. Audebert, J. P. Geindre, F. Fall, and J. C. Gauthier,
Effcient K_α X-ray source from femtosecond laser-produced plasmas,
Phys. Rev. E, **50**, 2200 (1994).

[38] Z. Jiang, J. C. Kieer, J. P. Matte, M. Chaker, O. Peyrusse, D. Gilles, G. Korn, A. Maksimchuk, S. Coe, and G. Mourou,
X-ray spectroscopy of hot solid density plasmas produced by subpicosecond high contrast laser pulses at 10^{18}–10^{19} W/cm^2,
Phys. Plasmas, **2**, 1702 (1995).

[39] F. Brunel,
Not-So Resonant, Resonant Absorption,
Phys. Rev. Lett., **59**, 52 (1987).

[40] S. C. Wilks and W. L. Kruer,
Absorption of ultrashort, ultra-intense laser light by solids and overdense plasmas.
IEEE J. Quan. Electron., **33**, 1954 (1997).

[41] S. Bastiani, A. Rousse, J. P. Geindre, P. Audebert, C. Quoix, G. Hamoniaux, A. Antonettia, and J. C. Gauthier,
Experimental study of the interaction of subpicosecond laser pulses with solid targets of varying initial scale lengths,
Phys. Rev. E, **56**, 7179 (1997).

[42] P. Gibbon, E. Förster,
Short-pulse laser-plasma interactions,

Plasma Phys. Control. Fusion **38**, 769 (1996).

[43] T. Feuer, A. Morak, I. Uschmann, Ch. Ziener, H. Schwoerer, E. Förster, R. Sauerbrey,
An incoherent sub-picosecond X-ray source for time-resolved X-ray-diffracion experiments
Appl. Phys. B, **72**, 15 (2001).

[44] C. Reich, P. Gibbon, I. Uschmann and E. Förster,
Yield optimization and time structure of femtosecond laser plasma K_α sources,
Phys. Rev. Lett., **84**, 4846, (2000).

[45] T. Guo, Ch. Spielmann, B. C. Walker, C. P. J. Barthy,
Generation of hard X-rays by ultrafast terawatt lasers,
Rev. Sci. Instr., **72**, 41, (2001).

[46] A. Rousse, C. Rischel, and J. C. Gauthier,
Colloquium: Femtosecond X-ray crystallography,
Rev. mod. Phys., **73**, 17, (2001).

[47] C. Blome, K. Sokolowski-Tinten, C. Dietrich, A. Tarasevitch and D. von der Linde,
Set-up for ultrafast time-resolved X-ray diffraction using a femtosecond laser-plasma keV X-ray-source,
Journal de Physique, IV(11), (2001).

[48] S. Kähle,
Erzeugung kurzer Röntgenimpulse.
Diplomarbeit, 2002.

[49] D. Strickland and G. Mourou,
Compression of amplified chirped optical pulses,
Opt. Commun., **56,** 219 (1985).

[50] S. Backus, C. G. Durfee III, M. M. Murnane, and H. C. Kapteyn,
High power ultrafast lasers,
Rev. Sci. Instr., **69**, 1207 (1998).

[51] S. I. Salem, P. L. Lee,
Expermental width of K and L X-ray lines,
Atomic and nuclear data tables, **18**, 233-241 (1976).

[52] J. A. Koch, O. L. Landen, T. W. Barbee, P. Celliers, L. B. Da Silva, S. G. Glendinning, B. A. Hammel, D. H. Kalantar, C. Brown, J. Seely, G. R. Bennett, and W. Hsing,
High-energy X-ray microscopy techniques for laser-fusion plasma research at the national ignition facility,
Appl. Opt., **37**, 1784 (1998).

[53] P. Elleaume, C. Fortgang, C. Penel, and E. Tarazona,
Measuring beam sizes and ultra-small electron emittances using an X-ray pinhole camera,
J. Synchrotron Rad., **2**, 209 (1995).

[54] T. Missalla, I. Uschmann, E. Förster, G. Jenke, and D. von der Linde,
Monocromatic focusing of subpicosecond X-ray pulses in the KeV range,
Rev. Sci. Instr., **70**, 1288 (1999).

[55] I. Uschmann,
Beiträge zur Röntgendiagnose laserinduzierter Plasmen mit gebogenen Kristallen,

Dissertation (1991).

[56] M. Montel,
Aberrations du premier ordre des systèmes catoptriques asymétriques Application au microscope X à réflexion totale,
Optica Acta, **1**, 117 (1954).

[57] P. Kirkpatrick and A. Baez,
Formation of optical images by X-rays,
J. Opt. Soc. Am., **38**, 766 (1948).

[58] S. K. Sundaram, and E. Mazur,
Inducing and probing non-thermal transitions in semiconductors using femtosecond laser pulses,
Nature materials, **1**, 217 (2002).

[59] W. N. Knox, D. S. Chemla, G. Livescu, J. E. Cunningham, and. J. E. Henry,
Femtosecond carrier thermalization in dense Fermi seas,
Phys. Rev. Lett., **61**, 1290, (1988).

[60] J. Shah,
Photoexcited hot carriers: from cw to 6 fs in 20 years,
Solid-State Electron., **32**, 1051 (1989).

[61] H. E. Elsayed-Ali, T. B. Norris, M. A. Pessot, and G. A. Mourou,
Time-resolved observation of electron-phonon relaxation in Cooper,
Phys. Rev. Lett., **58**, 1212 (1987).

[62] R. H. M. Groeneveld, R. Sprik, and A. Lagendijk,
Effect of a nonthermal electron distribution on the electron-phonon energy

relaxation process in noble metals,
Phys.Rev. B, **45**, 5079 (1992).

[63] R. H. M. Groeneveld, R. Sprik, and A. Lagendijk,
Femtosecond spectroscopy of electron-electron and electron-phonon energy relaxation in Ag and Au,
Phys. Rev. B, **51**, 11433 (1995).

[64] X. Y. Wang, d. M. Riffe, Y. S. Lee, and M. C. Downer,
Time-resolved electron-temperature measurements in a highly excited gold target using femtosecond thermionic emission,
Phys. Rev. B., **50**, 8016 (1994).

[65] J. Hohlfeld, S.-S. Wellershoff, J. Güdde, U. Conrad, V. Jähnke, E. Matthias,
Electron and lattice dynamics following optical excitation of metals,
Chem. Phys., **251**, 237 (2000).

[66] C. K. Sun, F. Vallee, L. Acioli, E. P. Ippen, and J. G. Fujimoto,
Femtosecond investigation of electron thermalization in gold,
Phys. Rev. B., **48**, 12365 (1993).

[67] G. L. Eesley,
Generation of nonequilibrium electron and lattice temperatures in cooper by picosecond laser pulses,
Phys. Rev. B., **33**, 2144 (1986).

[68] J. G. Fujimoto, J. M. Liu, E. P. Ippen, N. Bloembergen,
Femtosecond laser interaction with metallic tungsten and nonequilibrium electron and lattice temperatures,
Phys. Rev. Lett., **53**, 1837 (1984).

[69] L. Huang, J. P. Callan, E. N. Glezer, and E. Mazur,
GaAs under intense ultrafast excitation: Responce of the dielectric function,
Phys. Rev. Lett., **80**, 185 (1998).

[70] J. R. Goldman and J. A. Prybyla,
Ultrafast dynamics of laser-excited electron distributions in Silicon,
Phys. Rev. Lett., **72**, 1364 (1994).

[71] N. Del Fatti, R. Bouffanais, F. Vallee, and C. Flytzanis,
Nonequilibrium electron interactions in metal films,
Phys. Rev. Lett., **81**, 922 (1998).

[72] D. von der Linde, J. Kuhl, H. Klingenberg,
Raman scattering from nonequilibrium LO phonons with picosecond resolution,
Phys. Rev. Lett., 44, 1505 (1980).

[73] M. Harb, R. Ernstorfer, T. Dartigalongue, C.T. Hebeisen, R. E. Jordan, and R. J. Dwayne Miller,
Carrier relaxation and lattice heating dynamics in silicon revealed by femtosecond electron diffraction,
J. Phys. Chem. B, **110**, 25308 (2006).

[74] H. Park, X. Wang, S. Nie, R. Clinite, and J. Cao,
Mechanism of coherent acoustic phonon generation under nonequilibrium conditions,
Phys. Rev. B, **72**, 100301 (2005).

[75] P. Debye,

Interferenz von Röntgenstrahlen und Wärmebewegung,
Ann. d. Phys., **43**, 49 (1914).

[76] I. Waller,
Zur Frage der Einwirkung der Wärmebewegung auf die Interferenz von Röntgenstrahlen,
Z Phys., **17**, 398 (1923).

[77] C. Kittel,
Introduction to solid state physics,
6th ed. Wiley, New York, 1986.

[78] G. Busch and H. Schade,
Lectures on solid state physics,
Pergamon, New York, 1976.

[79] B. C. Larson, J. Z. Tischler and D. M. Mills,
Nanosecond resolution time-resolved X-ray study of silicon during pulsed-laser irradiation,
J. Mater. Res., **1**, 144 (1986).

[80] M. Horn-von Hoegen, F. K. LeGoues, M. C. Reuter and R. M. Tromp,
Defect self-annihilation in surfactant-mediated epitaxial growth,
Phys. Rev. Lett., **67**, 1130 (1991).

[81] M. Horn-von Hoegen,
Surfactants: Perfect heteroepitaxy of Ge on Si (111),
Appl. Phys. A, **59**, 503 (1994).

[82] H. H. Landolt and Börnstein,
Zahlenwerte und Funktionen aus Naturwissenschaft und Technik,

Springer, Madelung, 1961.

[83] J. F. Young and H. M. van Driel,
Ambipolar diffusion of high-density electrons and holes in Ge, Si, and GaAs: Many-body effects,
Phys. Rev. B, **26**, 2147 (1982).

[84] M. Bargheer, N. Zhavoronkov, J. C. Woo, D. S. Kim, M. Woerner, and T. Elsaesser,
Excitation mechanisms of coherent phonons unravelled by femtosecond X-ray diffraction,
Phys. Stat. Sol. (b), **243**, 2389 (2006).

[85] J. J. Baumberg, D. A. Williams, and K. Köhler,
Ultrafast acoustic phonon ballistics in semiconductor heterostructures,
Phys. Rev. Lett. **78**, 3358 (1997).

[86] O. Matsuda, T. Tachizaki, T. Fukui, J. J. Baumberg, and O. B. Wright,
Acoustic phonon generation and detection in GaAs/$Al_{0.3}Ga_{0.7}$As quantum wells with picosecond laser pulses,
Phys. Rev. B, **71**, 115330 (2005).

[87] O. B. Wright, B. Perrin, O. Matsuda, and V. E. Gusev,
Ultrafast carrier diffusion in gallium arsenide probed with picosecond acoustic pulses,
Phys. Rev. B, **64**, 081202 (2001).

[88] H. Chin, R.W. Schoenlein, T. E. Glover, P. Balling, W. P. Leemans, and C. V. Shank,
Ultrafast structural dynamics in InSb probed by time-resolved X-ray diffraction,

Phys. Rev. Lett., **83**, 336 (1999).

[89] N. V. Chigarev, D. Yu. Paraschuk, X. Y. Pan, and V. E. Gusev,
Coherent phonon emission in the supersonic expansion of photoexcited electron-hole plasma in Ge,
Phys. Rev. B, **61**, 15837 (2000).

[90] G. Tas and H. J. Maris,
Electron diffusion in metals studied by picosecond ultrasonics,
Phys. Rev. B, **49**, 015046 (1994).

[91] O. B. Wright,
Ultrafast nonequilibrium stress generation in gold and silver,
Phys. Rev. B, **49**, 9985 (1994).

[92] O. B. Wright and V. E. Gusev,
Acoustic generation in crystalline silicon with femtosecond optical pulses,
Appl. Phys. Lett., **66**, 1190 (1995).

[93] E. D. Palik,
Handbook of optical constants of solids,
Academic Press Handbook Series, 1985.

[94] Physical properties of semiconductors [online],
http://www.ioffe.rssi.ru/SVA/NSM/Semicond/index.html

[95] B. Krenzer, A. Janzen, P. Zhou, D. von der Linde and M. Horn-von Hoegen,
Thermal boundary conductance in heterostructures studied by ultrafast electron diffraction,
New J. Phys., **8**, 190 (2006).

[96] P. Hyldgaard,
Resonant thermal transport in semiconductor barrier structures,
Phys. Rev. B, **69**, 193305 (2004).

[97] E. J. Yoffa,
Dynamics of dense laser-induced plasmas,
Phys. Rev. B, **21**, 2415 (1980).

[98] W. H. Zachariasen,
Theory of X-ray diffraction in crystals,
New York: Dover Classics of Science and Mathematics, 1994.

[99] N. Bronstein and K. A. Semendjajew,
Teubner-Taschenbuch der Mathematik,
B. G. Teubner Stuttgart, Leipzig, 1996.

[100] G. A. Korn and T. M. Korn,
Mathematical handbook for scientist and engineers,
Mc-Graw-Hill Inc., New York, 1961.

[101] S. Takagi,
A dynamical theory of diffraction for a distorted crystal,
J. Phys. Soc. Japan, **26**, 1239 (1969).

[102] D. Taupin,
Théorie dynamique de la diffraction des rayons X par les cristaux déformés.
Bull. Soc. Fr. Mineral. Crystallogr., **87**, 469 (1964).

Acknowledgments

This thesis results from my research at the „Institut für Experimentelle Physik“ at the University of Duisburg-Essen. This thesis could not have been written without the help, assistance and support of many people.

First of all, I would like to thank my supervisor Prof. Dr. Dietrich von der Linde for the opportunity to carry out my PhD studies in the “Intensive Laserstrahlung und ultraschnelle Phänomene” group and his support in accomplishing of this thesis.

Special thank goes to my advisor Dr. Klaus Sokolowski-Tinten for his wonderful spirit at work, for numerous discussions, advice, and explanations. I don’t know how you did it but you made me always coming to work enjoyable. It has been an honor and a pleasure for me to work with you.

To Matthieu Nicoul. I will never forget the countless nights we spent in the lab (especially the one when we got home at 6 o’clock in the morning after the 20 hours experiment on acoustic phonons in Germanium). Thank you for being a great friend and colleague.

To Konstantin Lobov. I can’t remember any situation in which I could not turn to you for your advice. You always helped me. I don’t know what my life would be like now if you were not here. Thank you for everything you have done for me.

To Dr. Alexander Tarasevitch for his support, in particular for the laser-system. I would never have been able to do all the measurements for my PhD project without the laser-system you developed here.

To Dr. Juris Blums and Dr. Christian Blome for their invaluable help during the initial stages of my PhD studies.

I thank Prof. Dr. Dietrich von der Linde, Prof. Dr. Michael Horn-von Hoegen and Prof. Dr. Lothar Schäfer for being members of the examination board for my thesis.

I also would like to thank Prof. Dr. Michael Horn-von Hoegen for growing Germanium on Silicon and Bismuth on Silicon samples.

I would like to thank Michael Bieske for his technical assistance, which helped to make many things faster and easier.

Many thanks to Kay Eibl for her help in solving all the administrative problems. And of course special thanks for the reading my thesis and trying to improve my “Russian” English.

I am also grateful to Stephan Kähle, Wei Lu and Manuel Ligges for their advice on how to write the things more clearly.

Many greetings to all members of the group – I enjoyed your company very much.

I would like to profoundly thank my parents for always being there for me. Even when there were thousands of kilometers between us during my PhD studies here you were always with me in my mind and in my heart. I always felt your presence and support. I can never repay you for what you have been giving me all my life.

There are so many people who helped me in many ways during my PhD studies that listing them all on a piece of paper would be quite difficult. I will therefore need to thank them in person.